

Measurement of $\sigma(\text{p}\bar{\text{p}} \rightarrow \text{Z}) \cdot \text{Br}(\text{Z} \rightarrow \tau^+\tau^-)$ and
search for Higgs bosons decaying to $\tau^+\tau^-$
at $\sqrt{s} = 1.96 \text{ TeV}$

Measurement of $\sigma(\text{p}\bar{\text{p}} \rightarrow \text{Z}) \cdot \text{Br}(\text{Z} \rightarrow \tau^+\tau^-)$ and
search for Higgs bosons decaying to $\tau^+\tau^-$
at $\sqrt{s} = 1.96 \text{ TeV}$

EEN WETENSCHAPPELIJKE PROEVE OP HET GEBIED VAN DE
NATUURWETENSCHAPPEN, WISKUNDE EN INFORMATICA

PROEFSCHRIFT

TER VERKRIJGING VAN DE GRAAD VAN DOCTOR
AAN DE RADBOUD UNIVERSITEIT NIJMEGEN
OP GEZAG VAN DE RECTOR MAGNIFICUS PROF. MR. S.C.J.J. KORTMANN,
VOLGENS BESLUIT VAN HET COLLEGE VAN DECANEN
IN HET OPENBAAR TE VERDEDIGEN OP WOENSDAG 25 JUNI 2008
OM 13.30 UUR PRECIES

DOOR

Cristina Florina Galea

GEBOREN OP 26 MAART 1975
TE BUCUREȘTI, ROEMENIË

Promotor: Prof. dr. S.J. de Jong

Manuscriptcommissie:	Prof. dr. M.W.J.M. Demarteau	Universiteit van Amsterdam
	Dr. S.D. Protopopescu	Brookhaven National Laboratory
	Dr. S. Nelson	Stanford Linear Accelerator Center
	Prof. dr. R.H.P. Kleiss	
	Prof. dr. T.H.M. Rasing	

ISBN 978-90-9023129-7

Cover: Mount Everest © Mark Hannaford, Across the Divide Expeditions.

The work described in this thesis is part of the research programme of the “Nationaal Instituut voor Kernfysica en Hoge-Energie Fysica” (NIKHEF) in Amsterdam, the Netherlands. The author was financially supported by the “Stichting voor Fundamenteel Onderzoek der Materie” (FOM).

Contents

1	Introduction	1
2	The Standard Model of particle physics	5
2.1	Electroweak theory	7
2.2	Quantum Chromodynamics	9
2.3	Z boson production and decay at the Tevatron	10
2.4	Higgs boson production and decay at the Tevatron	12
2.5	Problems with the Standard Model	15
2.6	The Minimal Supersymmetric Standard Model	16
3	Experimental setup	19
3.1	The Tevatron	19
3.2	The DØ detector	21
3.2.1	Coordinate system	21
3.2.2	Central tracking system	22
3.2.3	Calorimeter system	26
3.2.4	Muon system	29
3.2.5	Luminosity monitor	32
3.2.6	Trigger and data acquisition systems	33
4	Object Identification	37
4.1	Tracks	37
4.2	Vertices	38
4.3	Muons	38
4.4	Electrons and photons	39
4.5	Jets	40
4.6	Missing E_T	41
5	Tau leptons	43
5.1	Tau lepton identification	43
5.2	Tau candidate energy correction	46
5.2.1	General method	49
5.2.2	Energy correction for type 1 tau candidates	50
5.2.3	Energy correction for type 2 tau candidates	55
5.2.4	Energy correction for type 3 tau candidates	61
5.2.5	Energy corrections for data	65
5.2.6	Missing E_T correction	68

6	Z boson cross section measurement	69
6.1	Data set	69
6.2	Trigger efficiency	71
6.3	Event simulation	77
6.3.1	Z boson p_T reweighting	79
6.3.2	Instantaneous luminosity profile reweighting	79
6.3.3	Beam shape correction	80
6.3.4	Muon efficiency corrections	80
6.3.5	Tracking efficiency correction for tau candidates	80
6.3.6	Vertex efficiency correction	81
6.4	Event selection	81
6.5	Background	82
6.5.1	QCD background	82
6.5.2	W + jets background	83
6.6	Charge mis-identification correction	85
6.7	Estimating the $Z \rightarrow \tau^+\tau^-$ signal	86
6.8	Systematic uncertainties	101
6.9	Results	103
7	Limits on neutral Higgs boson production	105
7.1	Limits on SM Higgs boson production	105
7.2	Limits in the $\tan\beta - m_A$ plane for the MSSM	114
8	Conclusions and outlook	117
	Bibliography	119
	Summary	127
	Samenvatting	129
	About the author	133
	Acknowledgements	135

1

Introduction

The state of the matter regarding the way we understand the universe today is that matter doesn't really matter. A long winding road took us in several hundred years from believing that we were conveniently located in the center of the universe, to realizing that while that may well be true, there are uncountable such centers everywhere else (and for sure the Sun does not revolve around the Earth). The road took us then further to being proud that we are made of stars, only a few decades ago. What a truly astounding discovery that was, to finally find out how all chemical elements were produced, namely in the center of a star somewhere! From there, however, we soon went on to understanding just how small we really are in this incredibly large world which, on top of it all, is still expanding at a rate given by the Hubble constant.

So here we are now, with new reasons to feel special again: according to the latest astronomical measurements, the matter that we are made of, the chairs on which we sit, this whole planet in fact, the Sun, the Milky Way at the border of which we are happily rotating around a black hole at 32,000 km/h, all other galaxies and the gas between them - all this constitutes only 5 % of the universe. Out of which more than 80 % is just free hydrogen and helium, the stars accounting for another 10 % and the neutrinos for 9.94 %. As Rocky Kolb once put it, who would go through the trouble to learn chemistry fully knowing that they would study only 0.03 % of the universe? The rest of 95 % of the world, the astronomers tell us, is made of 25 % dark matter (named like that because it does not emit radiation, and its presence can only be deduced from the gravitational influence on galaxies and clusters of galaxies) and 70 % dark energy, the existence of which is indirectly inferred from the time evolution of the Hubble constant (which, as it turns out, is not constant after all), besides other arguments such as the age of the universe and structure formation. We know today equally much about the dark matter and the dark energy. Namely very close to nothing [1,2].

Had I known this five and a half years ago when I started my doctoral studies, would I still have chosen to go into particle physics? The answer is: probably yes. This is a very exciting time in science, when astrophysics grows closer and closer to the type of research we do these days at accelerator laboratories. What if, one day, we will discover in high energy collisions a particle which will be a good candidate for dark matter? The physics of the two infinities, the infinitely large and the infinitely small, need each other. Besides, even though the facts listed above are based on very serious and most up to date research of hundreds of very smart people, one never knows if in a while from now - which may not even be longer than a few years, or a few decades - someone reading this will not be laughing unstoppably at how ignorant people used to be in 2007. After all, very respectable and knowledgeable men of the 16th century knew for sure that they were living in the center of the universe and the Sun, the Moon and the stars - all about 5000 of them - were rotating around them.

Back to Earth now, we still seem to have some work to do in understanding how our 5 % of the universe functions. But even here (or especially here) we came a long way in a very short time. It is impossible to make a comprehensive summary of all the progress made in only one century. A new field called particle physics attracted the curiosity and efforts of hundreds of brilliant minds at the beginning of the 20th century. Since then, thirty three Nobel Prizes were awarded for important contributions to this field. The next paragraphs will only mention a few of the milestones reached on the way to where we find ourselves today.

The current understanding of matter and what holds it together started sometime in the middle of the 19th century (Newton and his 17th century theory of gravity notwithstanding), when Maxwell published a set of equations which describe the inter-relationship between the electric and magnetic fields, the electric charge and electric current. Thirty six years later, in 1897, Thomson discovered the electron, the first of the particles which are still considered elementary. This happened a year after Becquerel had found evidence for spontaneous radioactivity in uranium decay, which set the start of the nuclear era. Within the first five years of the 20th century, Planck had already established the bases for quantum physics and Einstein the ones for the theory of relativity. In 1911, Rutherford found evidence for the atomic nucleus, and after another eight years he was also the one to discover the proton as a constituent of the nucleus. In 1913 Bohr invented the quantum theory of atomic spectra. A year later Chadwick made the first observation that the β spectrum is continuous, not discrete as expected from Bohr's theory. This was the first evidence for the existence of neutral almost non-interacting particles which we call today neutrinos and which were proposed in 1930 by Pauli as an explanation for the continuous β decay spectrum. Compton produced the experimental evidence that the photon is an elementary particle in 1923, the same year de Broglie proposed the corpuscular-wave dualism that still holds for electrons and all other elementary particles.

The concept of elementary particle spin was introduced in 1925 by Kronig, Uhlenbeck and Goudsmit. The fact that elementary particles, which are point-like, can possess non-zero spin is one of the most remarkable discoveries in quantum physics. Theoretical and experimental studies have shown that the spin possessed by these particles cannot be explained by postulating that they are made up of even smaller particles rotating about a common center of mass. The spin they carry is thus an intrinsic physical property, similar to the particle's electric charge and mass. Pauli developed the concept of spin, although he had vehemently rejected it in the beginning. He formalized the theory of spin in 1927, using matrices as a representation of the spin operators, and introduced a two-component spinor wave function. Fermions have half-integer spin and bosons integer spin, with interesting consequences for their statistical behaviour, namely that the number of bosons which may occupy a given quantum state is not restricted, while for the fermions this number is limited to maximum 1 (the Pauli exclusion principle). Pauli's theory was developed further by Dirac in his new relativistic wave equation for electrons which was published a year later, in 1928.

Between 1925 and 1927, Heisenberg and Schrödinger proposed two different formulations of quantum mechanics and Dirac set the foundations of Quantum Electrodynamics (QED). In 1931 Dirac proposed the existence of anti-particles, namely the positron and anti-proton. The former was discovered the following year by Anderson. The first evidence for the existence of the neutron was obtained in 1932 by Chadwick, and Heisenberg suggested the same year that nuclei are composed of protons and neutrons. Thus, in the early 1930's, the building blocks necessary for explaining the periodic table of elements were known, and even new chemical elements not yet discovered could be predicted based on this new understanding of matter.

The next generation of particles was discovered more or less by accident. As physicists were trying to understand what could possibly hold the positive particles together in a nucleus, in spite of their Coulomb rejection, they were searching for a particle called “meson”, which was proposed by Yukawa as a mediator of a new force called the strong force. Two particles were found at the same time in cosmic rays (the existence of which had just been discovered in 1912 by Hess): one was called pion, and the other one muon. The second generation of particles had been found, although it was only recognized as such many years later.

Heisenberg introduced the concept of isospin to explain several symmetries found in nature: the mass near degeneracy of proton and neutron, as well as the one of the charged and neutral pions, and finally the strength of the interactions between any pair of nucleons being the same, independently on the nucleon type. The isospin symmetry was given by the invariance of the Hamiltonian of the strong interactions under the action of the Lie group $SU(2)$. The neutron and the proton were assigned to the doublet (spin- $\frac{1}{2}$ or fundamental representation) of the group, while the pions were assigned to the triplet (the spin-1 or adjoint representation). The discovery of additional particles like the kaons induced the broadening of the concept of isospin symmetry into a larger symmetry called the Eight-fold Way by Gell-Mann, which was soon recognized to be an adjoint representation of the $SU(3)$ group. This led almost immediately to Gell-Mann's proposal of the existence of quarks, which would belong to the fundamental representation of the flavour $SU(3)$ symmetry. From this representation and its conjugate (the quarks and antiquarks) the higher representations corresponding to the mesons and baryons could be assembled.

In 1968, Glashow [3], Salam [4] and Weinberg [5] unified electromagnetism with the theory of the weak interactions into one concept called the electroweak theory. At that time, three quarks were known (the up, down and strange quarks), and four leptons (the electron, the muon and their respective neutrinos). A new quark, called charm, was added with the simultaneous discovery at Brookhaven and SLAC of the J/ψ meson in 1974. A third charged lepton called the tau was discovered by Perl at SLAC in 1975 [6]. It was found to have a mass about 3500 times higher than the mass of the electron, and about 17 times the mass of the muon. This large mass allows it to decay not only into lighter leptons, but also into hadrons and a neutrino.

After the discovery of the tau lepton the searches for more particles of the third family started. In 1977 the bottom quark was discovered. A sixth quark which was expected to exist was only found almost twenty years later: the top quark was discovered in 1995 at Fermilab. In 2000 the DONUT experiment also at Fermilab made a direct observation of the last lepton to be observed, namely the tau neutrino.

This thesis is the story of a journey on the look for the last particle predicted by theory more than four decades ago, but never found, in spite of historical efforts by thousands of physicists. It is called the Higgs boson. The next chapter gives a short presentation of the theories that we now believe are sufficient to describe our universe in terms of particles and the interactions between them. These theories were put together under the name of Standard Model of particle physics. The necessity and the place of the Higgs boson within these theories are briefly presented in this chapter. While remarkably successful so far, the Standard Model comes with its own problems and limitations. Possible solutions for these problems may be found in its most researched extension known as the Minimal Supersymmetric Standard Model (MSSM), which is also described briefly in the second chapter. Chapter 3 describes the experimental apparatus necessary for such an undertaking, while Chapter 4 introduces the reader to the way physical objects such as tracks, vertices, muons, electrons, photons and jets are reconstructed using this apparatus and the software tools necessary for analyzing the signals received from it. Chapter 5 concentrates on the identification of and energy correction for tau leptons, which are the main focus of this thesis.

The most important background in a search for the Higgs boson in the $\tau^+\tau^-$ channel, such as pursued in this analysis, is coming from the process $p\bar{p} \rightarrow Z \rightarrow \tau^+\tau^-$, which needs to be thoroughly understood. A measurement of the cross section times branching ratio $\sigma \cdot \text{Br}$ for this process is presented in Chapter 6. As no evidence for additional resonant sources of $\tau^+\tau^-$ events was observed, limits on the production of neutral Higgs boson are deduced in Chapter 7. These limits were interpreted as well within a few MSSM benchmark scenarios. Finally, Chapter 8 concludes and describes in addition a few methods to improve the precision of this measurement and the sensitivity of this search in the future.

2

The Standard Model of particle physics

The Standard Model (SM) of particle physics is a collection of theories which developed first independently, starting sometime in the middle of the twentieth century. Its purpose is to mathematically describe the world we live in at the most fundamental level, based on the old principle of Democritus that everything is decomposable into smaller and smaller pieces, until the truly indivisible parts are reached. Those indivisible parts of matter are what we call today elementary particles. Depending on the way they interact, these are classified in two classes: leptons and quarks. They are structureless and pointlike up to what we can test at the current resolution, which is down to dimensions of about 10^{-18} m.

The SM describes the universe in terms of quantum field theories, based on a Lagrangian density which has the most general form in describing the mechanics of particle interactions that respect the observed conservation laws. Matter particles themselves are viewed as fermionic (spin- $\frac{1}{2}$) excitations of relativistic quantum fields. They interact with each other via the exchange of force-carrying spin-1 bosons, which are summarized in Table 2.1 and correspond to three of the four known forces that act in nature: the strong force, the electromagnetic force and the weak force (in order of decreasing strength). The fourth and last known force, gravity, is 32 orders of magnitude weaker than the weak force, which in its turn is 4 orders of magnitude weaker than the electromagnetic force, and about 6 orders of magnitude below the strength of the strong force. Therefore the gravitational effects are considered negligible in the SM.

Force	Gauge boson
Strong	g (gluon)
Electromagnetic	γ (photon)
Weak	W^\pm and Z^0 bosons

Table 2.1. *Forces and their corresponding gauge bosons in the Standard Model.*

Interactions between matter particles are introduced into the theory by imposing symmetry conditions on the quantum fields which represent the particles. These conditions arise from conservation laws which we observe in the macroscopic world and which we impose at microscopic level as well, such as charge or momentum conservation. According to Noether's theorem, if an action is invariant under a group of

transformations (symmetry), then there is at least one conserved quantity associated to those transformations. But symmetry also implies dynamics, not only conservation laws. The Lagrangian of the theory is required to be invariant under a group of local phase changes (which means that the phase change depends on the space-time coordinates). Such phase changes are known as gauge transformations, and were introduced for the first time by Weyl in the attempt to describe electromagnetism in the language of General Relativity. Since the equations of motion typically contain space-time derivatives, most Lagrangians will not be invariant under them. To restore invariance, additional gauge fields were added to the theory and their presence insured that the equations of motion remain unchanged. The excitations of these gauge fields were then interpreted as the force-carrying bosons mentioned above.

Both the leptons and the quarks are divided into three families or generations, shown schematically in Table 2.2. The particles in the same leptonic or same hadronic family are related in the sense that they have similar properties and can transform into each other by interacting with a W^+ or W^- boson. Particles in successive generations have all properties in common, except they differ in mass, which increases with the generation number. There is no special connection between the particles in a certain leptonic family and the ones which form the corresponding hadronic family.

	Generation I	Generation II	Generation III	Electric charge	Interactions
Leptons	ν_e (electron-neutrino)	ν_μ (muon-neutrino)	ν_τ (tau-neutrino)	0	Weak
	e (electron)	μ (muon)	τ (tau)	-1	Weak Electromagnetic
Quarks	u (up)	c (charm)	t (top)	+2/3	Weak Electromagnetic
	d (down)	s (strange)	b (bottom)	-1/3	Strong

Table 2.2. *The fermions of the Standard Model and their interactions. The generation number gives the mass hierarchy, mass increasing from the first to the third generation. The electric charge is expressed in units of proton charge $e = 1.602 \cdot 10^{-19}$ Coulomb.*

For every particle listed in Table 2.2, there is also an associated antiparticle, which shares the same properties, such as mass and spin, but has opposite charges.

The two theories which constitute the Standard Model are the Electroweak theory and Quantum Chromodynamics, which are briefly described in the following sections.

2.1 Electroweak theory

Maxwell's work in the middle of the 19th century unified two apparently quite different types of phenomena, electricity and magnetism, into a single theory of electromagnetism. Almost exactly 100 years later, in 1968, Glashow, Salam and Weinberg made another conceptual leap by unifying Maxwell's electromagnetism - in the form of its quantum field theory descendent called quantum electrodynamics or QED and formalized in the 1940s by Feynman, Dyson, Schwinger and Tomonaga - with the theory of the weak interactions. The existence of electroweak interactions was experimentally established with the discovery of the W and Z bosons by the UA1 and UA2 collaborations in 1983 in proton-antiproton collisions [7–10].

Mathematically, the unification is accomplished under a $SU(2)_L \otimes U(1)_Y$ gauge group. $U(n)$ is the group of unitary n -dimensional matrices and for $n = 1$ it represents the space-time dependent rotation in a complex plane. Multiplying the equation of state for a particle by a member of this group produces a phase change. The invariance under phase changes permits the formulation of the theory to be possible independently of the choice of phase. $SU(n)$ denotes the group of special unitary n -dimensional matrices, where special means that the determinant of the matrices must be equal to 1. The $SU(n)$ group has $n^2 - 1$ free parameters, and therefore $n^2 - 1$ generators.

The $SU(2)$ symmetry is connected to the conservation of a charge called “weak isospin”. The weak isospin is analogous to the notion of isospin, but applies to the weak interaction instead of the strong one and to quarks, leptons and electroweak bosons instead of hadrons. Fermions are grouped into pairs of particles that behave the same under the weak interaction. As in the isospin case, members of the same pair are distinguished by the third component of the weak isospin. Type “up” fermions (quarks u, c, t and the neutrinos) have $T_z = +\frac{1}{2}$, while type “down” fermions (quarks d, s, b and the charged leptons) have $T_z = -\frac{1}{2}$. All weak interactions must preserve the weak isospin.

The $U(1)$ symmetry induces the conservation of another charge called the “weak hypercharge”. The weak hypercharge is twice the difference between the electrical charge Q and the third component of the weak isospin, T_z .

The electroweak theory is a chiral theory. A phenomenon is said to be chiral if it is not identical to its mirror image. A Dirac field ψ can be projected onto its left-handed and right-handed chiral components by:

$$\psi_L = \left(\frac{1 - \gamma^5}{2} \right) \psi, \quad \psi_R = \left(\frac{1 + \gamma^5}{2} \right) \psi, \quad (2.1)$$

where $\gamma^5 = i\gamma^0\gamma^1\gamma^2\gamma^3$ and γ^k (for $k = 0, 1, 2, 3$) are the four gamma matrices introduced by Dirac when he used spinors to represent spatial rotations and Lorentz boosts.

It was observed that only left-handed fermions interact weakly: the measurement of longitudinal polarization of the electron emitted in β decay of ^{60}Co showed that electrons emitted in weak transitions are mostly left-handed. This led to the conclusion that parity (a symmetry which transforms a particle into one with the opposite

handedness) is not a symmetry of the universe. The left-handed fermions belong to weak isodoublets, as indicated in Table 2.2, while the right-handed ones transform as weak isosinglets. Originally it was assumed that neutrinos were massless, and only left-handed neutrinos existed (along with their complementary right-handed antineutrinos). After the observation of neutrino oscillations [11], which implies that neutrinos are massive like all other fermions, the revised theory of electroweak interaction now includes both right- and left-handed neutrinos.

A theory of electromagnetic and weak interactions as described above is unsatisfactory due to the fact that it contains four massless gauge bosons, while experimentally only one was observed, namely the photon. Three of these bosons are given by the generators of $SU(2)$, denoted W^1 , W^2 and W^3 , and one corresponds to the $U(1)$ generator, noted here as B^0 . A solution to this problem was proposed in 1964 by Higgs [12], based on earlier work by Goldstone, Nambu, Englert, Brout and Anderson. A new scalar field was introduced, known today as the Higgs field, with a potential function allowing degenerate vacuum solutions with a non-zero vacuum expectation value. Choosing a solution spontaneously breaks the $SU(2) \otimes U(1)$ symmetry of the system and changes it into a $U(1)$ symmetry.

The direct consequence of this is the appearance of two massive charged bosons, known as the W^+ and W^- bosons, which are written as combinations between the W^1 and W^2 generators. The W^3 generator combines with B^0 to form two neutral bosons, one of which is massive (the Z^0 boson) and the other one massless (the photon). For the remainder of this thesis the Z^0 boson will be denoted the Z boson, while the W^+ and W^- bosons will be generically called the W boson. Another interesting consequence is that all fermions acquire mass through the interaction with this new scalar field, bringing the model closer to reality since all fermions were indeed experimentally observed to have mass.

The ratio of the W and Z boson masses can be predicted by the electroweak theory, a prediction verified experimentally with a very high precision. These bosons are heavyweights among the elementary particles: with masses of 80.425 ± 0.038 GeV and 91.1876 ± 0.0021 GeV [13], respectively, the W and Z particles are almost 100 times as massive as the proton, and heavier than entire atoms of iron. The masses of these bosons are significant because they limit the range of the weak force to about 10^{-18} m, as opposed to the electromagnetic force which has an infinite range due to the fact that the photon is massless. Also, from the measured masses of the electroweak bosons the vacuum expectation value of the Higgs field can be calculated, yielding a value of 246 GeV. All three particles have a spin of 1 and a mean life of about $3 \cdot 10^{-25}$ seconds.

Finding the W and Z bosons at their predicted masses in 1983 by the UA1 and UA2 CERN experiments was a major confirmation of the theory and promptly brought Carlo Rubbia and Simon van der Meer their Nobel Prize in physics in 1984, a most unusual step for the Nobel Foundation, which typically rewards remarkable achievements in science many years or decades later.

2.2 Quantum Chromodynamics

Quantum Chromodynamics (QCD) is a gauge theory designed to model the strong interaction. It is based on the $SU(3)$ group, which is a symmetry leading to the conservation of a quantity (or quantum number, or charge) called “colour”. The only elementary particles which interact strongly are the quarks and the antiquarks, via colour carrying gluons which represent the $3^2 - 1 = 8$ generators of the $SU(3)$ group. The colours are labeled red, green and blue for the quarks, and antired, antigreen and antiblue for the antiquarks.

QCD has two peculiar properties, called asymptotic freedom and confinement. Asymptotic freedom means that in very high-energy interactions, the quarks and the gluons interact weakly. This behaviour was predicted from QCD in the early 1970’s by D. Politzer, F. Wilczek and D. Gross [14,15]. For this work they were awarded the 2004 Nobel Prize in physics. Confinement, on the other hand, means that the force between quarks does not diminish as they are separated. Because of this, it would take an infinite amount of energy to separate two quarks. Therefore they are forever bound into neutral colour hadrons such as the proton and the neutron, which also explains the consistent failure of free quark searches.

A neutral colour state, or colour singlet, can be obtained by adding all three colours, all three anticolours or a colour charge and the equivalent anticolour charge. Hadrons can therefore be of two types: (anti)baryons consisting of three (anti)quarks, each of a different (anti)colour, or mesons consisting of a quark of a certain colour and an antiquark which carries the corresponding anticolour. The proton and antiproton are examples of baryons. They consist of two u quarks and one d quark or two anti-u quarks and one anti-d quark, respectively. These are called valence quarks, and they interact with each other via the exchange of gluons, which in turn can split into quark-antiquark pairs or emit more gluons, forming a sea of quarks and gluons. Since the asymptotic freedom means that the strong force decreases in strength as the energy scale of the interaction increases, a proton or an antiproton probed at high energy will consist of approximately non-interacting quarks and gluons (collectively called partons).

Confinement makes QCD calculations of hadronic cross sections at low energy very complicated, due to the fact that bound states exist and perturbation series in the coupling constant cannot be applied. The calculations are therefore split in two parts in accordance to the factorisation theorem, separated in energy by the factorisation scale, μ_F . The low-energy, partly non-perturbative part is described using Parton Distribution Functions (PDFs), which give the momentum distribution of the constituent quarks and gluons. The PDFs are universal and process independent, being determined from fits to data using many different processes studied in many different experiments. The probability of finding a type i parton with a fraction of the hadron momentum between x and $x + dx$ is given by $f_i(x, \mu_F^2)dx$, where $f_i(x, \mu_F^2)$ is the PDF. Although PDFs cannot be derived from first principles, their evolution as a function of μ_F is predictable in perturbation theory. At high energies, where the quarks and gluons can be considered “free” due to the weaker coupling of the strong force, the interactions

can be approximated by perturbation series. Eventually, the “free” quarks and gluons hadronize, resulting in colourless bound states which can be identified as jets in the detector. At the moment, the exact process through which this happens is not fully understood, but several promising models exist. The Lund string model, for example, seems to give an adequate description when tuned to data.

2.3 Z boson production and decay at the Tevatron

The Tevatron is a proton-antiproton collider operating at the center of mass energy of 1.96 TeV. At this energy, the Z boson production is dominated by quark-antiquark annihilation. Figure 2.1(a) shows this interaction, in what is called a “leading order” process. The partons inside the colliding hadrons that do not participate in the hard interaction will generally interact softly, creating what is known as the underlying event. The cross section for this process can be written in the factorised form:

$$\sigma = \sum_{i,j} f_i(x_1, \mu_F^2) \otimes C_{i,j}^P\left(x_1 x_2 s, \frac{Q^2}{\mu_F^2}\right) \otimes \bar{f}_j(x_2, \mu_F^2), \quad (2.2)$$

where Q^2 is the scale of the hard process, x_1 and x_2 are the fractions of the p and \bar{p} momentum taken by the interacting quark and antiquark, s is the square of the centre of mass energy of the $p\bar{p}$ collision, $C_{i,j}^P\left(x_1 x_2 s, \frac{Q^2}{\mu_F^2}\right)$ are the coefficient functions describing the hard process $q_i \bar{q}_j \rightarrow Z$, while $f_i(x_1, \mu_F^2)$ and $\bar{f}_j(x_2, \mu_F^2)$ are the PDFs of the proton and antiproton, respectively.

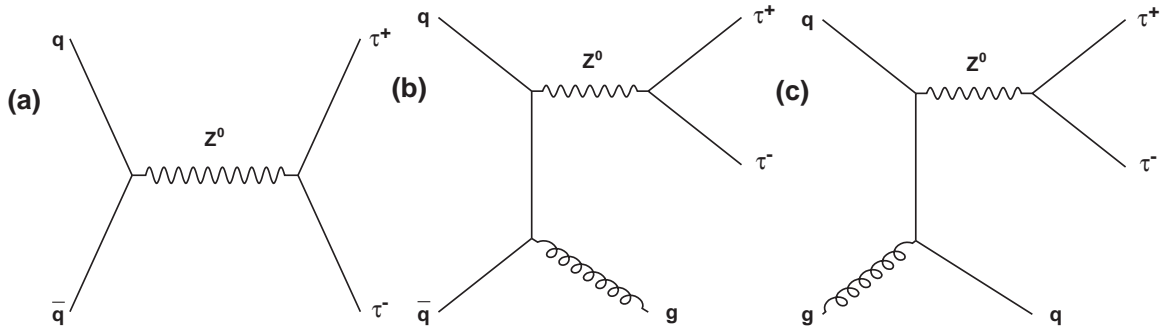


Figure 2.1. Z boson production at the Tevatron, via leading order annihilation of a quark-antiquark pair (a) or produced in association with a gluon (b) or a quark (c), and decay into tau lepton pair.

This process is indistinguishable from one which would be represented by the same Feynman diagram as shown in Fig. 2.1(a), but having a photon emitted by the τ^+ and absorbed by the τ^- , for example, which forms a so called “loop” connecting the final state fermion lines. This process is also indistinguishable from infinitely many

other diagrams containing more such loops. Therefore the exact rate at which such a process happens cannot be calculated in Quantum Field Theories. A full calculation would have to take into account all these diagrams, as well as all higher order processes as the ones illustrated in Fig. 2.1(b) and (c). The calculation of the cross section at leading order (LO) includes only diagrams such as the one shown in Fig. 2.1(a). When one-loop diagrams are added to the LO approximation, the calculation is called to be at next-to-leading order (NLO). Two-loop diagrams must be included for a next-to-next-to-leading order (NNLO) calculation, and so on. Each successive diagram containing more loops would contain more interaction vertices, leading to additional factors of the coupling constant α_s which would be considered in the calculation of the interaction rate. The physical quantities which we try to calculate and compare to measurements, such as the rate of a process, can be expressed as power series with successive terms containing higher powers of the coupling constant. If the coupling constant is small, the perturbative series will converge and higher order terms will become negligible compared to leading order terms.

Another complication arising from this type of treatment is that loop diagrams contain infinities. The momenta of the particles within the loop are not constrained and therefore may extend to infinity, causing the calculations to diverge. This problem was solved via a technique called *renormalisation*. Different types of divergences are treated by being absorbed into different physical parameters. A theory is renormalisable only if a finite set of such input parameters is required. The physical parameters (such as the effective charge of the electron) are expressed in terms of the bare parameters and the expression contains some arbitrary finite functions. Different choices made for these functions define different renormalisation schemes. Most of these schemes introduce an unphysical scale called the renormalisation scale, μ . The coupling constant of the theory becomes a function of μ , and so do the coefficients of the perturbative expansions. This is done in such a way that if calculated to infinite order, the result would be independent of μ . The usual prescription is to set μ to be equal to the typical energy scale associated with the process of interest. This leads to the fact that accurate predictions can now be made by performing calculations to a certain finite order in perturbation theory. These predictions were tested experimentally to a very high precision, a remarkable theoretical success.

With its large mass measured to be 91.1876 ± 0.0021 GeV by the LEP experiments, the Z boson is unstable and will decay immediately into highly energetic decay products. Table 2.3 gives the branching fractions for the Z boson decay. The leptonic decays have the cleanest experimental signature, namely two high momentum charged leptons which are of opposite sign and approximately back-to-back in most cases. In this thesis, the Z boson decay into tau leptons is studied. The tau leptons are the heaviest ones and decay themselves before they can be detected, which makes their detection rather complicated. Chapter 5 gives a detailed description of how this is done in the analysis presented here. However, the tau lepton mass is also what makes them interesting from the point of view of Higgs boson searches, which are detailed below in the next subsection.

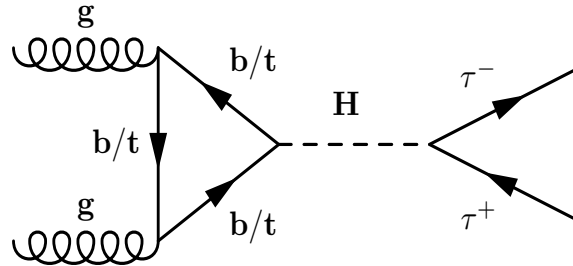
Decay channel	Branching fraction (%)
e^+e^-	3.363 ± 0.004
$\mu^+\mu^-$	3.366 ± 0.007
$\tau^+\tau^-$	3.370 ± 0.008
neutrinos	20.000 ± 0.06
hadrons	69.910 ± 0.06

Table 2.3. *Branching fractions for Z boson decays.*

Measuring the $Z \rightarrow \tau^+\tau^-$ cross section at hadron colliders, even though it can never reach the precision obtained by the LEP experiments, is interesting from many points of view. First of all, it is a useful test of our ability to identify tau leptons in a hadronic environment. Secondly, an excess over the expected Z boson production cross section times the branching ratio of the Z boson into a tau lepton pair, noted as $\sigma \cdot \text{Br}$, would be an indication of a source other than the Z boson for tau lepton pair production. $Z \rightarrow \tau^+\tau^-$ events constitute the main background for $H \rightarrow \tau^+\tau^-$ searches and therefore require a detailed understanding. Thirdly, if a low systematic uncertainty is achieved, this measurement can serve as an independent check on the luminosity measurement. The current systematic uncertainty of the luminosity in the DØ experiment is a relatively large 6.1 %.

2.4 Higgs boson production and decay at the Tevatron

The main Higgs boson production mechanism in $p\bar{p}$ collisions at 1.96 TeV is gluon-gluon fusion, followed by associated production with a W or Z boson. Since the coupling of the Higgs boson is directly proportional to the mass of the fermions to which it couples, the process that is expected to yield the highest production rate is the so called “top loop”, followed by the “bottom loop”, as illustrated in Fig. 2.2. Figure 2.3 (left) shows the cross section for these and other processes as a function of Higgs boson mass. The branching fractions of the Higgs boson into the most significant decay products as a function of its mass are shown in Fig. 2.3 (right).

Figure 2.2. *Production of the Higgs boson through gluon-gluon fusion and subsequent decay into a tau lepton pair.*

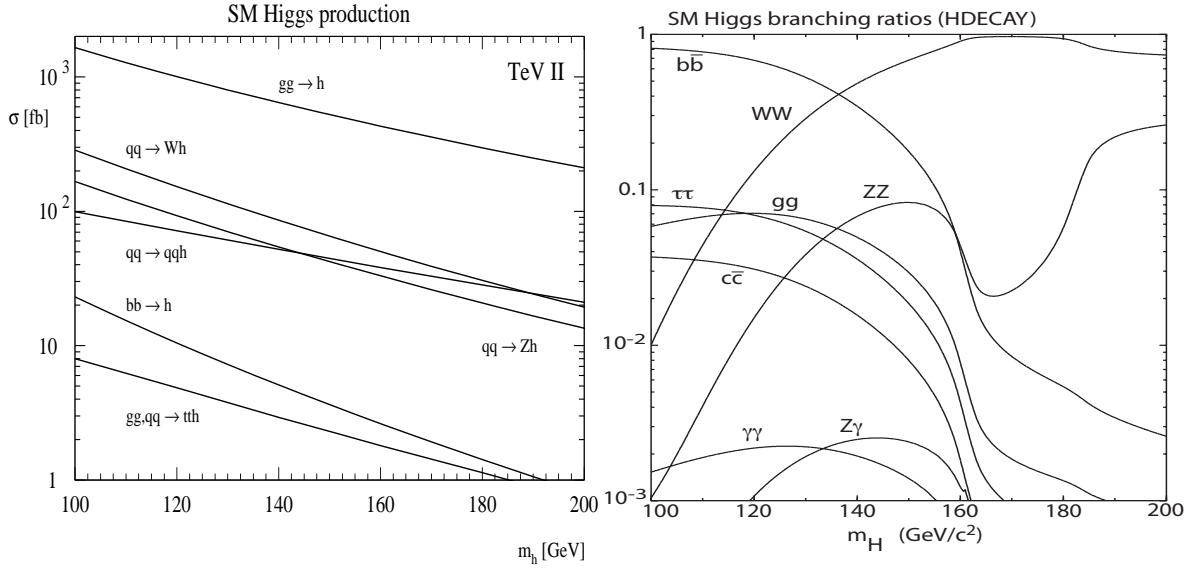


Figure 2.3. Production cross section for the SM Higgs boson in $p\bar{p}$ collisions at center of mass energy $\sqrt{s} = 1.96$ TeV [16] (left) and branching fractions for the SM Higgs boson, calculated with the HDECAY program [17] (right), as a function of m_H .

The mass of the Higgs boson is not known and cannot be predicted from within the Standard Model (SM). Direct searches at LEP set a lower limit for this mass at 114.4 GeV [18]. From precision measurements of cross sections, masses and various couplings of the heavy electroweak gauge bosons performed by the LEP experiments, combined with the latest measurements of the mass of the top quark together with the W boson mass and width from the Tevatron while properly taking into account the common systematic uncertainties, an upper limit of 160 GeV at 95 % confidence level was derived [19]. When the lower mass limit from direct Higgs boson searches at LEP is included in the calculation, the upper limit on its mass becomes 190 GeV.

Two mass regions present a special interest. If the mass of the Higgs boson is between 150 and 180 GeV, the SM would be consistent up to the Planck energy scale. A Higgs boson with a mass lower than 135 GeV could be an indication that the minimal extension of the SM, called the Minimal Supersymmetric Standard Model (MSSM) and discussed briefly in Section 2.6, may be the preferred scenario chosen by nature.

In spite of the lower rate, the channels in which the Higgs boson is produced in association with a W or Z boson decaying into leptons (which are used for triggering and background rejection) are the preferred ones for the low mass SM Higgs boson searches at the Tevatron. This is due to the fact that for masses below about 140 GeV the Higgs boson decays predominantly into $b\bar{b}$ pairs, as can be seen in Fig. 2.3 (right). The two jet signature of such events makes them very difficult to distinguish from the very high multijet background inherent to the $p\bar{p}$ collisions. For the high mass Higgs boson, the decay channel into a pair of W bosons is the most sensitive for searches. Figure 2.4 shows the results of combining the limits obtained in several different channels by the DØ and CDF experiments, in terms of ratio of the limit set for each mass and the cross section of the hypothetical SM Higgs boson with that mass [20].

The WH/ZH with $H \rightarrow b\bar{b}$ and the $\tau^+\tau^-/\gamma\gamma$ channels contribute to the $m_H < 150$ GeV region, while the $H \rightarrow WW$ and $WH \rightarrow WWW$ channels contribute to the $m_H > 115$ GeV region. One can see that so far no mass range was excluded, but this is expected to happen soon, since the sensitivity of the searches reached values very close to the expected SM cross section (in particular for a Higgs boson with a mass of 160 GeV, for example).

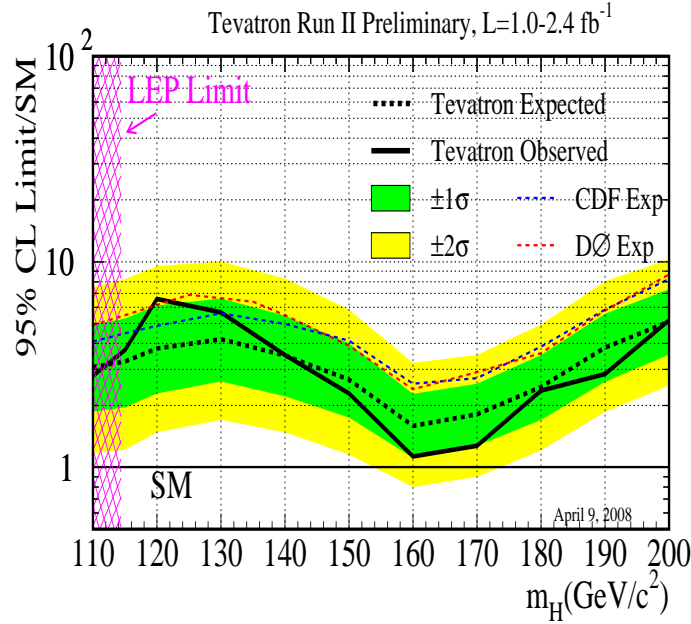


Figure 2.4. Expected (median) and observed 95% C.L. cross section limit ratios for a combination of analyses using $1.0 - 2.4 \text{ fb}^{-1}$ of data collected by the DØ and CDF experiments, as a function of m_H . The limits are expressed as a multiple of the SM prediction for test masses for which both experiments have performed dedicated searches in different channels. The bands indicate the 68 % and 95 % probability regions where the limits can fluctuate, in the absence of signal. Also shown are the expected upper limits obtained for all combined CDF channels, and for all combined DØ channels [20].

The search for a Higgs boson produced by gluon-gluon fusion proves to be more challenging, due to the large background from QCD jets and from Z boson hadronic decays, which make the search for $p\bar{p} \rightarrow H \rightarrow b\bar{b}$ very difficult, in spite of the high cross section times branching ratio of this process. However, the Higgs boson decay into a pair of tau leptons exhibits a significantly lower background from multijet processes and a relatively large branching ratio for masses below 140 GeV, which makes it an interesting channel for Higgs boson searches. Furthermore, in the MSSM the coupling of the Higgs boson to tau leptons is significantly increased under certain conditions [21], making the searches in this channel a very useful tool for constraining the parameters of the model as well as a very promising way to discovery.

2.5 Problems with the Standard Model

The combination of the Electroweak and Quantum Chromodynamics theories into one coherent description of matter and its interactions based on the $SU(3) \otimes SU(2) \otimes U(1)$ group of symmetry, known today as the Standard Model of particle physics, has been very successful so far. It predicted particles which were eventually discovered and relationships between parameters which were verified at a high level of precision. There are however a number of problems which make us believe that the Standard Model cannot be the whole story. First, the *vacuum energy problem*. This is one of the issues related to the completeness of the electroweak theory that scientists have not yet addressed, although it seems to hold an important clue for a unified theory of all known interactions. The Higgs potential contributes a field-independent constant term:

$$\rho_{\text{H}} \equiv \frac{M_{\text{H}}^2 v^2}{8} \quad (2.3)$$

which plays the role of vacuum energy density. When we consider gravitation, adding a vacuum energy density ρ_{vac} is equivalent to adding a cosmological constant term to Einstein's equation. Although recent observations raise the possibility that the cosmological constant may indeed be different from zero, they also show that the vacuum energy density must be very small:

$$\rho_{\text{vac}} \leq 10^{-46} \text{GeV}^4. \quad (2.4)$$

Given that $v = (G_F \sqrt{2})^{-\frac{1}{2}} \simeq 246 \text{ GeV}$ and a lower limit on M_{H} was set experimentally at 114.4 GeV, we find that the contribution of the Higgs field is

$$\rho_{\text{H}} \geq 10^8 \text{GeV}^4, \quad (2.5)$$

which is 54 orders of magnitude larger than the upper bound inferred from the cosmological constant. Either we must find a separate principle to annihilate the vacuum energy density of the Higgs field, or hope that a proper quantum theory of gravity, in combination with the other interactions, will resolve the puzzle of the cosmological constant [22].

Another issue related to the Higgs boson mass is the *hierarchy problem*. From fits to many SM parameters such as the mass and the width of the W and Z bosons, the top mass, the tau lepton polarisation, forward-backward asymmetries and others, an upper limit of 144 GeV was set on the Higgs boson mass with a confidence level (C.L.) of 95% [19]. But loops of virtual SM particles lead to quantum corrections to M_{H} of the order of the highest energy scale at which the SM is valid. If this scale is as large as the Planck scale, namely about 10^{19} GeV , the cancellation of such corrections needed to bring the Higgs boson mass down to the electroweak scale of about 100 GeV is extremely unnatural. There are other reasons why the Standard Model cannot be a final “theory of everything”. One of the most important ones is that gravity is not included in the theory, as its addition proved to be highly non-trivial. A theory which does not include gravity is clearly incomplete. In addition, the particle masses and field coupling strengths are free parameters which must be measured by experiments and cannot be predicted by the theory. The mechanism for electroweak symmetry breaking

is not predicted by the theory, nor is the reason why there are three families of leptons and quarks. Another mystery is the significant mass difference between the fermions from different families. Much is still left to be discovered and explained, even after (or if) the Higgs boson is found.

2.6 The Minimal Supersymmetric Standard Model

An extension of the Standard Model, called supersymmetry, often abbreviated as SUSY, offers a natural solution to the hierarchy problem. The new theory is based on an additional symmetry that relates each elementary particle of a certain spin to another particle that differs by half a unit of spin. The latter is known as the superpartner of the former. Since the particles of the Standard Model do not have this property, supersymmetry must be a broken symmetry allowing the supersymmetric partners of the SM particles to be heavy. If one postulates a bosonic partner for each fermion, the total correction to the Higgs mass remains naturally small, since the bosonic and fermionic contributions to the one-loop corrections are of opposite signs.

Supersymmetry has also the appealing feature that the running of the coupling strengths for all interactions now leads to unification in a single point, provided that the sparticle masses are of the order 1 TeV [23]. Also, the mathematical framework of SUSY makes the addition of gravity less problematic since it allows spin-2 particles to be introduced and gravity is postulated to be mediated by a spin-2 particle called graviton. Finally the lightest supersymmetric particle would be a good dark matter candidate.

The simplest realistic supersymmetric model is the Minimal Supersymmetric Standard Model (MSSM) [24,25]. In addition to supersymmetric partners to all SM particles, it requires two complex Higgs doublets. One Higgs doublet couples only to the down-type fermions and the other couples only to the up-type fermions. The Higgs doublets have 8 degrees of freedom, 3 of them being constrained by the electroweak gauge bosons. This leaves a Higgs sector consisting of 5 physical Higgs bosons: two charged (H^\pm) and three neutral scalar bosons, two of them being CP-even, typically denoted h and H , and one CP-odd, A . At tree level, the Higgs sector is fully specified by two parameters, usually chosen to be the mass of the CP-odd Higgs boson, m_A , and the ratio of the vacuum expectation values of the two Higgs doublets, denoted as $\tan\beta$. The main production mechanism of neutral MSSM Higgs bosons at hadron colliders is, as in the case of the SM Higgs boson, the gluon-gluon fusion. However, the neutral Higgs boson production through $b\bar{b}$ annihilation is heavily enhanced at high values of $\tan\beta$, on which it depends quadratically.

Figure 2.5 shows the NLO cross sections for Higgs production via the $b\bar{b} \rightarrow H/A$, calculated with the code from [26], and $gg \rightarrow H$ (obtained using HIGLU [27] and HDECAY [17]), as well as their sum, calculated for $p\bar{p}$ collisions at $\sqrt{s} = 1.96$ TeV, for a supersymmetric axial Higgs boson in the case $\tan\beta = 30$. For comparison, the SM cross sections for the same processes producing a SM Higgs boson are also shown.

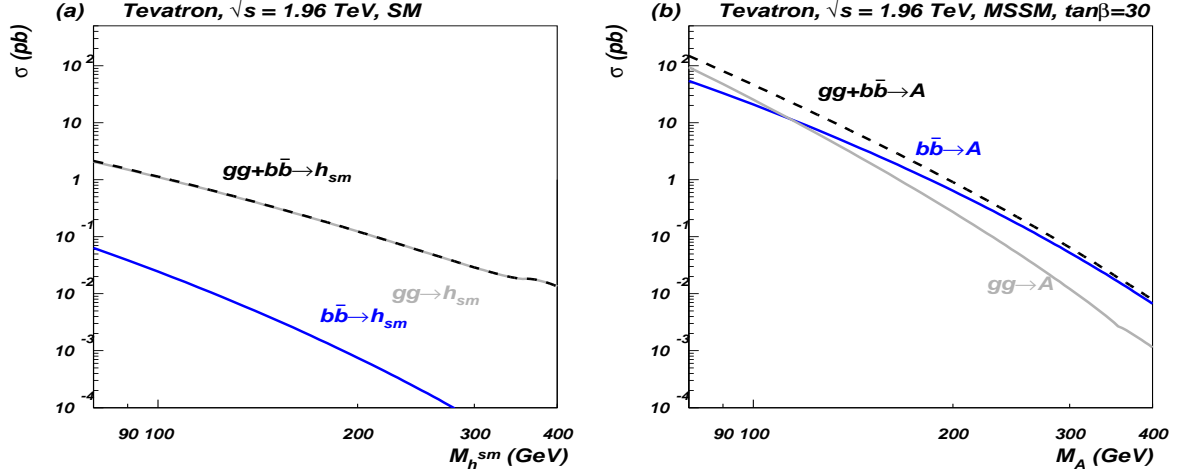


Figure 2.5. NLO production cross section for the SM Higgs boson in $p\bar{p}$ collisions at center of mass energy $\sqrt{s} = 1.96$ TeV, as a function of m_H (left) and as a function of m_A for a MSSM Higgs boson, at $\tan\beta = 30$ [28].

The neutral scalar Higgs bosons are mixtures of the real parts of the vacuum states of the two Higgs doublets. Their masses are calculated as eigenvalues of the mass matrix, with the following results:

$$m_{H,h}^2 = \frac{1}{2} \left[m_A^2 + M_Z^2 \pm \sqrt{(m_A^2 + m_Z^2)^2 - 4m_A^2 M_Z^2 \cos^2(2\beta)} \right]. \quad (2.6)$$

This leads to the important upper bound:

$$m_h \leq \min(m_A, M_Z) \cdot |\cos(2\beta)|, \quad (2.7)$$

which predicts that one of the neutral Higgs scalars must be lighter than the Z boson. However, the radiative corrections are already important at 1-loop level, the dominant contribution coming from top-stop loops. When all corrections are taken into account, a new limit of $m_h \leq 135$ GeV is obtained [29–31].

The SM coupling of the CP-odd Higgs boson to the b quark is enhanced by a factor of $\tan\beta$, and therefore the production cross section is enhanced by $\tan^2\beta$. The coupling of the CP-even states, h and H, are enhanced by $-\sin\alpha/\cos\beta$ and $\cos\alpha/\cos\beta$ respectively, where α is the mixing angle between h and H and is given by:

$$\cos^2(\beta - \alpha) = \frac{m_h^2(m_Z^2 - m_h^2)}{m_A^2(m_H^2 - m_h^2)} \quad (2.8)$$

The leading decay modes for a low mass A are $b\bar{b}$ (90 %) and $\tau^+\tau^-$ (9 %), which makes the study of events containing pairs of tau leptons to be of particular interest.

If supersymmetry is indeed modeling what happens in nature, a sufficiently high $\tan\beta$ could lead to an observable additional peak beyond the one of the Z boson in the di-tau mass spectrum. Large $\tan\beta$ values are favoured by some models, as it naturally explains the difference in mass between the top and the bottom quarks [32].

Scanning the whole parameter space of the Minimal Supersymmetric Standard Model is a daunting task. In a constrained model, where unification of the $SU(2)$ and $U(1)$ gaugino masses is assumed, the most relevant parameters of the model are the common scalar mass M_{SUSY} , the mixing parameter X_t (which represents the off-diagonal element of the squark mixing matrix), the mass parameter μ , the gaugino mass term M_2 and the gluino mass $m_{\tilde{g}}$. Four benchmark scenarios for MSSM Higgs boson searches were defined in [33,34]: two m_h^{max} scenarios, in which the Higgs boson mass is maximally shifted by radiative corrections, with the above defined parameters $M_{\text{SUSY}} = 1 \text{ TeV}$, $X_t = 2 \text{ TeV}$, $\mu = \pm 0.2 \text{ TeV}$, $M_2 = 0.2 \text{ TeV}$ and $m_{\tilde{g}} = 0.8 \text{ TeV}$ and two no-mixing scenarios, in which the Higgs boson mass is relatively modestly shifted by radiative corrections, defined by parameters $M_{\text{SUSY}} = 2 \text{ TeV}$, $X_t = 0 \text{ TeV}$, $\mu = \pm 0.2 \text{ TeV}$, $M_2 = 0.2 \text{ TeV}$ and $m_{\tilde{g}} = 1.6 \text{ TeV}$.

Combined limits from the four LEP experiments interpreted within these four benchmark scenarios have excluded at 95 % confidence level for all $\tan\beta$ values the existence of MSSM Higgs bosons with a mass below 92.9 GeV for h and 93.4 GeV for A. Values of $\tan\beta$ lower than 0.7 - 2 were excluded for all $m_{A/h}$ values [35].

The allowed values for $\tan\beta$ were further constrained at the Tevatron. Searches for MSSM Higgs bosons have been carried out by the DØ and CDF experiments in the following channels [36–38] (here ϕ denotes all three neutral MSSM Higgs bosons, $\phi = h, H, A$): $b\bar{b}\phi, \phi \rightarrow b\bar{b}$ (with one additional tagged b jet), $p\bar{p} \rightarrow \phi \rightarrow \tau^+\tau^-$ (inclusive) and $p\bar{p} \rightarrow t\bar{t} \rightarrow H^\pm W^\pm b\bar{b}$, $H^\pm \rightarrow \tau\nu_\tau$.

It was shown [39] that the bounds obtained from the $b\bar{b}\phi, \phi \rightarrow b\bar{b}$ channel depend very sensitively on the radiative corrections affecting the relation between the bottom quark mass and the bottom Yukawa coupling. In the channel with $\tau^+\tau^-$ final states, on the other hand, compensations between large corrections in the Higgs boson production and the Higgs boson decay occur, which implies the cancellation of the leading dependence of these radiative corrections. A subdominant parametric dependence on these corrections remains in the $\tau^+\tau^-$ channel, which may lead to variations of a few tens of percent in the τ -pair production rate, which is lower than variations of the rate by up to factors of a few in the case of bottom-quark pair production. This makes the $\tau^+\tau^-$ channel more robust and therefore an excellent candidate for searches of MSSM Higgs boson production. At the Tevatron, the tightest limits in the $\tan\beta - m_A$ plane for the MSSM are set using this channel by the CDF experiment using 1.8 fb^{-1} of data [40]. A very similar result was found in the analysis detailed below.

3

Experimental setup

3.1 The Tevatron

The Tevatron is the highest energy proton-antiproton collider to date, situated on the grounds of Fermi National Accelerator Laboratory (Fermilab) near Chicago, USA. The protons and antiprotons are produced and accelerated using a chain of eight accelerators, following the path shown in Fig. 3.1.

The first step is using the Cockcroft-Walton apparatus to accelerate negatively charged hydrogen ions up to 750 keV. The Cockcroft-Walton is basically a voltage multiplier that converts alternating current (AC) or pulsing direct current (DC) electrical power from a low voltage level to a higher DC voltage level. It is made up of a voltage multiplier ladder network of capacitors and diodes, and different small scale versions of it can be found in most television sets. It was invented by Heinrich Greinacher, a Swiss physicist, in 1919, but was named after John D. Cockcroft and Ernest T. S. Walton when they used it in 1932 to produce the first artificial nuclear disintegration in history, which eventually led to the development of nuclear power and nuclear weapons. The discovery brought the two physicists their Nobel Prize in 1951.

Bunches of these hydrogen ions which leave the Cockcroft-Walton are then accelerated up to 400 MeV inside a 130 meters linear accelerator (LINAC). When they reach this energy, the ions are stripped of their electrons by going through a carbon foil and the resulting protons are accelerated up to an energy of 8 GeV by a synchrotron with a circumference of 475 meters called the Booster. From there they enter the Main Injector ring, where they are accelerated to either 120 or 150 GeV.

The protons with energies of 120 GeV are used to produce antiprotons by colliding them with a nickel target. This is a very inefficient process and requires about 10^5 protons in order to produce and collect one antiproton from the multitude of secondary particles resulting from such collisions. The Antiproton Source consists, besides the target, of two synchrotrons with a mean radius of 90 m, called the Debuncher and the Accumulator. The Debuncher captures the antiprotons coming from the target, while the Accumulator continuously stores them (or “stacks” them). Since the stacking efficiency depends on the amount of antiprotons already stacked, the antiprotons from the Accumulator are regularly transferred to a different ring of permanent magnets specially designed for antiproton storage, called the Recycler and situated inside the Main Injector tunnel.

When enough antiprotons have been stored in the Accumulator and Recycler, they are transferred into the Main Injector ring, where they are accelerated up to 150 GeV and injected into the Tevatron in the form of 36 bunches, preceded just before by the

injection of 36 bunches of protons at the same energy which were accelerated inside the Main Injector as well. The bunches of protons contain typically $2.4 \cdot 10^{11}$ protons, while the antiprotons bunches contain currently about 10^{11} antiprotons. The length of each bunch is 37 cm. They are grouped in three trains with a $2.2 \mu\text{s}$ separation between them. The bunch to bunch separation is 396 ns, which also gives their collision frequency.

With its radius of approximately one kilometer, the Tevatron is at this time the largest working accelerator in the world. It is used to accelerate the protons and antiprotons up to an energy of 980 GeV, which means they will be traveling in opposite directions inside a beam pipe with a diameter of a few centimeters at 494 km/h below the speed of light. The Tevatron ring is divided into six regions of similar geometry named using the first six letters of the alphabet, each of them being subdivided in six smaller sections numbered from 0 to 5. The beams are made to collide at two points, where the DØ and CDF experiments are located. DØ took its name from the location along the ring where it is placed, while CDF, the name of the experiment placed at position B0, stands for the Collider Detector at Fermilab.

The center of mass energy of these collisions is 1.96 TeV. Until the Large Hadron Collider (LHC) situated at CERN near Geneva, Switzerland, will start producing proton-proton collisions at its designed center of mass energy of 14 TeV, this remains the highest beam energy value ever obtained in the world. The highest luminosity ever achieved by the Tevatron is a world record for hadron colliders as well: $2.85 \cdot 10^{32} \text{ cm}^{-2}\text{s}^{-1}$. During a typical store (~ 20 hours) the luminosity decreases exponentially from about $2 - 2.5 \cdot 10^{32} \text{ cm}^{-2}\text{s}^{-1}$ to approximately $1 - 2 \cdot 10^{31} \text{ cm}^{-2}\text{s}^{-1}$. Until present (April 2008) an integrated luminosity of 3.9 fb^{-1} was delivered to each of the two experiments.

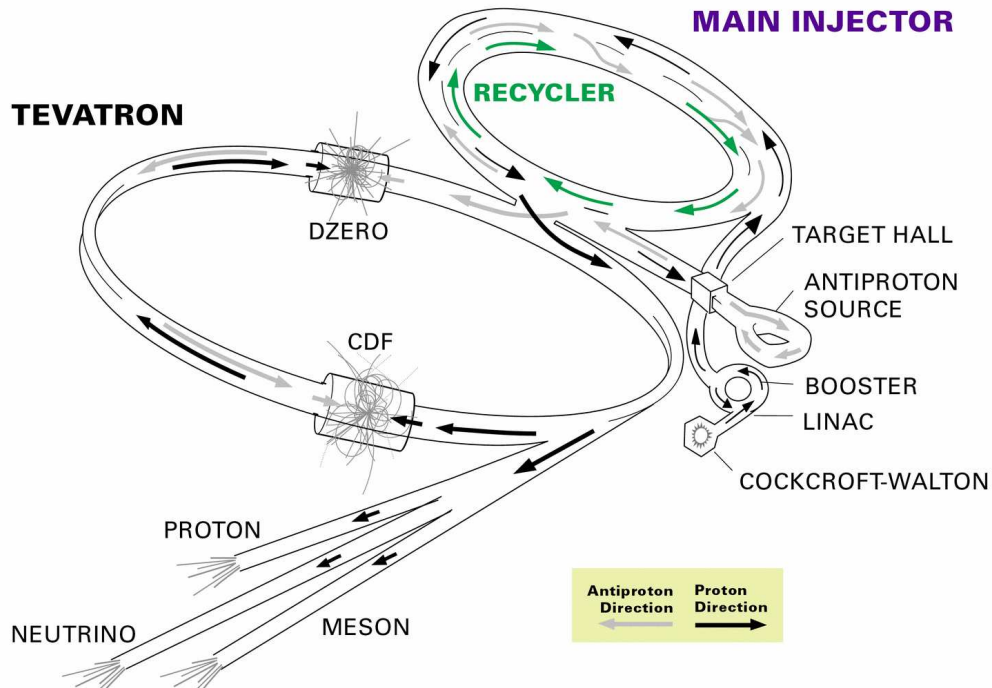


Figure 3.1. Fermilab's accelerator chain.

3.2 The DØ detector

DØ is a general-purpose detector, with axial and forward-backward symmetry, designed for the identification and energy measurement of particles resulting from $p\bar{p}$ collisions which take place approximately in the center of the detector. A longitudinal section view of the detector is shown in Fig. 3.2. It comprises four major subsystems: a central tracking detector, an uranium/liquid-argon calorimeter, a muon spectrometer and a triggering system. Additional subsystems are used for data storing, as well as luminosity and radiation monitoring. These will be briefly described below. For a complete description of the DØ detector the reader is referred to [41].

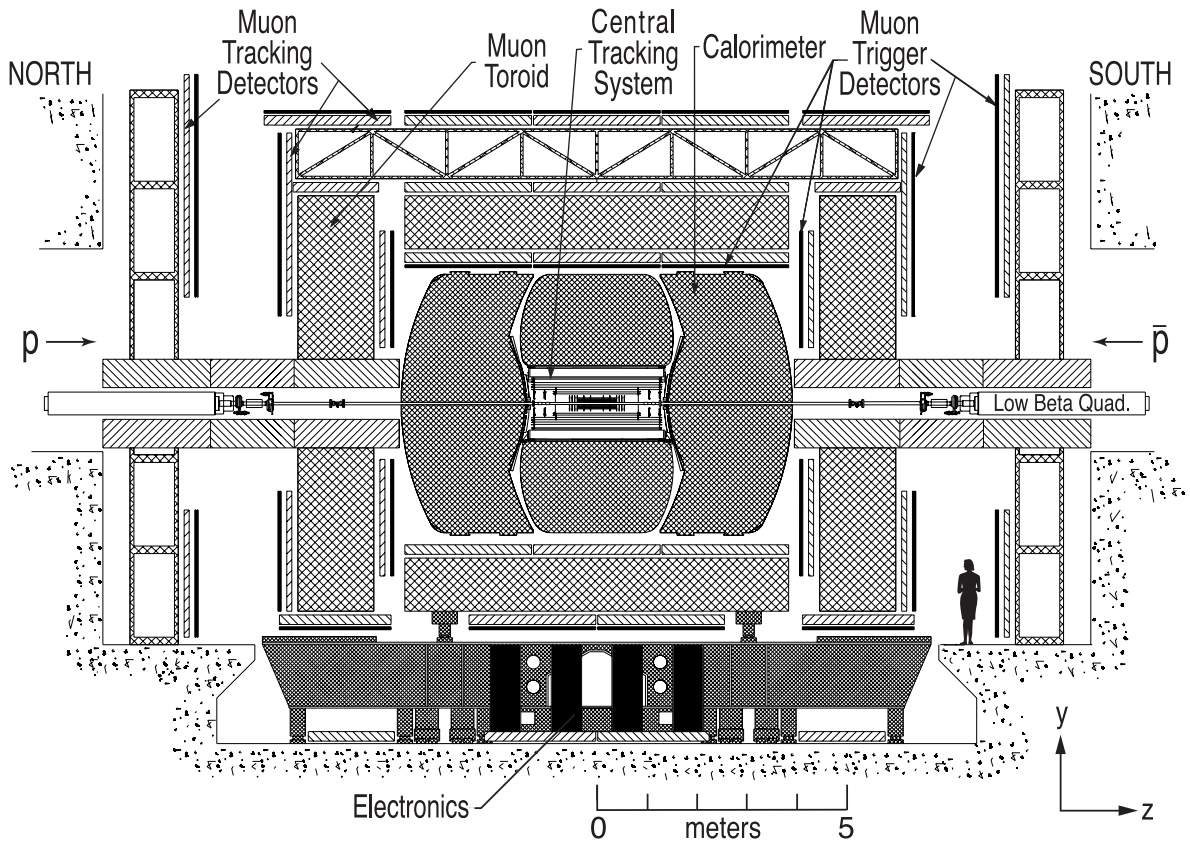


Figure 3.2. Longitudinal section view of the DØ detector.

3.2.1 Coordinate system

The spatial coordinates of the DØ detector are defined using a righthanded Cartesian system with the origin in the center of the detector. The positive z -axis is the direction of the protons, the positive y -axis points upwards and the positive x -axis points out of the Tevatron ring. Since the proton-antiproton interactions have no preference of

direction in the $x - y$ plane, a system of cylindrical coordinates is used in most studies, with the z direction as axis of symmetry. The polar angle θ is measured with respect to the positive z direction, while the azimuthal angle ϕ is measured with respect to the positive x direction. The radial distance r is the displacement from the z axis. The θ angle is often replaced by a variable called pseudo-rapidity and defined as

$$\eta = -\ln \tan \frac{\theta}{2}. \quad (3.1)$$

When $E \gg m$, which is usually the case for high energy particles, and for angles above about 1° the pseudo-rapidity is a good approximation for the rapidity, which is defined as

$$y = -\frac{1}{2} \ln \left(\frac{E + p_z}{E - p_z} \right), \quad (3.2)$$

where E is the energy of the particle and p_z is its momentum in the z direction. Differences in rapidity are invariant under Lorentz boosts along the z direction, making the rapidity and the pseudo-rapidity particularly useful variables at hadron colliders, where the center-of-mass system of the colliding partons is different from the rest frame of the laboratory.

3.2.2 Central tracking system

The central tracking system consists of the Silicon Microstrip Tracker (SMT) and the Central Fiber Tracker (CFT), situated inside a solenoidal magnet. It is the most central piece of the DØ detector, surrounding the beryllium beam pipe with an outer diameter of 38.1 mm. The outer diameter of the tracking system was limited by the available space within the central calorimeter vacuum vessel (2.73 m in length and 1.42 m in diameter), along with the necessity of placing a solenoidal magnet inside the same cavity.

The solenoid magnet is a cylinder with a radius of 52 cm and a length of 2.7 m, and it can operate safely and stably at either polarity. The magnetic field produced is oriented parallel to the beam direction and is approximately uniform inside the magnet, having a value of 2 Tesla. A schematic view of the central tracking system is shown in Fig. 3.3.

The two tracking detectors locate the primary interaction vertex with a resolution of about $35 \mu\text{m}$ along the beamline. The high resolution of the vertex position allows a good measurement of lepton p_T , jet transverse energy (E_T) and missing transverse energy (\cancel{E}_T). The transverse momentum resolution for central tracks ($|\eta| < 2$) is between $(1.5 - 4)\%$ for tracks with $p_T = 1 \text{ GeV}$, $(3 - 10)\%$ for tracks with $p_T = 10 \text{ GeV}$ and $(15 - 30)\%$ for tracks with $p_T = 100 \text{ GeV}$. The resolution stays close to the lower limit of these intervals within the region fully covered by the CFT ($|\eta| < 1.6$) and degrades rapidly outside this region.

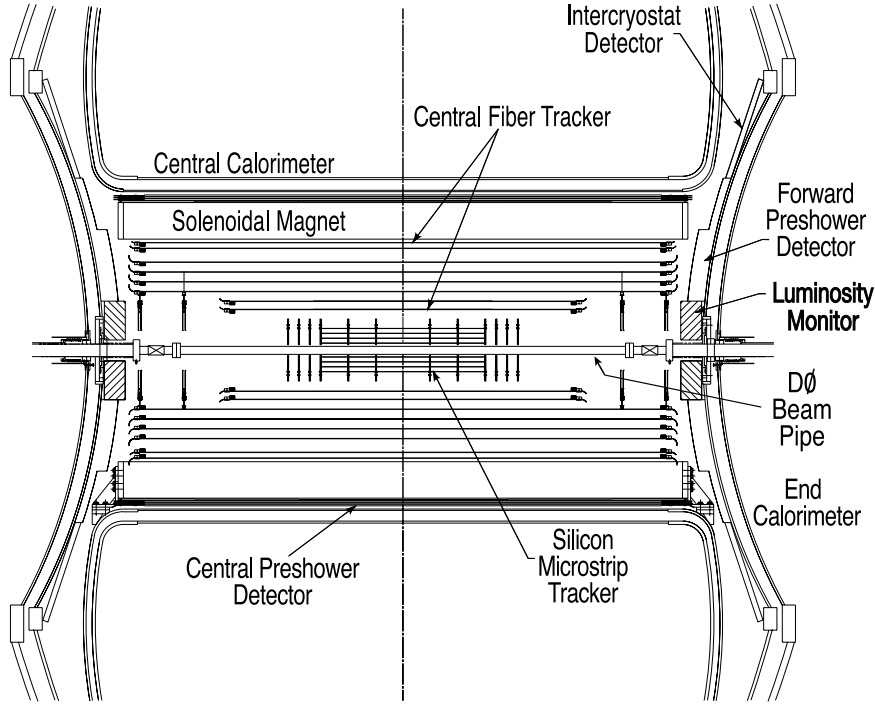


Figure 3.3. Cross-section view of the central tracking system in the $x - z$ plane.

Silicon Microstrip Tracker

The SMT provides both tracking and vertexing over nearly the full η coverage of the calorimeter and muon systems. The length and the design of the device is set by the relatively large length of the interaction region ($\sigma_{vertex\ z} \approx 25$ cm). In order to have the tracks generally perpendicular to the detector surfaces for all η in spite of the long interaction region, a design of barrel modules interspersed with disks in the center and assemblies of disks in the forward (high η) regions was chosen. The barrel detectors primarily measure the $r - \phi$ coordinate and the disk detectors measure $r - z$ as well as $r - \phi$. Therefore at high η the vertices are reconstructed in three dimensions by the disks, while at low η the vertices are reconstructed using the barrels and the CFT.

An isometric view of the SMT is shown in Fig. 3.4. The detector consists of six barrels and sixteen disks. The barrels have four silicon readout layers each. The first two layers counting from inside out have twelve silicon modules called “ladders”, while the outer two layers have twenty-four ladders each. The centers of the barrels are situated at $|z| = 6.2, 19.0$ and 31.8 cm. Each barrel is capped at high $|z|$ with a disk of twelve double-sided wedge detectors, called “F-disk”, and forward of the three disk/barrel assemblies on each side there is a unit consisting of three F-disks. The F-disks have their centers at $|z| = 12.5, 25.3, 38.2, 43.1, 48.1$ and 53.1 cm. In the far forward regions, two disks with larger diameter, called “H-disks”, provide tracking at high $|\eta|$. The H-disks consist of twenty-four wedges, each comprising two back-to-back

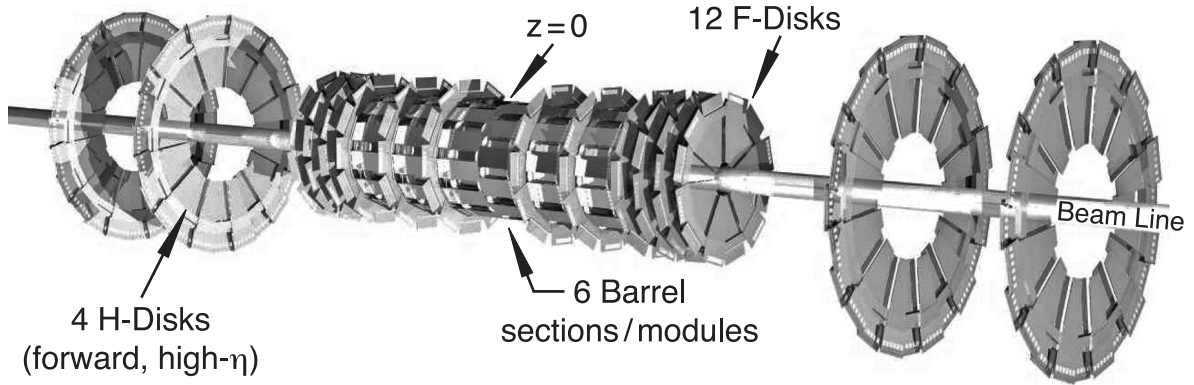


Figure 3.4. *Isometric view of the Silicon Microstrip Tracker.*

single-sided “half” wedges. There are therefore 432 ladders, 144 F-wedges and 96 full H-wedges in the SMT, with each side of the wedges being read separately, which leads to a total of 912 readout modules and 792,576 channels. The SMT is read out by custom-made 128-channel SVXIIe readout chips.

The sensors are made of silicon and come in seven varieties which use either single-sided, double-sided or double-sided double-metal technologies. The readout strips are placed at distances (“pitch”) which vary between 40 and 153.5 μm , with most of them having a pitch of 50 μm on the p-side and 62.5 μm on the n-side. The readout strips are made of n^+ -doped silicon on one side of the sensor and p^+ -doped silicon on the other side. The bulk is depleted of charge carriers by applying a bias voltage to the sensors. When a charged particle traverses the sensor, charge carriers are created and collected by the nearest strips, leading to a detectable electric signal called “hit”. The tracks of the charged particles are later reconstructed by combining the hits registered by several sensors.

The barrel ladders are supported by beryllium bulkheads, half of them containing cooling channels and the other half used for support. The disks are supported by beryllium rings. The overall support of the SMT (excluding the H-disks) is provided by a double-walled carbon fiber cylinder. The H-disks are located on separate mounts suspended from the third layer of the CFT. Cooling of the detector is necessary to reduce bulk damage to the silicon, which would lead to type inversion and increase in depletion voltage. It is done using a water and 30 % ethylene glycol mixture supplied at -10°C which flows through the channels machined in the beryllium bulkheads.

High levels of radiation could damage the SMT sensors as well, mostly through displacement or build-up of crystal defects due to non-ionizing energy of the particles produced in the $\text{p}\bar{\text{p}}$ interaction or from the beam halo. The most affected regions are the ones closer to the beam pipe, as the flux of charged particles decreases as $r^{-1.68}$ [42]. Radiation damage is known to produce linear increase of the leakage current with the fluence, forcing the use of increased depletion voltage. However, since the limit to which the depletion voltage can be increased without causing break-down is about

100 V, significant losses to Layer 1 of the SMT are expected when about 4 fb^{-1} of integrated luminosity will be accumulated.

To monitor and prevent accidental irradiation due to beam deviation and increased halo, two separate radiation monitoring systems are used. On each side of the detector, outside the calorimeter end caps, four argon filled gas counters with a large diameter anode cylinder were mounted, called Beam Loss Monitors (BLMs) [43,44]. They have the capacity of triggering beam abort in case of excessive amounts of radiation registered by at least two of the eight devices. Additionally, a system of 48 diodes known as “radiation monitors” [45], similar in design to the ones used by the OPAL experiment [46], were placed on some of the F-disks and H-disks, providing a precise integrated dose measurement as well as a radiation history over several seconds in case of beam abort. They have the capacity to abort the beam as well, but this was never used. Instead, alarm signals are sent to the DØ Control Room and to the Accelerator Division to alert operators about unusually high radiation doses when they exceed certain acceptable limits. An estimate of the radiation dose accumulated by the SMT as a function of time for the first two years of collisions at $\sqrt{s} = 1.96 \text{ TeV}$, made using the radiation monitors, can be found in [47].

To compensate for the decrease in the quality of tracking due to irradiation, a new layer of silicon detectors, called Layer 0, was installed recently between the beam pipe and Layer 1 of the SMT. This lead to an improvement in tracking and vertex finding resolution for the time being, and studies show that it will overcome the radiation damage expected for Layer 1 in the coming years of running, when the integrated luminosity will increase by a factor of two or three.

Central Fiber Tracker

The CFT consists of scintillating fibers mounted on eight concentric support cylinders and occupies the radial space from 20 to 52 cm from the center of the beam pipe. It provides coverage for the $|\eta| < 1.6$ region. To accomodate the forward SMT H-disks, the two innermost cylinders are 1.66 m long, while the outer six are 2.52 m long. Each cylinder supports one doublet layer of fibers oriented along the beam direction (the “axial” layer) and a second doublet layer oriented at a small stereo angle in ϕ (which is either $+3^\circ$ or -3°), called the “stereo” layer.

The fibers have a diameter of $835 \mu\text{m}$ and are made of polystyrene doped with two organic fluorescent dyes. The charged particles passing the fibers cause excitations to the polystyrene, which transmits them rapidly to the first dye (paraterphynyl). The paraterphynyl has a rapid fluorescence decay (few nanoseconds), but the light emitted, with a wavelength of 340 nm, has a very short mean free path of only a few hundred microns in polystyrene. The role of the second dye (3-hydroxyflavone) is to absorb the 340 nm photons and re-emit them at 530 nm, which is a well transmitted wavelength in polystyrene. The light is observed from only one end of the scintillating fiber. The opposite end of each fiber was turned into a mirror using aluminium coating which provides a reflectivity of about 90 %.

The scintillating fibers are coupled to clear fiber waveguides which carry the scintillation light to the Visible Light Photon Counters (VLPCs) for readout. The VLPCs are semiconductor photodetectors which operate at a nominal temperature of 9 K and are capable of detecting single photons. They provide a fast response, very good quantum efficiency ($> 75\%$) and high gain (22,000 – 65,000 electrons per incoming photon) when transforming the light from the scintillating fibers into an electrical signal. The CFT requires 76,800 channels of VLPC readout.

3.2.3 Calorimeter system

The DØ calorimeter system consists of three sampling calorimeters, each housed in its own cryostat which keeps the detector temperature at 90 K. Between the cryostats there are layers of scintillator tiles to compensate for the lack of sensors in the η region where the calorimeters meet, called the intercryostat detector (ICD). Liquid Argon is the active medium used to sample the ionization produced by charged particles transversing the calorimeter, while the absorber plates are made of different materials, depending on their location.

The three calorimeters and their different modules are schematically shown in Fig. 3.5. The Central Calorimeter (CC) provides coverage up to $|\eta| < 1$, while the two end calorimeters, ECN (north) and ECS (south) extend the coverage to $|\eta| \approx 4$.

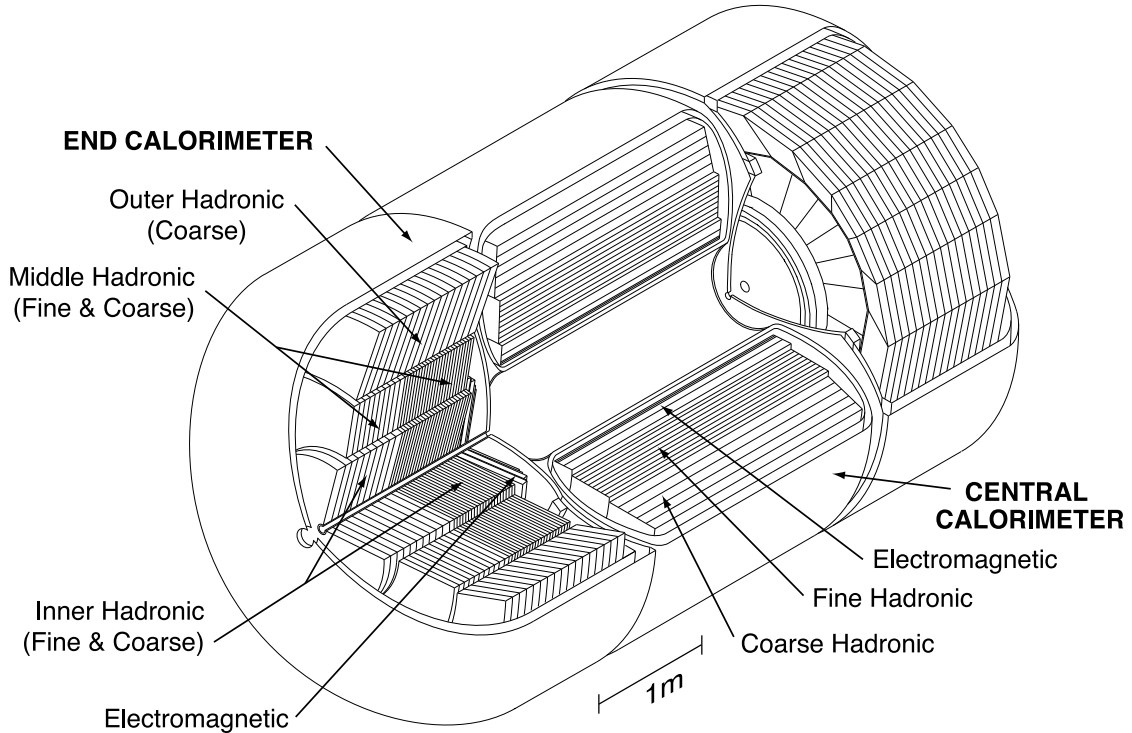


Figure 3.5. *Isometric view of the central and two end calorimeters.*

High energy electrons passing through matter emit photons via bremsstrahlung. These photons produce pairs of electrons and positrons, which in turn emit more photons through bremsstrahlung. This process of forming an electromagnetic (EM) “shower” or cascade continues until the energy of the resulting electrons and positrons is lower than 10 MeV. At that point, the electrons will start to lose energy via ionization rather than bremsstrahlung, therefore making their presence detectable.

Hadronic particles, on the other hand, interact with the atomic nuclei predominantly via the strong force when they pass through material. They also produce secondary particles that go on to produce more particles with decreasing energy thus forming a hadronic shower. As in the case of electrons, the lower energy particles are detected by their ionization loss. The average distance traveled by particles in a hadronic shower before an interaction takes place is typically longer than that in an electromagnetic shower and hence the hadronic showers penetrate further into the calorimeter. This explains the order and nomenclature of the different calorimeter modules in Fig. 3.5.

The DØ calorimeter is segmented into cells with sizes comparable to the transverse sizes of showers: 1-2 cm for the EM showers and 10 cm for hadronic showers. Each cell consists of alternating layers of absorbing metallic material used to induce shower formation and readout copper plates coated with a highly insulating material (G-10 and carbon loaded epoxy), all submersed inside the active material (liquid Ar) in which atoms are ionized by the passage of charged particles. The electric field is established by grounding the metal absorber and connecting the resistive surfaces of the signal boards to positive high voltage (typically 2.0 kV). After being collected from the readout plates, the signal is amplified, shaped and digitized, used for trigger decisions and in case the event is accepted at all trigger levels it is baseline subtracted and stored. The full calorimeter has 47,032 readout channels.

The cells are grouped together for signal readout to form pseudo-projective towers as shown in Fig. 3.6. The term “pseudo-projective” was chosen because the centers of cells of increasing shower depth lie on rays from the center of the interaction region (*i.e.* the center of the detector), but the cell boundaries are aligned perpendicular to the absorber plates. Towers in both EM and hadronic modules cover a region of 0.1 in η and 0.1 in ϕ , with the exception of the third layer of the EM modules, located at EM shower maximum, which is segmented twice as finely in both η and ϕ . For all layers with $|\eta| > 3.2$ the cell coverage in both η and ϕ increases to 0.2, to avoid too small cells.

The electromagnetic sections (EM) were designed to sample electron showers. The absorber plates are thin (3 and 4 mm in the CC and EC, respectively) and made of nearly pure depleted uranium. There are four separate depth layers for the EM modules. In the CC, the layers are approximately 1.4, 2.0, 6.8 and $9.8X_0$ thick, while in the EC they are approximately 1.6, 2.6, 7.9 and $9.3X_0$ (where X_0 is the radiation length or the distance in which an electron loses all but $\frac{1}{e}$ of its energy). The values for the first layers include all material in the calorimeters themselves, from the outer warm wall to the first liquid Ar gap. The detector components between the interaction region and the first active gap in the CC at $\eta = 0$ consist of about $4.0X_0$ of material; those between the interaction region and the first active gaps of the ECs at $\eta = 2$ are $4.4X_0$ thick.

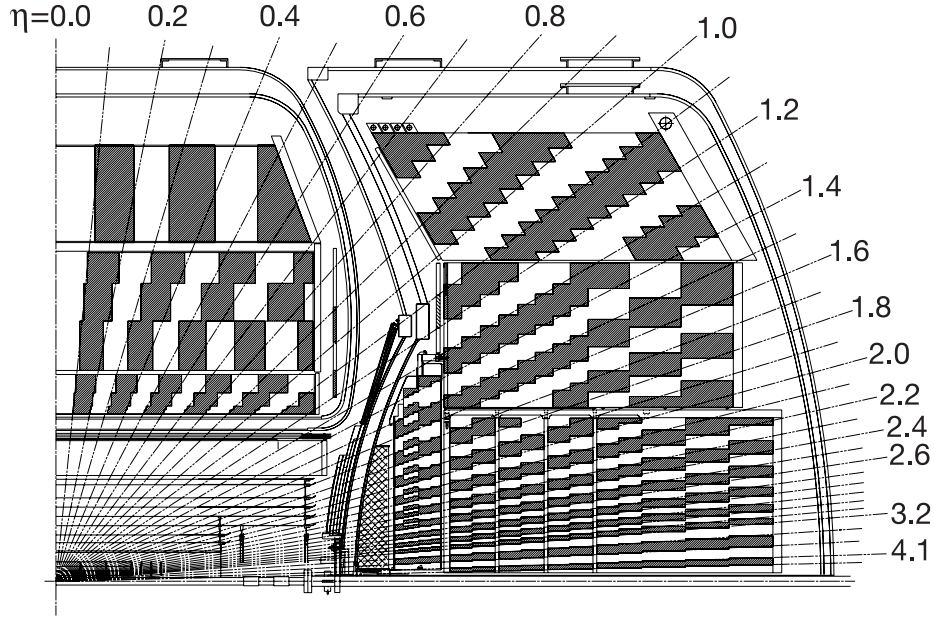


Figure 3.6. Longitudinal section view of one quarter of the $DØ$ calorimeters showing the segmentation pattern. The shading indicates the way cells are grouped to form towers, while the rays indicate pseudorapidity intervals from the center of the detector.

The absorber plates in the fine hadronic modules are made from 6-mm-thick uranium-niobium (2 %) alloy and in the coarse hadronic ones from 46.5 mm thick copper (in the CC) or stainless steel (in the EC). The fine hadronic modules in the CC consist of three layers of cells, approximately 1.3 , 1.0 and $0.76\lambda_I$ (where λ_I is the interaction length or the mean free path of a particle before undergoing an interaction that is neither elastic nor quasi-elastic in a given medium). The single CC coarse hadronic module has a thickness of about $3.2\lambda_I$. The two EC inner hadronic modules are cylindrical, with inner and outer radii of 3.92 and 86.4 cm. The fine hadronic portion consists of four readout cells, each $1.1\lambda_I$ thick. Each of the EC middle hadronic modules has four fine hadronic readout cells of about $0.9\lambda_I$ each and a single coarse hadronic section of $4.4\lambda_I$. The outer hadronic modules of the ECs are made from stainless steel plates inclined at an angle of about 60° with respect to the beam axis. The maximum thickness is $6.0\lambda_I$. Each layer is offset from the others to provide hermeticity.

In the crossover regions between the CC and ECs there are several areas (gaps) where particles travel mostly through support structures and cryostat walls. To address this problem, additional layers of sampling have been added. Single-cell structures called massless gaps were installed within the central and end cryostats. These are standard calorimeter readout cells placed in front of the first layer of uranium. In addition to this, an intercryostat detector (ICD) consisting of a single layer array of 384 scintillating

tiles enclosed in light-tight aluminium boxes was mounted on the surfaces of both end cryostats. The ICD covers the region $1.1 < |\eta| < 1.4$; its position is indicated in Fig. 3.3. The tile size was chosen to match the calorimeter cell size. The scintillation light is taken outside the magnetic field region by optical fibers and amplified using phototubes. The signal electronics are designed to be compatible with the calorimeter digitization system and electronics calibration.

The central and forward preshower detectors (CPS and FPS) are layers of scintillating fibers similar to the ICD. They are placed on the calorimeter cryostat surfaces closest to the interaction region.

3.2.4 Muon system

Muons lose most of their energy in the interaction with matter through ionization. As opposed to the electrons, the bremsstrahlung plays very little role in the energy loss for muons with energies below few hundred GeV, since the effect is attenuated by a factor of about 40,000 (the square of m_μ/m_e). As a result, muons with moderate transverse momentum ($p_T > 2.7$ GeV) completely penetrate the central calorimeter. High energy muons can sometimes be detected in the calorimeter due to their specific minimum ionizing particle (MIP) signature, but because they rarely form an electromagnetic shower their total energy cannot be measured in the calorimeter. A detector specifically designed for muon identification was placed outside the DØ calorimeter system, taking advantage of the muons' penetrating power: anything that reaches that far is most likely a muon.

The muon system is the outermost subsystem of the DØ detector, providing coverage up to $|\eta| \approx 2$. It consists of layers of drift tubes and scintillation counters surrounding the calorimeter, embedded in a magnetic field which bends the trajectories of charged particles in the $r - z$ plane. It is divided into a central module ($|\eta| < 1$) also referred to as the wide angle muon system (WAMUS) and two forward ones ($1 < |\eta| < 2$) known as the forward angle muon system (FAMUS). Figure 3.7 shows a view of the drift chambers, while Fig. 3.8 presents in detail the muon scintillation detectors, from both the central and forward regions.

The central muon system consists of a toroidal magnet, drift chambers, the $A\phi$ scintillation counters and the cosmic cap and bottom scintillation counters.

The central toroid is a square annulus made of iron which is 109 cm thick and covers the region $|\eta| < 1$. The inner surface is situated at a distance of 318 cm from the beamline. The magnet is wound using twenty coils of ten turns each. Two end toroids are squares extending 426 cm from the beamline in both x and y directions, with a 183 cm square hole centered on the beamline and wound around the vertical sides of the hole using eight coils of eight turns each. They are situated at $454 \leq |z| \leq 610$ cm. The central and end toroid coils are operated in series at a current of 1500 A. The value of the magnetic field obtained is about 1.8 – 1.9 T, and the polarity, as in the case of the solenoid, changes regularly.

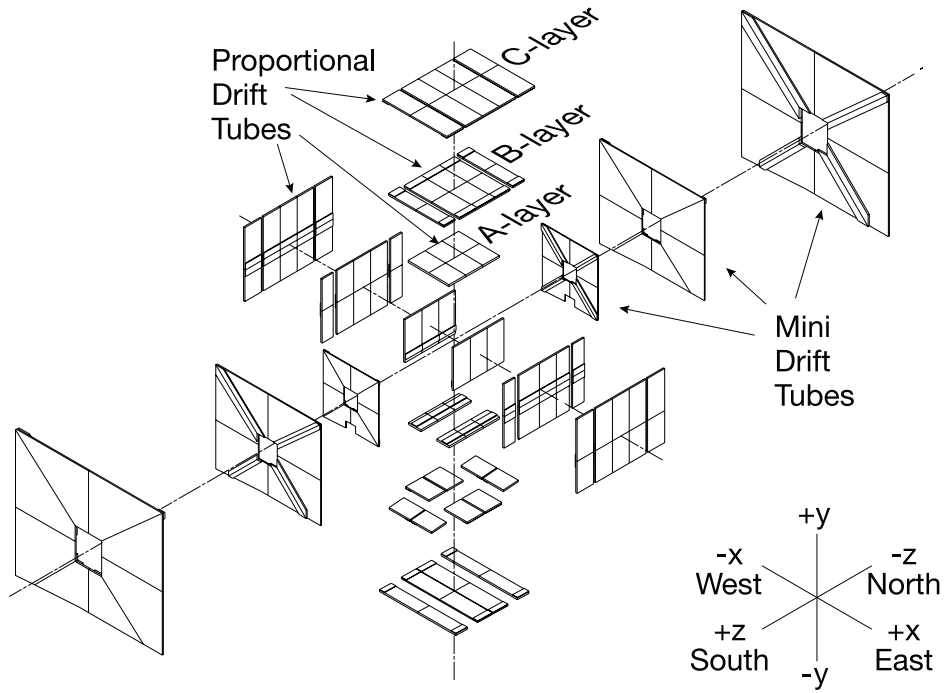


Figure 3.7. Exploded view of the muon drift chambers.

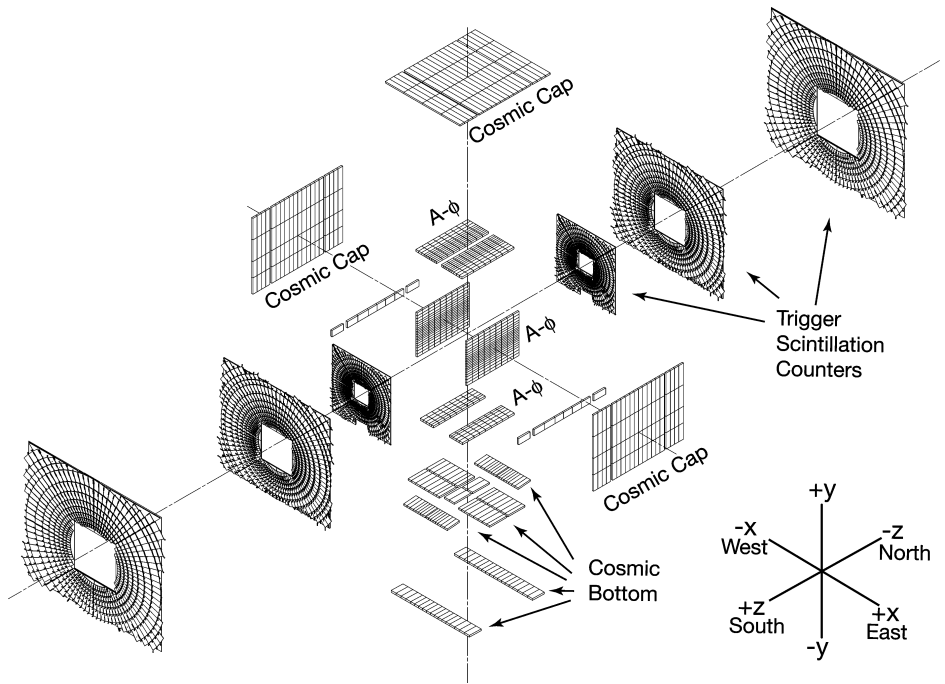


Figure 3.8. Exploded view of the muon scintillation detectors.

Drift tube detectors are gas filled containers with an anode wire strung through the center and cathode pads placed at the top and bottom of the detector. When a charged particle traverses the volume, it ionizes the gas producing electrons and ions. The electrons are accelerated towards the anode, gain energy and produce further ionizations. This results in an “avalanche” of electrons which amplifies the signal. The drift chambers used in the WAMUS region are called Proportional Drift Tubes (PDTs). They are organized in three layers, one of them (the A layer) being located inside the central toroid magnet, and the other two (the B and C layers) situated outside the toroid magnet. The chambers are rectangular, large (typically $2.8 \times 5.6 \text{ m}^2$) and made of extruded aluminium tubes. The PDTs have three decks of drift cells, except for the lateral and upper sides of the A-layer where they have four. Each deck is 24 cells wide. The cells are 10.1 cm wide and 5.5 cm high. Along with an anode wire at the center of each cell, oriented parallel to the magnetic field lines, vernier cathode pads are located above and below the wires to provide information on the hit position along the wire. The vernier pads consist of two metal strips that run along the length of the tube and their width follows a self repeating see-saw pattern with a cycle of 60 cm. The relative amounts of charge deposited on each strip indicate the position of the passing particle. The tubes are filled with a gas mixture of 84 % Ar, 8 % methane and 8 % CF_4 . The operating voltage is 2.3 kV for the pads and 4.7 kV for the wires. The drift velocity is approximately 10 cm/ μs and the maximum drift time is 500 ns. The hit resolution is between 10 and 50 cm, depending on the position along the pad.

The $A\phi$ scintillation counters cover the A layer PDTs and provide fast triggering information, being used as well for muon identification and the rejection of out-of-time backscatter from the forward direction. Their ϕ segmentation is approximately 4.5° , which matches the CFT trigger sectors, and their longitudinal segmentation is about 84.5 cm. Nine counters are required along the z direction, with small separation between them. There are 630 $A\phi$ counters which form a rectangular annulus of $5.67 \times 5.77 \text{ m}^2$ with a gap at the bottom of 2.44 m in length. The gap extends approximately between 4.3 and 5.0 in ϕ and between -1.2 and 1.2 in η , where the calorimeter support is located. The scintillation counters collect scintillation light when a charged particle passes through them. Wavelength shifting fibers are embedded in the scintillators, being connected to photomultiplier tubes which convert the light into electric signal.

The cosmic cap and bottom counters are installed on top, sides and bottom of the C-layer of PDTs, providing fast timing signal to associate a muon in a PDT with the appropriate bunch crossing and discriminate against cosmic ray background. There are 240 counters, 63.5 cm wide and 207 - 287 cm long. As opposed to the $A\phi$ counters, they are positioned with their width along z and length along ϕ . The cosmic bottom counters are very similar to the cosmic cap ones, except that they are positioned with their narrow dimension along ϕ and their long dimension along η , each covering 4.5° in ϕ , similarly to the $A\phi$ counters. There are 132 counters, situated outside the bottom of the B and C layers of PDTs, as well as on the center of the sides of the B layer.

The forward muon system covers the region $1.0 \leq |\eta| \leq 2.0$ and consists of four major parts: the end toroidal magnets (described above), three layers of mini drift tubes (MDTs), three layers of scintillation counters used for triggering on events with muons and the shielding around the beam pipe.

The MDTs were chosen for their short electron drift time (less than 132 ns), good coordinate resolution (less than 1 mm), radiation hardness and low occupancy. There are 6,080 mini drift tubes arranged in three layers A, B and C, with A closest to the interaction region and placed inside the toroidal magnet, while the B and C layers are further away and outside the toroid. Each layer is divided into octants, as illustrated in Fig. 3.7, and consists of three (layers B and C) or four (layer A) planes of tubes mounted along the magnetic field lines. An MDT tube consists of eight cells, each with a $9.4 \times 9.4 \text{ mm}^2$ internal cross section and a $50 \text{ }\mu\text{m}$ W-Au anode wire in the center. The gas mixture used in the MDTs is $\text{CF}_4 - \text{CH}_4$ (90 % - 10 %). The MDTs are operated at a voltage of 3.2 kV. The drift time in the MDTs is 60 ns, less than the beam crossing time, and therefore scintillation counters are not needed to match the drift tube hits to events as in the case of the PDTs. However, scintillation counters in all three layers in the forward region are still useful for reducing backgrounds coming from sources other than the interaction region (cosmic ray muons for example).

The muon forward scintillation counters are mounted inside (layer A) and outside (layers B and C) of the toroidal magnet. Each layer is divided into octants containing about 96 counters. The ϕ segmentation is 4.5° and as in the case of the $A\phi$ counters matches the CFT trigger sectors. There are 4,214 such counters and their timing resolution is about 1 ns.

The beam halo as well as scattered proton and antiproton fragments which interact with the end calorimeter, the beam pipe or the Tevatron low-beta quadrupole magnets contribute to non-muon background in the central and forward muon systems. Shielding consisting of layers of iron, polyethylene and lead in a steel structure surrounding the beam pipe and the low-beta magnets was used to significantly reduce this background. The position of the shielding is shown in Fig. 3.2. It extends from the end calorimeter cryostat, through the end toroid magnet to the wall of the collision hall. Monte Carlo studies show that the shielding provides a factor of 50-100 reduction in energy deposition in the muon detector.

The momentum resolution of the forward muon system is limited by multiple scattering in the toroid and the overall muon momentum resolution is generally defined by the central tracking system for muons with momentum up to 100 GeV. The MDT system, with a coordinate resolution of 0.7 mm per hit, improves the momentum resolution for higher momentum muons and plays a particularly important role in determining the muon momentum for tracks with $1.6 \leq \eta \leq 2.0$, which do not pass through all the layers of the CFT.

3.2.5 Luminosity monitor

The primary purpose of the luminosity monitor (LM) is to determine the Tevatron luminosity at the $D\bar{O}$ interaction region by detecting inelastic $p\bar{p}$ collisions. The LM serves also as an instrument for measuring beam halo rates and for making a fast measurement of the z coordinate of the interaction vertex.

The LM consists of two arrays of 24 plastic scintillation counters with PMT readout located at $|z| = 140$ cm. The counters are 15 cm long and are situated in front of the end calorimeters, covering a pseudorapidity range $2.7 < |\eta| < 4.4$.

The luminosity \mathcal{L} is determined from the average number of inelastic collisions per beam crossing \bar{N}_{LM} measured by the LM:

$$\mathcal{L} = \frac{f \cdot \bar{N}_{LM}}{\sigma_{LM}}, \quad (3.3)$$

where f is the beam crossing frequency and σ_{LM} is the effective cross section for the LM that takes into account the acceptance and efficiency of the LM detector. Since \bar{N}_{LM} is typically greater than one, it is important to account for multiple $p\bar{p}$ collisions in a single beam crossing. This is done by counting the fraction of beam crossings with no collisions and using Poisson statistics to determine \bar{N}_{LM} .

To distinguish between $p\bar{p}$ interactions and beam halo backgrounds, precise time-of-flight measurements of particles traveling at small angles with respect to the beam direction are used. A fast estimation of the z coordinate of the vertex is done using

$$z_v = \frac{c}{2}(t_- - t_+) \quad (3.4)$$

where t_- and t_+ are times-of-flight measured for particles hitting the LM detectors at $z = \pm 140$ cm. Beam collisions are selected by requiring $|z| < 100$ cm, which encompasses nearly all $p\bar{p}$ collisions produced by the Tevatron, since $\sigma_z \approx 25$ cm. Beam halo particles traveling along the z direction will have $z_v \approx 140$ cm and are therefore eliminated by the above requirement.

3.2.6 Trigger and data acquisition systems

As mentioned in Section 3.1, the beams of protons and antiprotons are grouped into bunches with a bunch-to-bunch separation of 396 ns, and the bunches are organized into three trains or superbunches of 12 bunches each, separated by 2.2 μ s. This gives an average $p\bar{p}$ interaction rate of 1.7 MHz. It is technically unfeasible and scientifically uninteresting to write all these events to storage tape for offline analysis. In fact, the rate of events which will be kept for analysis is limited to an average of 30 Hz by the amount of memory necessary for data storage and the computing time required for their reconstruction.

An online filtering system called trigger was designed to select only potentially interesting events. It uses information coming from all detector subsystems described above and only retains for storage events with certain characteristics, which can be specified. The trigger system is shown schematically in Fig. 3.9. It consists of three decision-making subsystems of increasing complexity called Level 1 (L1), Level 2 (L2) and Level 3 (L3) triggers. An event passing one of the requirements set for accepting events at Level 1 will be stored in a buffer awaiting a decision from Level 2, which uses more sophisticated information and in case it passes is then stored again in a different buffer until a decision is made at Level 3. The L1 and L2 buffers play an important role in minimizing the experiment's deadtime.

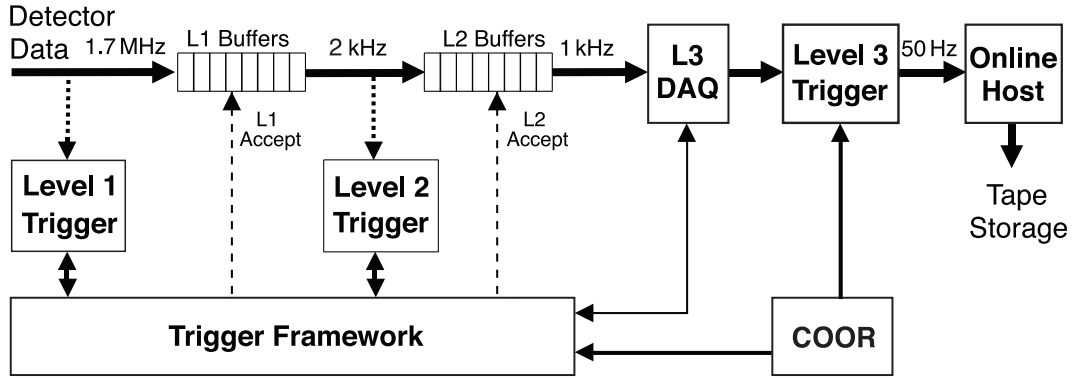


Figure 3.9. The $D\bar{O}$ trigger and data acquisition systems. The specified rates are the ones maximally allowed by design.

The trigger system is closely integrated with the data readout and data acquisition systems, as illustrated in Fig. 3.9. Each event satisfying the L1 and L2 triggers is fully digitized and all the data blocks for the event are transferred to a single commodity processor in the L3 farm. The overall coordination and control of $D\bar{O}$ triggering is handled by the COOR package running on the online host. COOR interacts directly with the trigger framework (TFW, briefly described in the next subsection) for the L1 and L2 triggers and with the data acquisition (DAQ) supervising systems for the L3 triggers. COOR receives requests from users to configure the detector or to start and stop runs and sends the necessary commands to the rest of the system to carry out those requests. The DAQ system is responsible for the data flow of the fully digitized event into L3 and later for the storage on tape of events which pass a L3 trigger.

Level 1 trigger

The first trigger stage (Level 1 or L1) makes use of information coming from all sub-detectors described above, except the SMT, to select interesting events and reduce the rate by a factor of approximately 1000. The Level 1 trigger comprises a collection of hardware trigger elements which report their findings to the Trigger Framework (TFW) upon each beam crossing. The TFW then makes a global decision to either reject the event or accept it for further examination. In addition, the TFW coordinates various vetoes that can inhibit triggers, provides the prescaling of triggers which exhibit unacceptably high rates and correlates the trigger and readout functions. It consists of several large electronics cards housed in customized VME crates and it makes extensive use of field programmable gate array (FPGA) technology to implement different functions, being programmable by COOR via text-based commands.

The time lapse in which a decision has to be made is 396 ns at L1, but can be delayed by 3.5 μ s. The L1 system can support a total of 128 separate trigger requirements called trigger bits. Each trigger bit is programmed to check that a specific combination of

trigger terms (or trigger conditions) were fulfilled, using logic circuits determined by custom hardware and firmware built using a series of FPGAs.

The Level 1 central track trigger (L1CTT) reconstructs trajectories of charged particles using data provided by three scintillator-based detectors: CFT (axial fibers only), CPS and FPS. It uses 80 segments in ϕ of 4.5° each called trigger sectors. Hits in each sector are used to search for tracks via pre-programmed look up tables. This is done by considering approximately 20,000 possible hit patterns consistent with particle tracks. The track predefined patterns, or equations, require a fiber hit in all eight CFT axial layers. The tracks pass the trigger if their transverse momentum is greater than one of the following four thresholds: 1.5, 3, 5 and 10 GeV. The generated L1 track candidates are then passed also to the L1 Muon trigger.

The Level 1 muon trigger (L1MUO) combines information from muon scintillation counters, wire chamber hits and the L1CTT to build muon objects. Field programmable gate arrays are used to perform combinatorial logic on roughly 60,000 muon channels and up to 480 tracks from L1CTT for each bunch crossing. The hit information in the wire chambers are used to form track stubs (or centroids) which are used to confirm the scintillator hits in each layer. Triggers are formed by matching confirmed scintillator hits between layers or with L1 track candidates coming from L1CTT. Timing information from the scintillation counters is also used to reject cosmic rays which are typically not consistent with tracks coming from the center of the detector within a certain time frame around a beam crossing.

The Level 1 calorimeter triggers (L1CAL) add up the energy in trigger towers which cover 0.2×0.2 in $\Delta\eta \times \Delta\phi$ each, for both the electromagnetic (EM) and the hadronic (H) part of the calorimeter separately. There are 1280 EM towers and 1280 H towers. The tower energies are converted to E_T and have pedestals subtracted as well as energy scales adjusted if necessary. Due to signal to noise considerations only trigger towers up to $|\eta| < 3.2$ are considered for triggering. The triggers are formed by requiring that the transverse energy deposited in the trigger towers be above certain levels in one or more towers. Additional trigger terms are constructed from global quantities in the calorimeter, such as total energy, total energy projected in the transverse plane and missing E_T (or energy imbalance in the transverse plane).

Level 2 trigger

The second filtering stage (Level 2 or L2) uses data provided by the Level 1 triggers as well as the SMT. It has an input rate of about 2 kHz and an accept rate of 1 kHz. The Level 2 system includes preprocessors for tracking, calorimeter, preshower and muon subsystems, as well as a global processor for integration of the data (L2Global). The subsystems work in parallel to reconstruct simple trigger objects such as tracks, jets, electrons or muons. The trigger decisions are made by the L2Global processor based on the physics objects reconstructed in the preprocessors and the relationships between them. A decision has to be made within $100 \mu\text{s}$ at Level 2. Data corresponding to the events accepted at L2 is fully read out, digitized and sent to the Level 3 trigger.

Level 3 trigger

The third and final stage of filtering is done using a dedicated computer farm of about 300 PCs which run event filters based on fully programmable algorithms written in C++. The L3 filters are usually simplified versions of different parts of the offline reconstruction code. A Level 3 accept or reject decision has to be made in about 250 ms.

The Level 3 trigger decisions are based on complete physics objects as well as on the relationships between them (such as their acoplanarity, the rapidity or azimuthal angle between objects or their invariant mass). Candidate physics objects or the relations between them are generated by object specific algorithms (filter tools). The tools perform the bulk of the work: unpacking raw data, locating hits, forming clusters, applying calibration and reconstructing electrons, muons, tau candidates, jets, tracks, vertices and \cancel{E}_T . Different algorithm parameters are given as input to the tools via the programmable trigger list. They define the physics objects precisely, specifying for example the cone size for a jet algorithm or the electromagnetic fraction used for electron reconstruction.

Individual calls to the tools are made by filters that define the specific selection criteria employed by a tool or imposed on its results. These criteria include the above mentioned tool parameters, as well as thresholds or other cuts applied by the filter on the result of a tool (for example, the requirement of two jets within a certain η range above a fixed E_T threshold).

The trigger list includes blocks of filter scripts that specify one or more filters and defines the L3 condition for each L3 trigger or filter bit. Each L3 filter script is associated with a L2 bit. Failure to pass an individual filter terminates the execution of the script, calling no further tools. Only when all filters in a script are satisfied, is the trigger satisfied and the event sent to the host cluster to be recorded.

Data storage and access

The typical size of an unreconstructed “raw” event is about 250 kbytes. The total number of events collected by the DØ experiment so far is approximately 40 billion, of which about half are used in the analysis presented here. Due to cost considerations, the medium chosen for storage is magnetic tape. The tapes are placed in special storage rooms and the access to data is assured by robots. The data handling system, called SAM, is organized as a set of servers which work together to store and retrieve files and associated metadata. If all events collected by the DØ experiment would be placed on typical compact disks (CDs) placed directly on top of each other, the stack would be higher than the Eiffel Tower in Paris. To put things in perspective, the final sample selected in this analysis would easily fit on one CD.

4

Object Identification

4.1 Tracks

Trajectories of charged particles resulting from a $p\bar{p}$ collision are reconstructed using the position of the detector elements which they encounter and in which the particles lose energy by interacting with their material. The energy deposits in the SMT and CFT, called “hits”, are used by two distinct pattern recognition algorithms to reconstruct possible track candidates which are then passed to a Kalman track fitter [48–52] to calculate the optimal track parameters.

The first track finding algorithm is a histogramming approach [53] based upon the Hough transform [54], a method originally invented in the 1950’s for bubble chamber experiments. The solenoid magnet produces an approximately uniform magnetic field within the tracking system, parallel to the direction of the beam. The trajectories of particles in a plane perpendicular to the direction of the field are therefore circles, which can be characterized by three parameters (ρ, d_0, ϕ) : the curvature $\rho = qB/p_T$, where q is the charge of the particle, B is the magnetic field and p_T is the transverse momentum of the particle, the impact parameter d_0 representing the distance of closest approach of the track to $(0,0)$ and the direction ϕ of the track at the point of closest approach to $(0,0)$. Since the most interesting tracks have small impact parameters, $d_0 \sim 0$. The parameter space (ρ, ϕ) defined by the intervals $-\rho_0 < \rho < \rho_0$ (with $\rho_0 = qB/p_T^{min}$) and $0 < \phi < 2\pi$ is divided into cells creating a 2D histogram. The Hough transform makes a unique correspondence between each hit in the coordinate space (x, y) and a line in the parameter space (ρ, ϕ) . The lines representing all hits from the same track intersect at one point, which corresponds to the parameters of the trajectory in question. In practice, for each hit the contents of the cells covered by the band to which the hit corresponds are incremented, and the cells with the highest number of entries are the ones which represent the regions where the true parameters of the tracks are located. However, since a peak finding procedure is not feasible due to the high level of background, all cells with at least 4 hits and which do not have all their hits contained in one of the nearby cells are considered track candidates and undergo further filtering, this time also using information regarding their pseudorapidity η and the z position, until the tracks with lowest χ^2 are found.

The second track finding method is an iterative road-following algorithm [55,56]: an initial track hypothesis is constructed from three hits, of which at least one in the SMT, and extrapolated to the next layer of SMT or CFT within an expectation window. Any hit within this window is tried to be associated with the track hypothesis, but only

hits which produce a χ^2 increase of less than a certain limit are retained. In case two or more hits of a given layer are accepted, the corresponding number of new hypotheses are added. Finally, the track hypotheses are filtered and only the ones passing certain quality criteria are kept.

The lists of candidate tracks resulting from the two track-finding approaches described above are then combined and passed to a Kalman track fitter, which propagates the tracks through the DØ tracking system while taking into account the interactions with the magnetic field and the material of the detector. The fitter incrementally adds hits to tracks using the input candidates to define roads. In the end, only the tracks with optimal track parameters are retained.

4.2 Vertices

The vertex reconstruction algorithm consists of three steps [57,58]: track selection, vertex fitting and vertex selection. First, tracks are clustered according to their z coordinate. Only tracks which have at least 2 SMT hits and $p_T > 0.5$ GeV are kept for fitting. Additionally, the significance of the track's distance of closest approach to (0,0) in the (x, y) plane $S = d_0/\sigma_{d_0}$ has to be less than 3. For each z cluster, an iterative vertex search using a Kalman filter yields a vertex position. Each vertex is then assigned a probability that it originated from a minimum-bias interaction based on the transverse momenta of its associated tracks. The vertex with the lowest probability is then selected as a primary hard scatter vertex.

4.3 Muons

Muons are identified based on their signature in the 3 layer muon detector system. With a toroid magnet placed between the first and second layers, the muon system covers more than 90 % of the angular acceptance of the detector (up to pseudo-rapidity $|\eta| = 2$), providing muon identification as well as an independent - although not very accurate - measurement of the muon momentum. A muon identified on the basis of the information provided by the muon system alone is called a “local muon”. A local muon which is matched to a track found in the central tracking system is called a “central track-matched muon”.

Reconstructed muons are classified depending on the number of hits in each layer of the muon system. A muon is called “tight” if it has:

- at least two wire hits and one scintillator hit in the A layer;
- at least three wire hits and one scintillator hit in either of the layers B or C;
- a fit to the muon track in the muon system which converged ($\chi^2_{loc} > 0$).

A muon is called “medium” if it has:

- at least two wire hits and one scintillator hit in the A layer;
- at least two wire hits and one scintillator hit in either of layers B and C.

The muon is also considered to be “medium” if it is situated in the bottom part of the detector and has one scintillator and two wire hits either in the A layer or in the B and C layers, matching a central track.

The muon is called “loose” if:

- it has at least one scintillator hit;
- fulfills any two of the following three requirements:
 - has at least two wire and one scintillator hits in the A layer;
 - has at least two wire hits in layers B or C;
 - has at least one scintillator hit in the B or C layers.

A muon is also called “loose” if it has at least one scintillator and two wire hits either in the A layer or in the B and C layers, matching a central track.

The central track matching the muon is called “loose” if the distance of closest approach with respect to the primary vertex of the event in the (x, y) plane is less than 0.2 cm for the case where the track does not have SMT hits or less than 0.02 cm if the track has at least one SMT hit. The track is called “medium” if it is loose and has $\chi^2/\text{d.o.f.} < 4$. A “tight” track is a medium track with at least one SMT hit.

The muons selected in this analysis were central track-matched loose muons and the quality of the track to which the local muons were matched was medium. Their energy was measured exclusively by the central tracking detectors, since adding the hits in the muon system was proven to degrade the energy resolution of the muons.

More information on muon identification can be found in [59].

4.4 Electrons and photons

The reconstruction of electrons and photons begins with the formation of calorimeter clusters using a simple cone algorithm which starts with seed cells with $E_T > 0.5$ GeV and groups together all cells within a radius $R = 0.2$. The cluster is considered further only if it has a transverse energy $E_T > 1$ GeV, in which case the cells within an extended cone with $R = 0.4$ are also added to the cluster.

Electrons and photons deposit most of their energy in the electromagnetic (EM) section of the calorimeter, while hadrons typically penetrate further, leaving their energy mostly in the hadronic sections. Therefore the fraction of energy deposited in the EM layers (f_{EM}) is one of the main variables used to distinguish the clusters due to electrons or photons from the hadronic activity in the calorimeter.

A cluster is considered to be an electron if:

- at least 90 % of its reconstructed energy is in the electromagnetic part of the calorimeter ($f_{EM} > 0.9$);
- the cluster is isolated: the energy deposited in a hollow cone $0.2 < R < 0.4$ around the cluster represents less than 15 % of the energy deposited inside the $R < 0.2$ cone;
- there is at least one track in a $\Delta\eta \times \Delta\phi$ road of size 0.05×0.05 around the cluster;
- its shower shape is consistent with an electromagnetic shower.

The electron shower shape estimator [60] is built from seven observables: the energy deposits in the first five layers of the calorimeter, the azimuthal extension of the cluster in the finely segmented third layer of the calorimeter, and the logarithm of the cluster's total energy. From these observables a covariance matrix is built, where the matrix elements are computed from reference Monte Carlo samples at different cluster energies and pseudorapidities. The covariance parameter χ_H^2 measures the consistency of a given shower to be an electromagnetic one. This parameter is required to be less than 50 for a cluster to be considered an electron.

The cluster is identified as a photon if it fulfills the first two requirements listed above for electrons, but it can not be matched to any activity in the tracker. The tracker activity can be either a reconstructed track or a density of hits in the SMT and CFT consistent with a charged track.

4.5 Jets

Particle jets are reconstructed from energy depositions in the calorimeter using a seed-based, improved legacy cone algorithm [61] with a cone radius $R = 0.5$.

To reduce the number of jets originating from calorimeter noise, an algorithm called T42 [62,63] is applied before any clustering takes place. All cells with energies less than 4σ above the threshold, or 2σ above the threshold if they were adjacent to a cell with energy higher than 4σ , are rejected by this algorithm, leading to a reduction of 30 to 60 % of all calorimeter cells.

The calorimeter cells above 0.5 GeV which survive the T42 algorithm are then clustered into seeds. The resulting pre-clusters with energies above 1 GeV are fed into an iterative clustering algorithm. If any of the resulting proto-jets share energy, they are either split or merged such that finally each calorimeter “tower” (defined as group of all cells which have the same η and ϕ , covering an area of 0.1×0.1 in the (η, ϕ) space) is assigned to at most one reconstructed jet.

Additional quality criteria are applied to jets to reduce backgrounds originating from noise and other instrumental effects:

- the fraction of energy deposited in the coarse hadronic layers of the calorimeter, which are most susceptible to noise, is required to be less than 0.4;
- the electromagnetic fraction (f_{EM}) is required to be above 0.05 to avoid noise in the hadronic calorimeter and below 0.95 to remove reconstructed electrons or photons;
- to reduce the number of jets produced by hot cells in the calorimeter, the number of calorimeter towers containing 90 % of the jet's energy is required to be at least 2, and the ratio of highest to next-to-highest E_T of the cells has to be less than 10;
- the jet has to be confirmed by the independent calorimeter trigger readout, to reduce the influence of possible noise in the calorimeter readout chain.

The energy of each reconstructed jet is corrected to the particle level by applying jet energy scale (JES) corrections [64]. The corrections are measured separately for data and Monte Carlo making use of momentum conservation in a sample of photon + jet events. Correction factors are obtained as a function of the jet position in the calorimeter and account for imperfect calorimeter response, the energy offset due to the underlying event, multiple interactions, pile-up effects and noise, as well as for the jet energy loss due to showering outside the fixed-size jet cone.

4.6 Missing E_T

The presence of neutrinos in each event is noticeable due to the imbalance of the energy in the plane transverse to the beam direction. The raw missing transverse energy is defined as the vector equal in length and opposite in direction to the vectorial sum of transverse energies of the calorimeter cells selected by the T42 algorithm. The transverse momenta of all muons are subtracted from this vector, after corrections for the energy deposited by the muons in the calorimeter have been applied. Further corrections related to the jet energy scale (JES) are applied to all good jets in the event and propagated to the missing E_T calculation. However, this implies that all tau leptons which fake a good jet will have JES corrections applied to them, which is not optimal for correcting their energy. One of the reasons is that tau leptons generally form narrow jets, and the corrections for out of cone energy could lead to overestimating their energy and this way degrading the missing E_T resolution. A way to overcome this is described at the end of next chapter, after the energy corrections derived for tau leptons will be presented.

5

Tau leptons

5.1 Tau lepton identification

Tau leptons are elusive particles: with a mass of 1.78 GeV and a short lifetime $c\tau$ of 87 μm , no detector in current or near future high energy collider experiments is ever close enough to detect them before they decay (Table 5.1 shows the decay modes of the tau leptons). Besides, about half of their energy is carried away invisibly by the tau neutrino, making their detection even more difficult.

Final State	Branching ratio (%)	Decay type
$e\nu_e\nu_\tau$	17.8	Leptonic
$\mu\nu_\mu\nu_\tau$	17.4	
$\pi/K\nu_\tau$	11.8	π -like
$\pi/K \geq 1\pi^0\nu_\tau$	36.9	ρ -like
$\pi\pi\pi \geq 0\pi^0\nu_\tau$	13.9	3-prong

Table 5.1. *Tau lepton decay modes*

Within the DØ experiment a tau candidate is a collection of the following objects:

- **Calorimeter Cluster:** reconstructed using the simple cone algorithm [61] with a cone $R < 0.5$, where $R = \sqrt{(\Delta\phi)^2 + (\Delta\eta)^2}$, $\Delta\phi$ is the difference in azimuthal angle and $\Delta\eta$ the difference in pseudorapidity between the axis of symmetry of the cone and each of the calorimeter towers. A core cone of size $R_{core} = 0.3$ is used for the calculation of isolation variables. The cluster should have $rms < 0.25$, with $rms = \sqrt{\sum_{i=1}^n [(\Delta\phi_i)^2 + (\Delta\eta_i)^2] E_{T_i}/E_T}$, where i is the index of the calorimeter tower associated with the τ -cluster, while E_T and E_{T_i} are the transverse energies of the calorimeter cluster and the calorimeter tower i , respectively;
- **Associated Tracks:** all tracks in a $R < 0.3$ cone around the calorimeter cluster, compatible with a τ decay (invariant mass < 1.8 GeV). At least one track with $p_T > 1.5$ GeV is required;
- **Electromagnetic (EM) sub-clusters:** reconstructed with the nearest neighbor algorithm [65] using a seed situated in the third layer of the electromagnetic calorimeter (EM₃), where the showers are supposed to reach their maximum. The EM sub-cluster must have an energy $E > 800$ MeV.

The tau candidates always have a calorimeter cluster. They are classified into three types, depending on the characteristics they possess:

- **type 1:** only one associated track and no EM sub-clusters (roughly corresponding to π -like decays);
- **type 2:** only one associated track and at least one EM sub-cluster (roughly corresponding to ρ -like decays, as well as to decays into an electron and neutrinos);
- **type 3:** at least two associated tracks (roughly corresponding to 3-prong decays).

Due to the high background from jets (see Table 5.2), additional selection criteria have to be applied to distinguish between jets and tau leptons. Three separate neural networks (NN), one for each tau type, were trained using taus from Monte Carlo events as signal and jets back-to-back to non-isolated muons from data as background. The NNs used a simple back propagation algorithm, with one node for each input variable, one intermediate layer having a number of hidden nodes equal to the number of input nodes, and a single output node.

The input variables can be classified as follows:

- **isolation variables :**

- $\text{caliso} = (E_T^\tau - E_T^{\text{core}}) / E_T^{\text{core}},$
- $\text{em12isof} = (E^{EM_1} + E^{EM_2}) / E^\tau,$
- $\text{trkiso} = \sum p_T^{\text{trk}} / \sum p_T^{\tau_{\text{trk}}};$

- **shower shape variables :**

- rms,
- fraction of E deposited in the EM and fine hadronic layers,
- $\text{profile} = E_T^{\text{leading } 2 \text{ towers}} / E_T^\tau,$
- $\text{prf3} = E_T^{\text{leading EM sub-cluster}} / E_T^{EM_3};$

- **calorimeter - track correlation variables :**

- $E_T^\tau / (E_T^\tau + \sum p_T^{\tau_{\text{trk}}}),$
- $\delta\alpha = \text{angle between } \sum \vec{\tau_{\text{trk}}} \text{ and } \sum \vec{EM} \text{ sub-clusters},$

where τ_{trk} (trk) are tracks associated (unassociated) with the tau candidate within a cone $R < 0.5$ and E^{EM_i} is the energy in the i^{th} layer of the EM calorimeter.

Figure 5.1 shows the distribution of some of these input variables for type 1 tau candidates, with an arbitrary normalization. No single distribution can be used to clearly distinguish between signal and background, but when combined in a neural network they can be very effective in making this separation.

The output of a neural network should be close to 0 for the background and near 1 for the signal. Figure 5.2 shows the NN output for background jets and for tau leptons

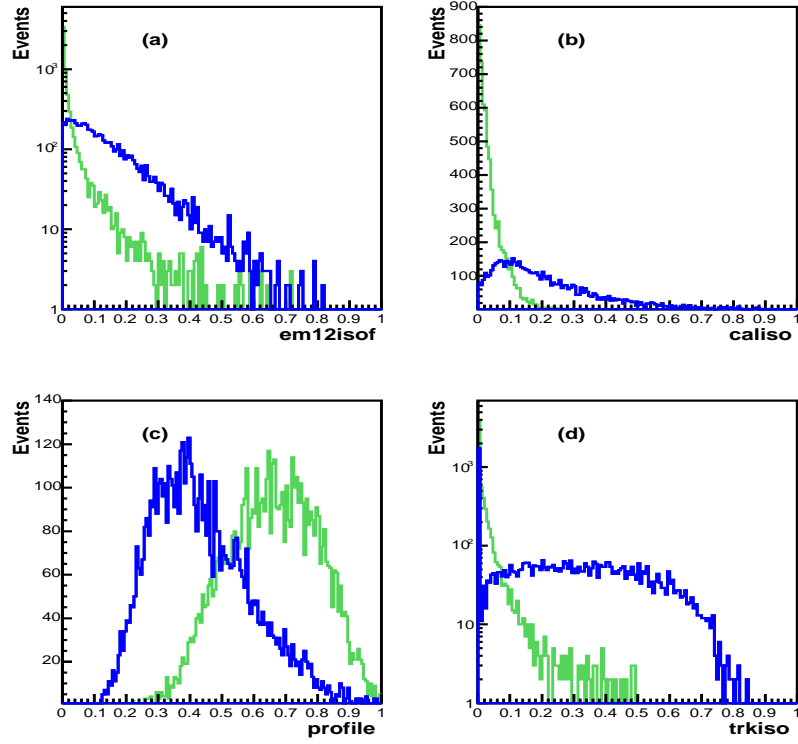


Figure 5.1. Some distributions of NN input variables for type 1 tau candidates: *em12isof* (a), *caliso* (b), *profile* (c) and *trkiso* (d). The signal distributions are shown in (light) green, while the background ones are shown in (dark) blue.

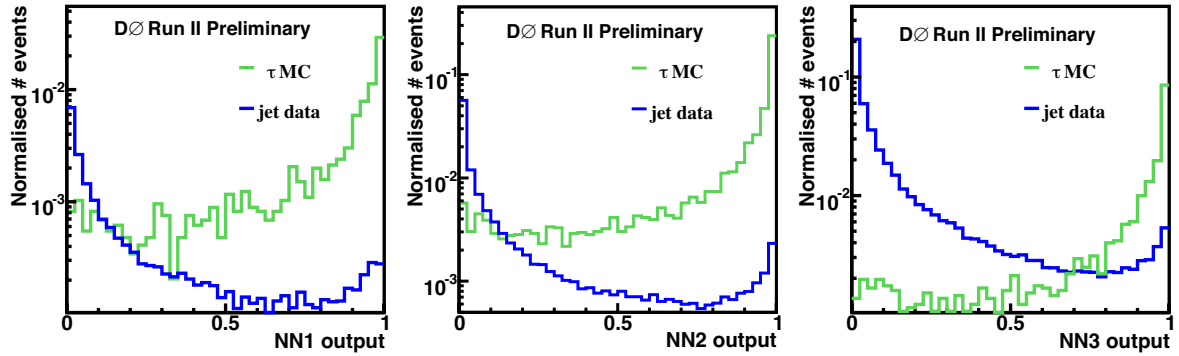


Figure 5.2. NN output distributions for type 1 (left), type 2 (middle) and type 3 (right) tau candidates. The ratio of signal to background is arbitrary, but the relative amounts of type 1, type 2 and type 3 events in background and signal are not. The distributions are normalized with respect to each other such that the sum over the three types is 1 for both signal and background.

from $Z \rightarrow \tau^+\tau^-$ Monte Carlo events for the three tau types. The distributions are normalized with respect to each other such that the sum over the three types is 1 for both signal and background. As shown in Table 5.2, requiring that the NN output is larger than 0.9 results for the sum of all three types in a background rejection close to a factor of 50. The numbers in this table correspond to the tau candidates with transverse energy between 20 and 40 GeV. This shows that using the neural networks to discriminate between QCD jets and hadronic decays of the tau lepton reduces the probability for a jet to be misidentified as a tau lepton to 1.1 % for the sum of all types (from 52 % without the NN output requirement) while maintaining a total efficiency of close to 70 % for real tau leptons which decay hadronically or to an electron and neutrinos. More details on tau identification can be found in [66] and [67].

τ -type	1	2	3	all
QCD jets	2	12	38	52
τ	11	60	24	95
$NN > 0.9$				
QCD jets	0.06	0.24	0.80	1.1
τ	7	44	16	67

Table 5.2. *Efficiencies (%) for tau identification, before and after the $NN > 0.9$ cut. The numbers for signal are with respect to the total number of tau leptons, excepting the $\tau \rightarrow \mu\nu_\mu\nu_\tau$ decays.*

5.2 Tau candidate energy correction

The tau energy scale and resolution are important ingredients in measurements which rely on precise knowledge of the energy of the tau. One of these measurements is the search for the Higgs boson in the di-tau channel, where limits are set based on the mass distribution of the tau lepton pair. However, all analyses involving tau leptons in the final state can benefit from a corrected tau energy, especially when cuts on the tau candidate p_T are used.

The DØ calorimeter is a sampling calorimeter containing liquid Ar and absorber plates of different materials (U, U-Nb, Cu or stainless steel). It was designed in Run I as a compensating calorimeter (see Fig. 38 and Fig. 45 of [68]). However, recent studies show (see [69]) that the charged pion response is now significantly lower than the electron response. A low charged pion response (in the 50 – 70 % range) for pions with energies up to 50 GeV was observed in all η regions of the calorimeter. This is possibly due to the application of a higher zero suppression threshold together with the shortening of the readout time from 2.2 μs to 260 ns in Run II.

As virtually all hadronic decays of the tau lepton contain at least one charged pion or kaon, the response of the calorimeter to these particles will greatly influence the response to tau leptons. A low charged pion response will lead to a poor energy

resolution in the tau energy range below 50 GeV. Since the tracking resolution at low energies was found to be greatly superior to the resolution of the energy measured by the calorimeter when it comes to pions [71], in this analysis the $p_{(T)}$ of the charged track produced by the π^\pm is used as a better measurement of the (transverse) energy of the charged pion. The energy of the neutral pions will continue to be measured using the calorimeter, taking advantage of the fact that they decay electromagnetically and the resolution of the energy measured in the EM region of the calorimeter is even better than the one of the tracking system starting from rather low energies (10 GeV).

As described in detail in the next sub-sections, for the type 1 tau candidates the $p_{(T)}$ of the track was used as the best estimate of the (transverse) energy of the tau lepton, in the energy region where the tracking resolution is superior to the calorimeter energy resolution (up to calorimeter cluster energies of 70 GeV). The method which proved to be most successful for the type 2 and 3 tau candidates was the one in which the (transverse) energy was estimated using:

$$E_{(T)}^{corr} = \sum p_{(T)}^{\tau \text{ trk}} + E_{(T)}^{cal} - \sum R(p_{(T)}^{\tau \text{ trk}}, \eta) \cdot p_{(T)}^{\tau \text{ trk}}, \quad (5.1)$$

where $p_{(T)}^{\tau \text{ trk}}$ is the $p_{(T)}$ of tracks associated to the tau candidate, $E_{(T)}^{cal}$ is the (transverse) energy of the calorimeter cluster and $R(p_{(T)}^{\tau \text{ trk}}, \eta)$ is a number typically between 0.5 and 0.9 representing the response of the calorimeter to π^\pm as a function of the energy and rapidity of the π^\pm (see [69]). $R(p_{(T)}^{\tau \text{ trk}}, \eta)$ is defined as the ratio of the energy of the calorimeter cluster formed by a charged pion and the true energy of that pion. It was measured in MC for different energies between 0 and 50 GeV and the results were fitted with a function of the following form:

$$R(p_{(T)}^{\tau \text{ trk}}, \eta) = p_0(\eta) + p_1(\eta) \cdot \tanh [p_{(T)}^{\tau \text{ trk}}/p_2(\eta)] + p_3(\eta) \cdot p_{(T)}^{\tau \text{ trk}}, \quad (5.2)$$

where $p_{(T)}^{\tau \text{ trk}}$ is the (transverse) momentum of the charged pion track in GeV [72]. The fit parameters for each η region are listed in Table 5.3.

	$0. < \eta < 0.5$	$0.5 < \eta < 1.$	$1. < \eta < 1.5$	$1.5 < \eta < 2.5$
p_0	0.176192	0.397057	0.392424	0.335192
p_1	0.472680	0.255986	0.243833	0.255563
p_2 [GeV]	2.363530	2.911430	4.975300	3.391480
p_3 [GeV ⁻¹]	0.00258638	0.00214346	0.00324337	0.00181515

Table 5.3. *Fit parameters for the charged pion response in Monte Carlo using the default code in GEANT, called GEISHA [70], for the simulation of hadronic interactions.*

As the resolution of the calorimeter becomes better than the tracking resolution for calorimeter cluster energies higher than 100 GeV (type 2) or 120 GeV (type 3), the energy of the calorimeter cluster was used in that energy region, multiplied with an η and E dependent scale factor obtained from MC.

Significant improvements in the energy measurement resolution for all tau-types were observed after the energy correction was applied [71]. Figure 5.3 shows the distributions of measured uncorrected p_x , p_y and p_z and E of tau candidates as a function of the true visible p_x , p_y and p_z and E of the tau leptons from $Z \rightarrow \tau^+\tau^-$ MC to which the tau candidates were matched, while Fig. 5.4 shows the same distributions after the corrections were applied to the tau candidates. The true or generated visible energy is defined as the sum of the energies of the tau lepton decay products which are likely to interact with the DØ detector (all decay products except the neutrinos) at generator level.

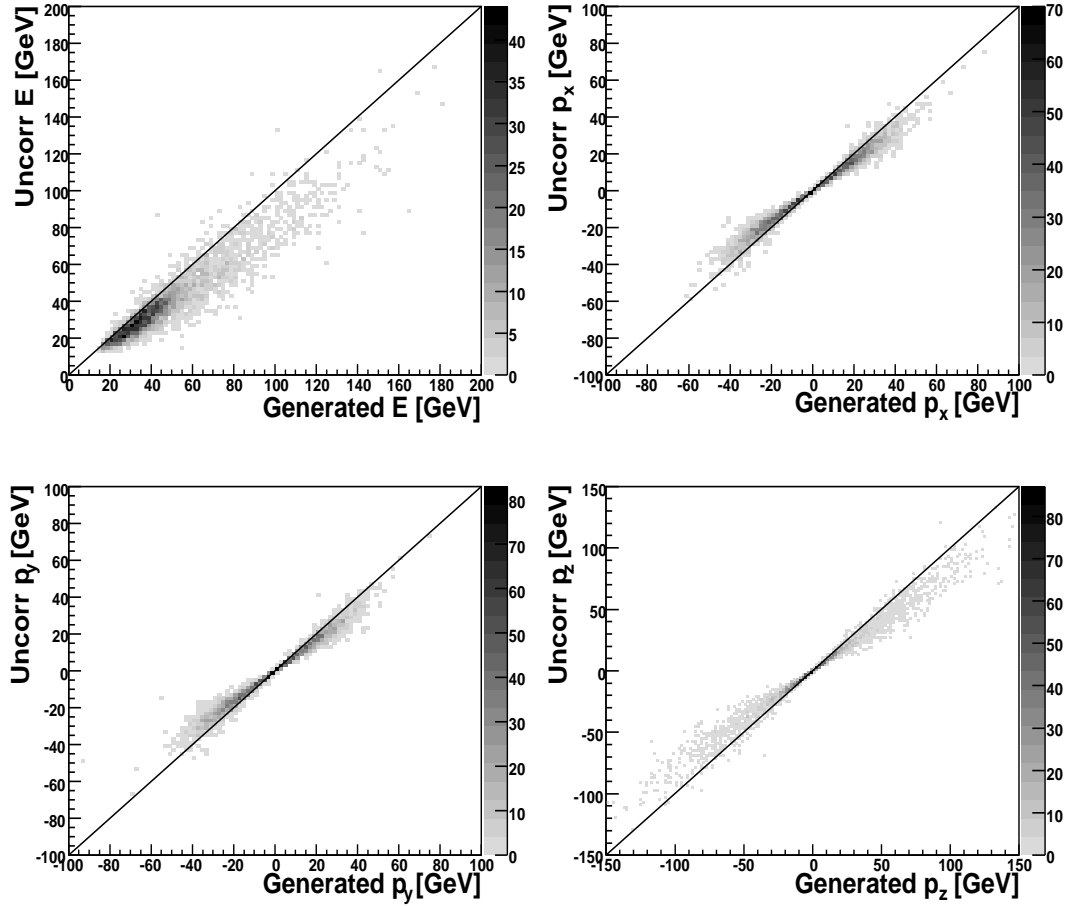


Figure 5.3. Uncorrected E (upper left), p_x (upper right), p_y (lower left) and p_z (lower right) of tau candidates as a function of respectively the generated visible E , p_x , p_y and p_z of tau leptons matching them from $Z \rightarrow \tau^+\tau^-$ MC events.

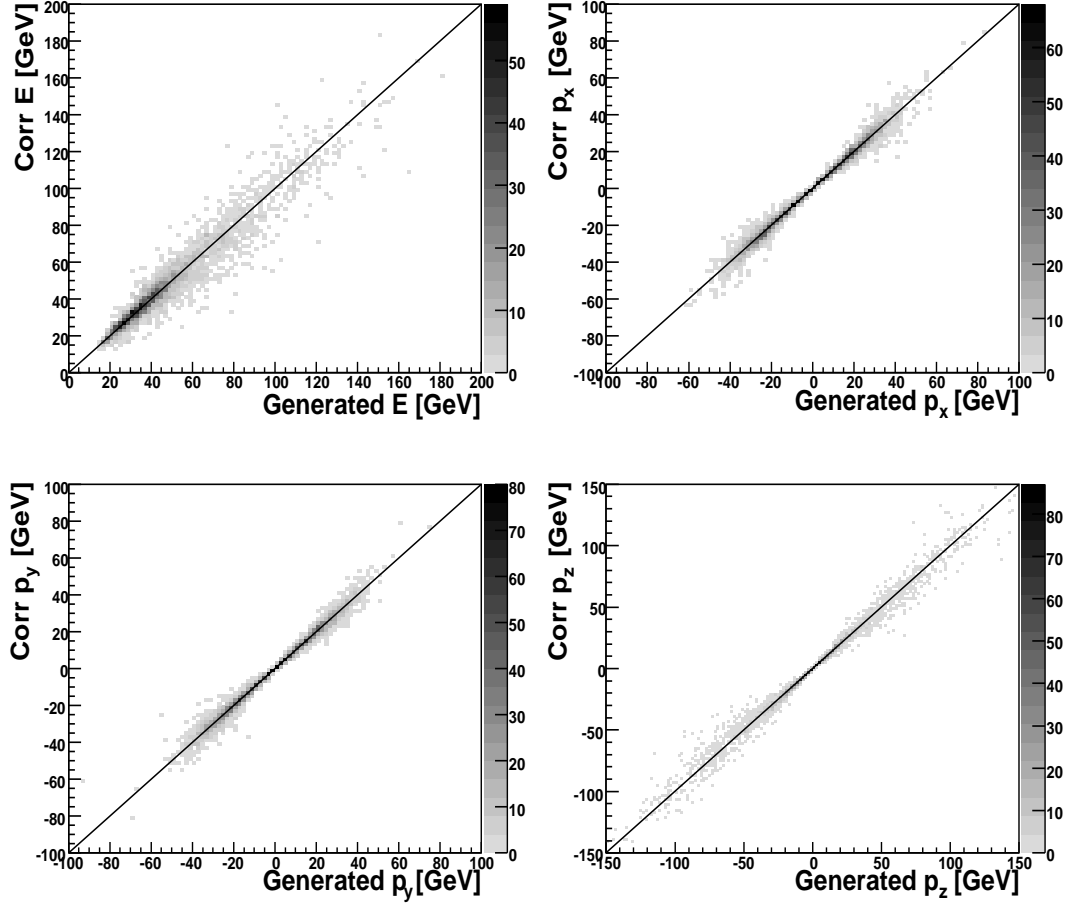


Figure 5.4. Corrected E (upper left), p_x (upper right), p_y (lower left) and p_z (lower right) of tau candidates as a function of respectively the generated visible E , p_x , p_y and p_z of tau leptons matching them from $Z \rightarrow \tau^+ \tau^-$ MC events.

5.2.1 General method

A number of methods for measuring and correcting the energy of tau candidates were studied. For this purpose a Monte Carlo sample was used consisting of 67500 single tau lepton events with minimum bias overlaid from data, generated with p_T between 5 and 300 GeV, uniformly distributed in pseudo rapidity between $[-3., 3.]$. Half of this sample was generated with energies below 30 GeV. For all the details on the generation of this sample please see [73].

The tau candidates found by the reconstruction code, which had a NN output of at least 0.8, were matched to a generated tau lepton which was not decaying into a muon, within a distance $\Delta R < 0.2$.

The resolution corresponding to different methods of measuring the tau candidate energy was defined as the RMS of the following variable, which is calculated for each tau candidate:

$$\text{FED} = \text{Fractional Energy Difference} = \frac{E_{(T)}^{\text{measured}} - E_{(T)}^{\text{true}}}{E_{(T)}^{\text{true}}}, \quad (5.3)$$

where $E_{(T)}^{\text{measured}}$ is the measured (transverse) energy of the tau candidate (either by the tracking system, or the calorimeter, or a combination of both), and $E_{(T)}^{\text{true}}$ is the true (transverse) energy, from MC truth information, of the visible decay products of the tau lepton.

The mean value of this distribution is important as well. In the ideal case it is zero. The preferred energy measurement was therefore the one in which the mean of the FED distribution was closest to zero and the RMS as low as possible in all energy ranges.

5.2.2 Energy correction for type 1 tau candidates

Four methods of measuring and correcting the energy were studied for type 1 tau candidates. The first one is to simply use the energy of the calorimeter cluster, which was the method used by all analyses involving tau candidates in the DØ experiment at the beginning of these studies. The second one is to use the momentum of the track associated with the tau candidate, while placing minimal requirements of compatibility between the momentum of the track and the energy of the calorimeter cluster given by the following inequalities:

$$\frac{p^{\tau \text{ trk}}}{E^{\text{cal}}} > 0.7 \quad , \quad \frac{E^{\text{cal}}}{p^{\tau \text{ trk}}} > 0.3. \quad (5.4)$$

The third method was to apply the charged pion corrections on all tau candidates, as given by Eq. 5.1. Finally, the fourth method, called the “optimized” method, is a combination between the use of the associated track momentum in the low energy regime (up to a calorimeter cluster energy of 70 GeV), where the tracking resolution is superior to the calorimeter energy resolution, and the use of calorimeter cluster energy multiplied with a scale factor meant to bring the FED mean to zero for energies higher than 70 GeV. For the low energy region, the condition of compatibility between the energy of the calorimeter cluster and the momentum of the track given by the inequalities 5.4 was required. The tau candidates which failed this condition were neglected in this study. However, in MC only 1.6 % of type 1 tau candidates with an associated track of good quality (which has at least one SMT hit) do not fulfill conditions 5.4.

The calorimetric response of tau candidates and their energy resolution were found to have a strong dependence on pseudo-rapidity. Figure 5.5 illustrates this dependence by showing the distribution of FED versus η for all type 1 tau candidates, before and after the corrections given by the optimized method were applied. Therefore the scale

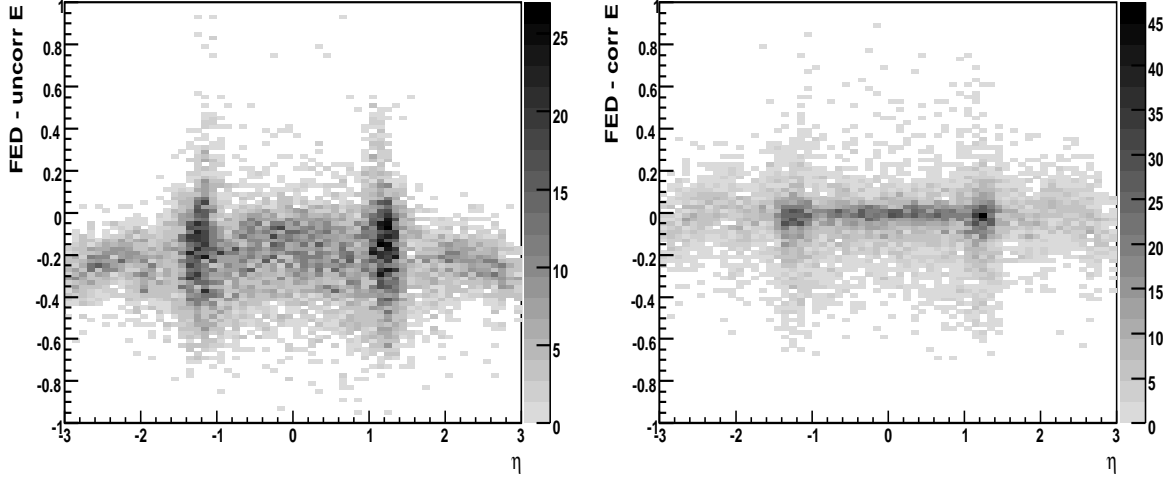


Figure 5.5. *FED distribution as a function of η for type 1 tau candidates, where the measured E of the tau candidate is given by the energy of the calorimeter cluster (left) or by the corrected energy using the optimized method (right).*

factors were measured from MC as a function of η and calorimeter cluster energy and are shown in Fig. 5.6. They were obtained for five η regions ($0. < |\eta| < 0.5$, $0.5 < |\eta| < 0.9$, $0.9 < |\eta| < 1.4$, $1.4 < |\eta| < 2$. and $2. < |\eta| < 3$.) by requiring the mean of the FED distribution to be zero in each energy bin. The results were fitted using 3rd or 4th degree polynomial functions. The fits and the parameters obtained by fitting the scale factors for each energy bin are also shown in Fig. 5.6. For the actual corrections the parametrized functions were used.

It was found that for the region $2. < |\eta| < 3$. the energy resolution of the calorimeter is superior to the tracking resolution for all energies. Therefore the optimal energy measurement in that region is the calorimeter cluster energy multiplied with a correction factor which was found to be constant as a function of tau candidate energy and equal to 1.3 [71].

The FED distributions as a function of generated visible tau lepton energy for the four methods described above can be seen in Fig. 5.7. Figure 5.8 shows the resolution and the mean of the FED variable corresponding to each of the four energy measurements as a function of the true visible energy of the tau lepton. It is worth noticing that after applying the optimized energy correction method the mean of the FED function is now very close to zero over the entire energy range. The resolution of tau lepton energy is highest as well for any visible energy when this method is applied. The effect of these corrections on the energy spectrum of the type 1 tau candidates can be seen in Fig. 5.9.

Finally, Fig. 5.10 shows the FED distributions using the four correction methods mentioned in this section. Significant improvements in the width and the shift of the distribution can be observed after the corrections were applied.

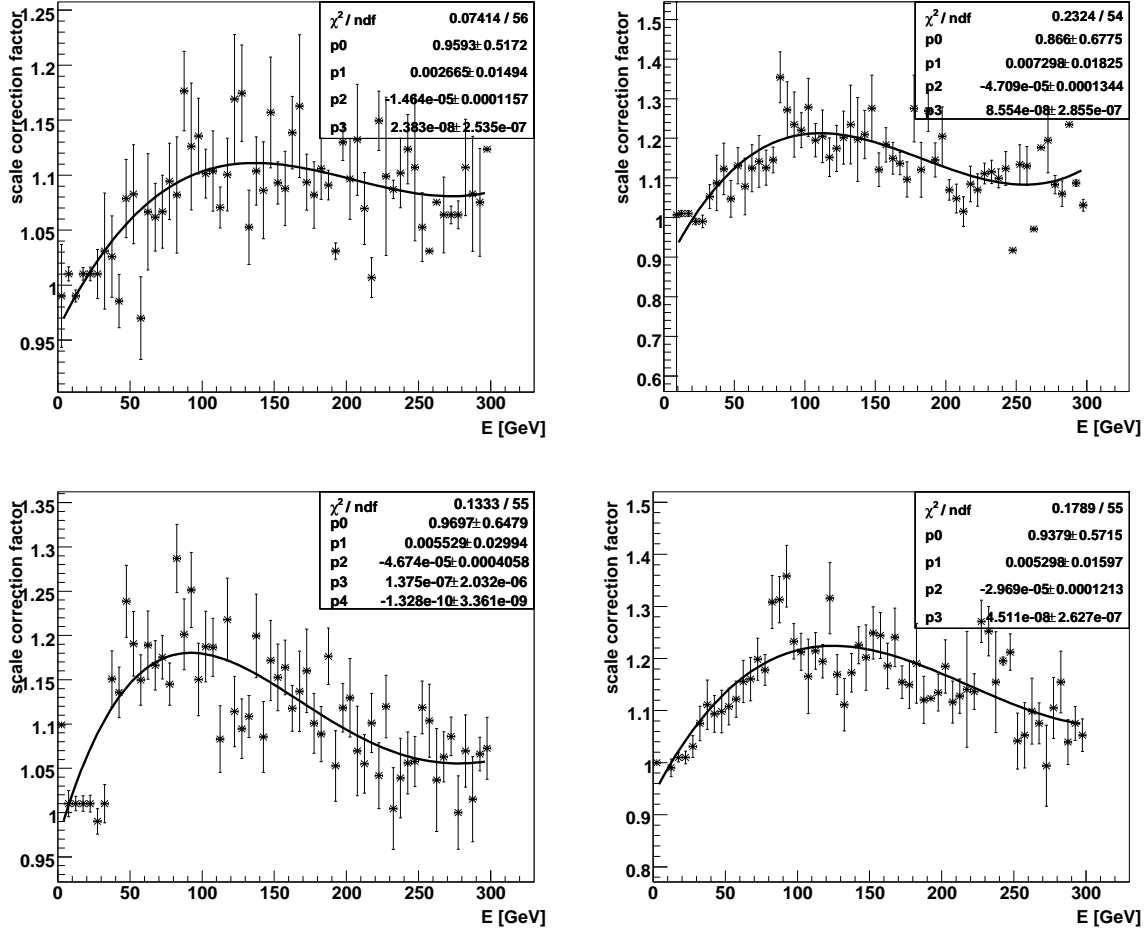


Figure 5.6. Tau energy scale factors for type 1 tau candidates in the η regions $0 < |\eta| < 0.5$ (upper left), $0.5 < |\eta| < 0.9$ (upper right), $0.9 < |\eta| < 1.4$ (lower left) and $1.4 < |\eta| < 2$ (lower right). On the horizontal axis, E denotes the momentum of the associated track for tau candidates having tracks with momentum $p^{\tau \text{ trk}} < 80$ GeV, and the calorimeter cluster energy for the rest of the tau candidates.

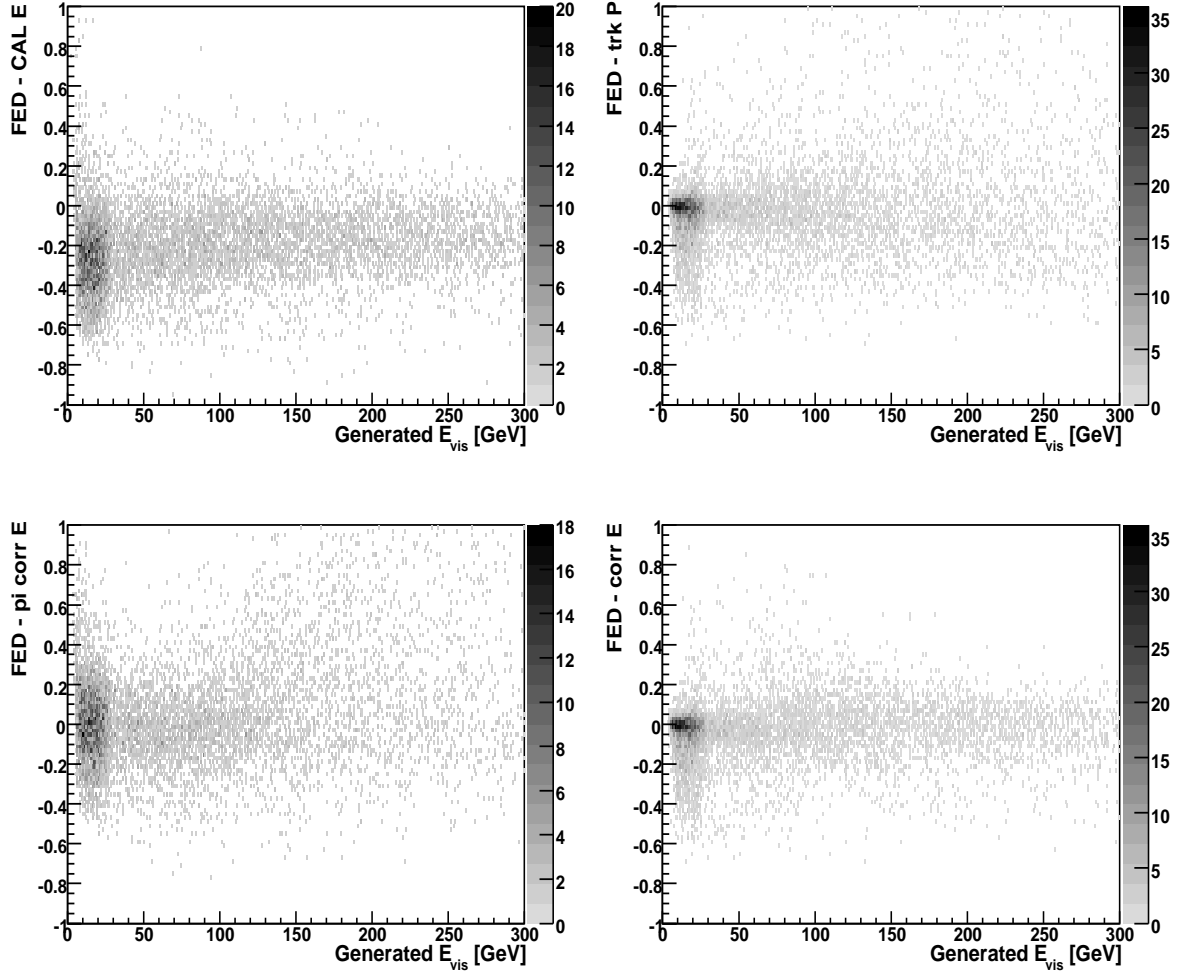


Figure 5.7. *FED* distribution for type 1 tau candidates as a function of the true (generated) visible energy of the tau lepton, for the measured energy in the *FED* function being the energy of the calorimeter cluster (upper left), the momentum of the associated track, with the compatibility condition 5.4 applied (upper right), the energy of the tau corrected using the charged pion response (lower left) and the energy of the tau corrected with the optimized method (lower right).

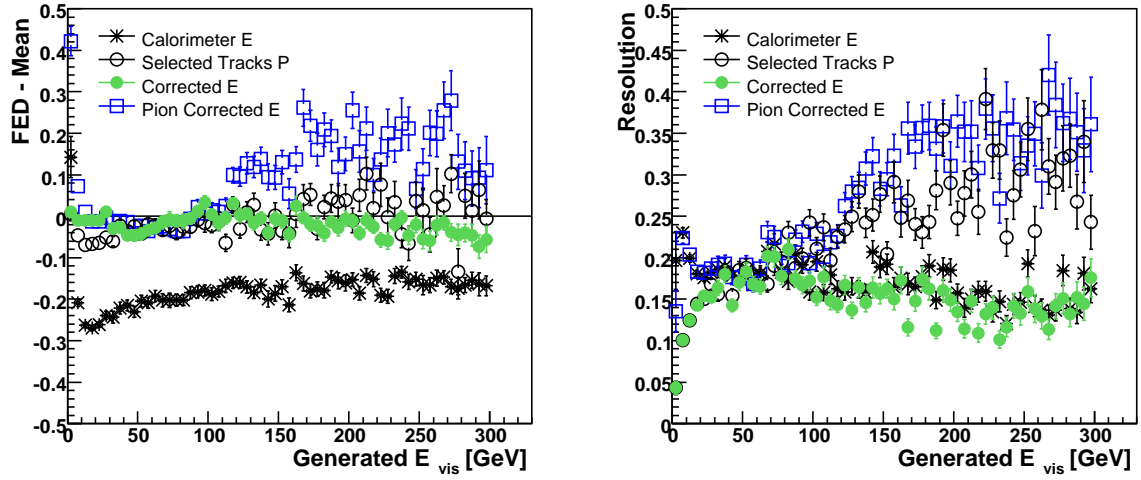


Figure 5.8. The FED mean (left) and FED RMS, or the resolution (right) for type 1 tau candidates as a function of the true (generated) visible energy of the tau lepton, for the measured energy in the FED function being the energy of the calorimeter cluster (asterisks), the momentum of the associated track, with the compatibility condition 5.4 applied (empty circles), the energy corrected using the charged pion response (empty squares) and the energy corrected with the optimized method (filled circles).

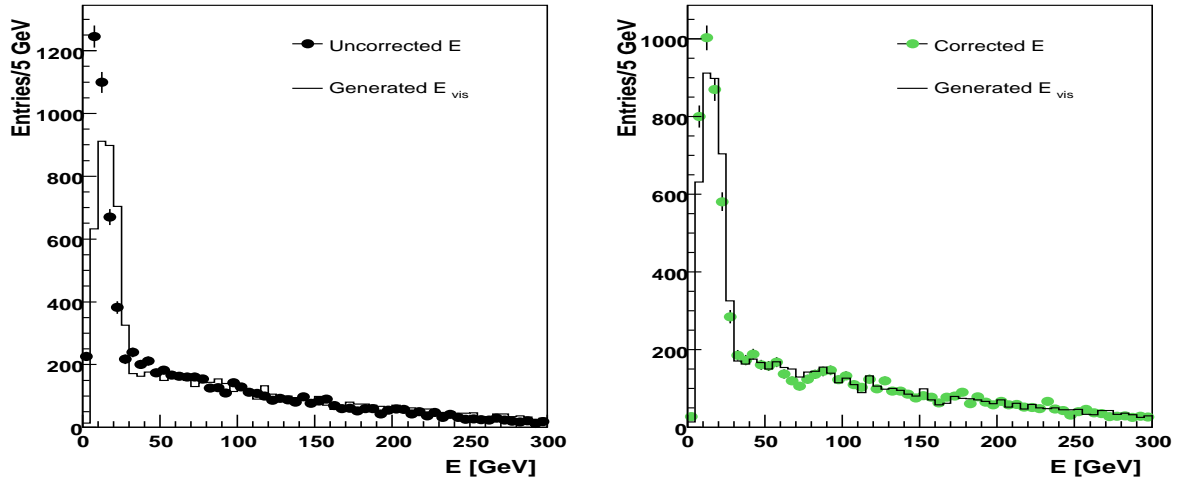


Figure 5.9. Energy spectra for type 1 tau candidates before (left) and after (right) applying the energy corrections. The dots represent the spectrum obtained using the calorimeter cluster E (left) and the energy of the tau candidates corrected with the optimized method (right). For comparison, on both figures the generated visible energy spectrum is also shown (black line).

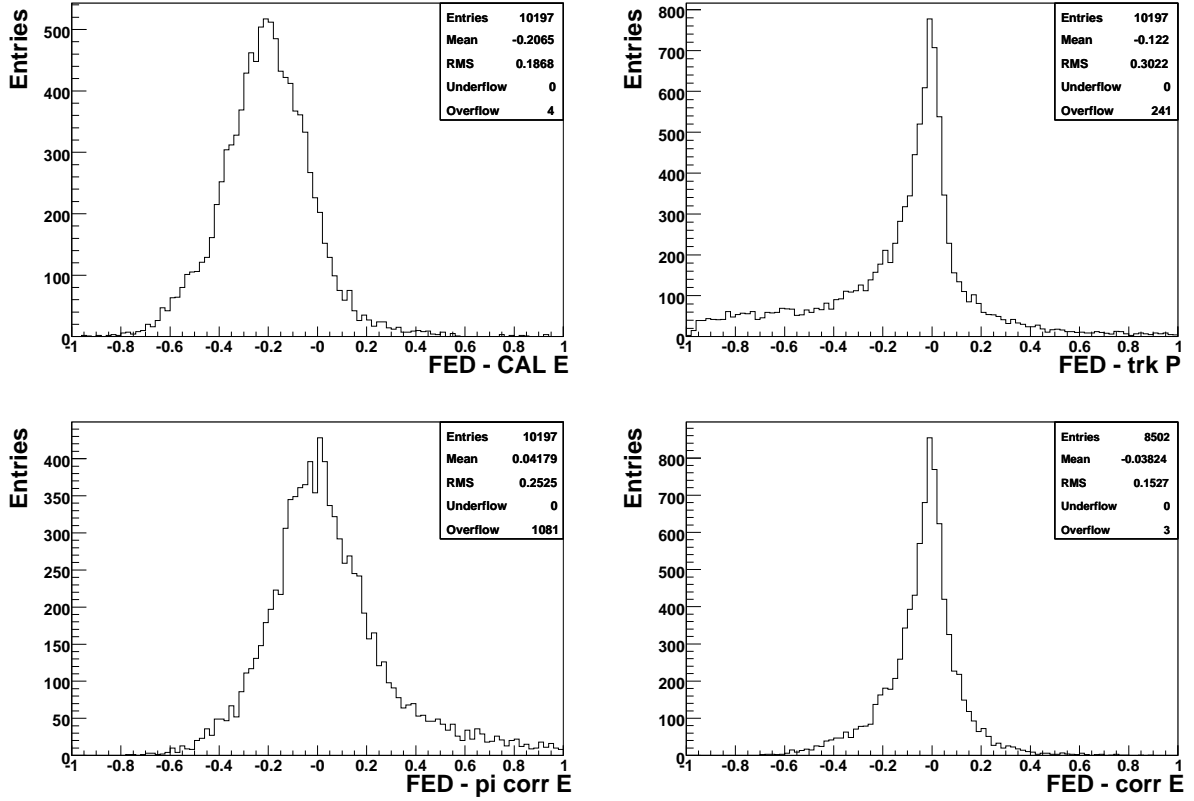


Figure 5.10. *FED* distributions for type 1 tau candidates after using the four methods mentioned above: when the measured energy is the energy of the calorimeter cluster (upper, left), the momentum of the track associated with the tau candidate (upper, right), after applying charged pion corrections on all tau candidates (lower, left) and after applying the optimized method of energy correction (lower, right). These distributions correspond to the $0 < |\eta| < 2$ region.

5.2.3 Energy correction for type 2 tau candidates

Since the calorimeter resolution becomes better than the tracking resolution at high energies (see Fig. 5.8), the optimized method for correcting the energy of a type 2 tau candidate with $E_T^{EM}/E_T < 0.9$ consists of using the pion response corrected energy given by Eq. 5.1 if its calorimeter cluster energy is lower than 100 GeV or the energy of the calorimeter cluster multiplied with a scale factor if the calorimeter cluster energy is higher than 100 GeV.

In this analysis no effort was made to reject the electrons at generator level. However, the electrons will have a very high fraction of energy deposited in the EM layers of the calorimeter. The energy resolution of the EM region of the calorimeter is comparable or better than the tracking resolution at energies above 10 GeV, therefore we use

as the best estimate of the energy of the tau candidate the energy of the calorimeter cluster multiplied with a scale factor for the type 2 tau candidates (mostly electrons) which have more than 90 % of their transverse energy deposited in the EM layers.

Just as in the case of type 1 tau candidates, the corrections applied to the calorimeter cluster energy are dependent on η . Figure 5.11 illustrates this dependence by showing the distribution of FED versus η , before and after the corrections given by the optimized method were applied. Five slightly different η regions were used: $0. < |\eta| < 0.5$, $0.5 < |\eta| < 1.$, $1. < |\eta| < 1.4$, $1.4 < |\eta| < 2.$ and $2. < |\eta| < 3.$. However, for the case of type 2 tau candidates the correction factors for each η region were found to be independent of the energy. Figure 5.12 shows these correction factors, which were calculated requiring that the most probable value of the FED function in each energy bin was zero. Since the FED distributions in each of these bins has pronounced negative tails, the overall mean is consistently about 4 % below zero for taus with calorimeter cluster energy greater than 25 GeV. To compensate for that, the correction factors for those type 2 tau candidates were multiplied with a factor of 1.025. Compared to using a factor of 1.04, this has the advantage of maintaining a better overall resolution and keeping the most probable value of the FED in each energy bin closer to zero.

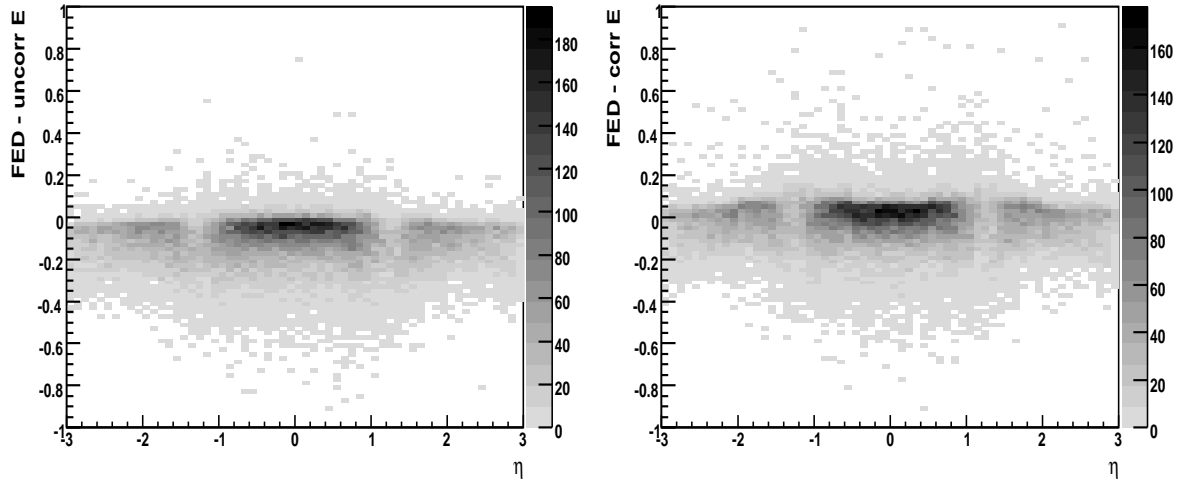


Figure 5.11. *FED distribution as a function of η for type 2 tau candidates, where the measured E of the tau candidate is given by the energy of the calorimeter cluster (left) or by the energy corrected using the optimized method (right).*

In addition to the energy measurement for the tau candidates which was used in DØ at the start of these studies (the calorimeter cluster uncorrected energy) and the previously described “optimized method”, two other correction procedures were studied.

One of them tried to take advantage of the fact that the majority of charged pions deposit all their energy in the hadronic part of the calorimeter, while the neutral pions

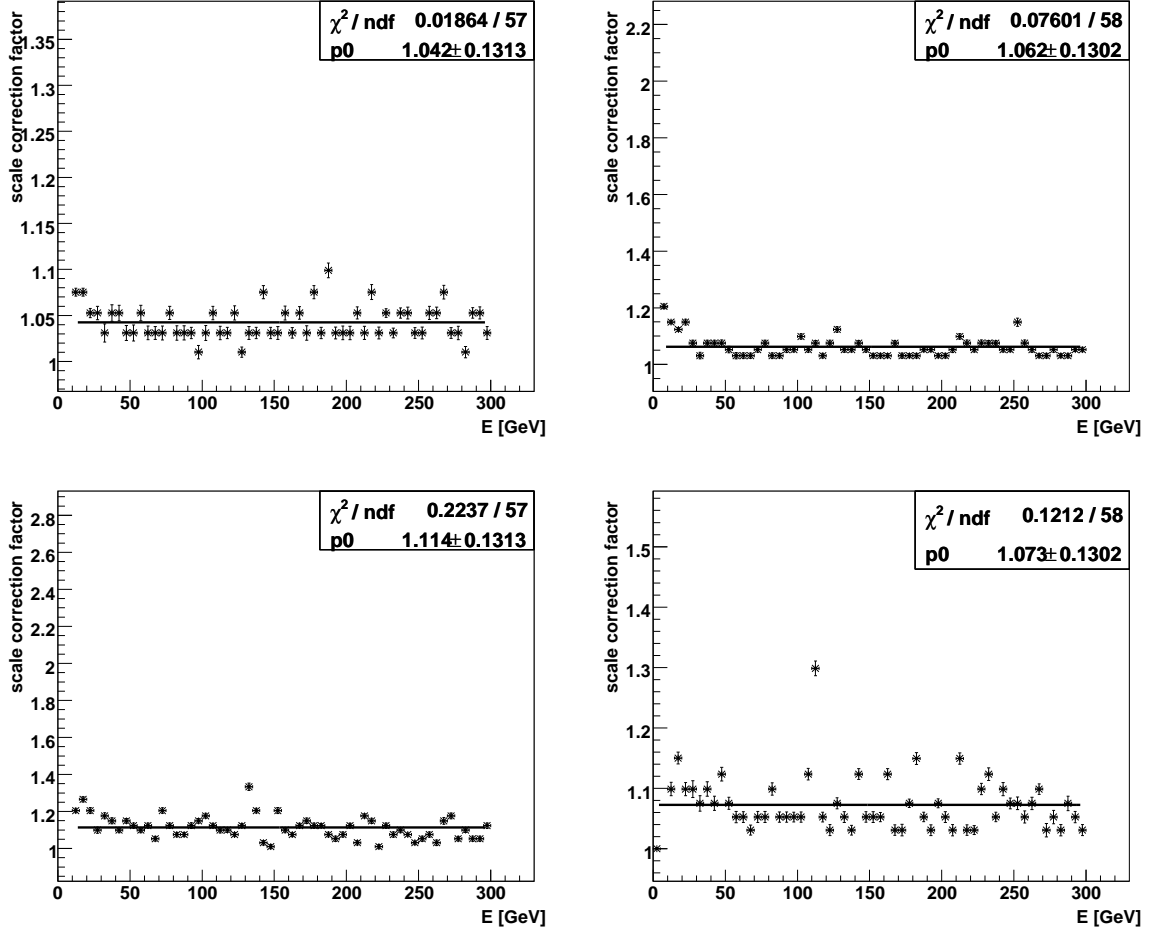


Figure 5.12. Tau energy scale factors for type 2 tau candidates as a function of calorimeter cluster energy in the 4 most central η regions: $0 < |\eta| < 0.5$ (upper left), $0.5 < |\eta| < 1$ (upper right), $1 < |\eta| < 1.4$ (lower left), $1.4 < |\eta| < 2$ (lower right). For the $2 < |\eta| < 3$ region, a constant factor of 1.05 was obtained (not shown here).

decay electromagnetically and form EM subclusters. The method consisted in using the momentum of the track associated to the tau candidate as an energy measurement for the charged pion, and the energy deposited by the tau candidate in the EM layers minus the average energy deposited by the charged pion in those layers as an energy measurement for the neutral pions. The corrected energy took therefore the following form:

$$E_{(T)}^{\text{corr}} = p_{(T)}^{\tau\text{-}trk} + E_{(T)}^{\text{EM}} - R_{EM}(p_{(T)}^{\text{trk}}, \eta) \cdot p_{(T)}^{\text{trk}}, \quad (5.5)$$

where $p_{(T)}^{\tau-trk}$ is the (transverse) momentum of the track associated to the tau candidate, $E_{(T)}^{EM}$ is the (transverse) energy deposited by the tau lepton in the EM layers of the calorimeter and $R_{EM}(p_{(T)}^{trk}, \eta)$ is the average fraction of energy deposited in the EM region of the calorimeter by the charged pions as a function of their energy and rapidity.

However, due to the longitudinal shower fluctuations, as well as the non-Gaussian distribution of the energy deposition of the π^\pm in the EM region of the calorimeter (about a quarter of the charged pions leave almost zero energy in the EM region, while the EM fraction distribution for the other three quarters is almost constant between 0.1 and 1 - see Fig. 5.13), using the average charged pion response in the EM layers led to an even worse resolution of the tau candidate energy compared to the one measured by the calorimeter.

A slightly different approach used the energy of the EM clusters instead of the whole EM energy. The difference between these two approaches was very small, therefore this method will not be presented in detail here.

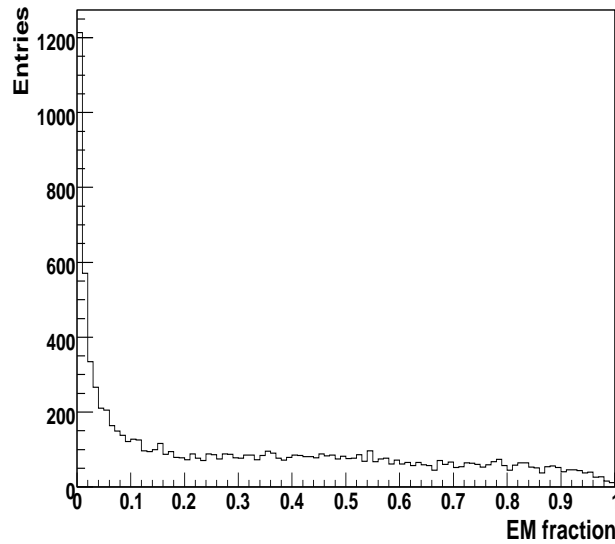


Figure 5.13. *The fraction of energy deposited by charged pions in the EM layers of the calorimeter.*

The fourth method studied was to use only the charged pion correction for all energies. This gave unsatisfactory results at high energies, due to a combination of two factors: first, the tracking resolution becomes worse with increasing momentum, and secondly, the charged pion response functions were obtained using charged pions with a maximum energy of 50 GeV, therefore the extrapolation becomes possibly unreliable at much higher energies. Figure 5.14 shows the FED distributions for the four methods mentioned here as a function of the true (generated) visible energy of the tau lepton. Figure 5.15 shows the FED mean and RMS for the four methods, while Fig. 5.16

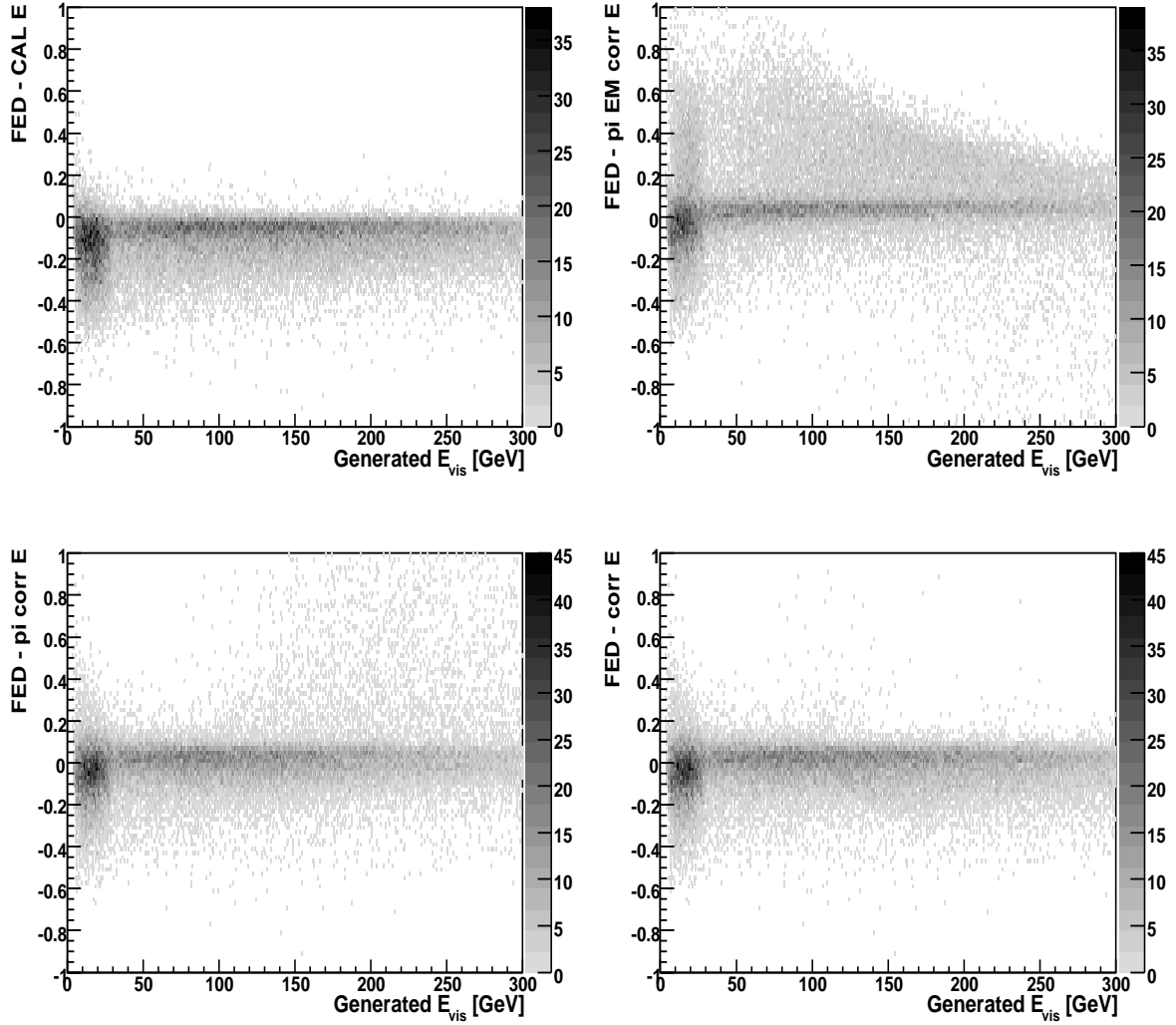


Figure 5.14. *FED* distribution for type 2 tau candidates as a function of the true (generated) visible energy of the tau lepton, for the measured energy in the *FED* function being the energy of the calorimeter cluster (upper left), the EM charged pion corrected energy (upper right), the corrected energy using the charged pion response (lower left) and the corrected energy with the optimized method (lower right).

illustrates the effect of the energy corrections on the visible energy spectrum of the tau candidates by comparing both spectra before and after the corrections were applied to the generated one.

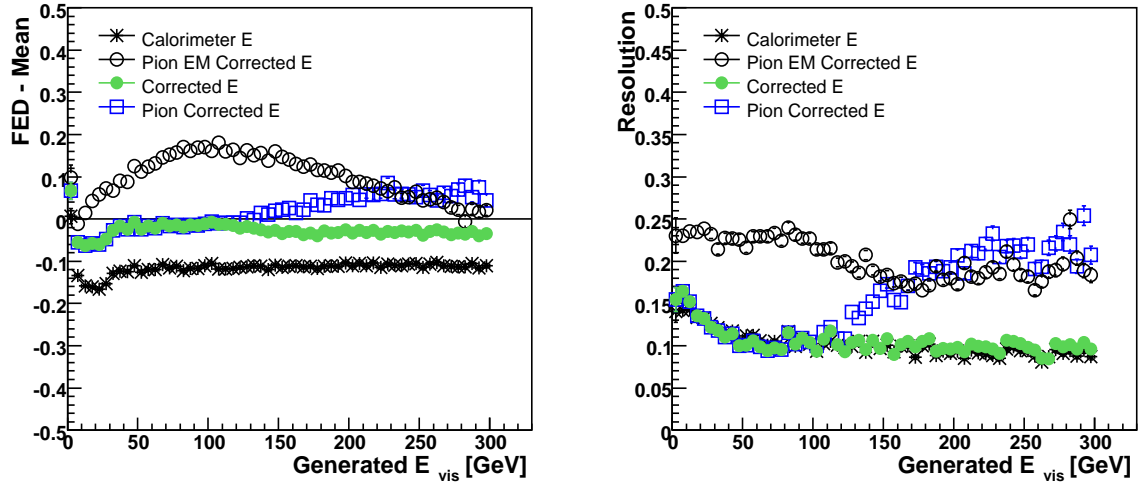


Figure 5.15. The FED mean (left) and FED RMS, or the resolution (right) for type 2 tau candidates as a function of the true (generated) visible energy of the tau lepton, for the measured energy in the FED function being the energy of the calorimeter cluster (asterisks), the EM charged pion corrected energy (empty circles), the energy corrected using the charged pion response (empty squares) and the energy corrected with the optimized method (filled circles).

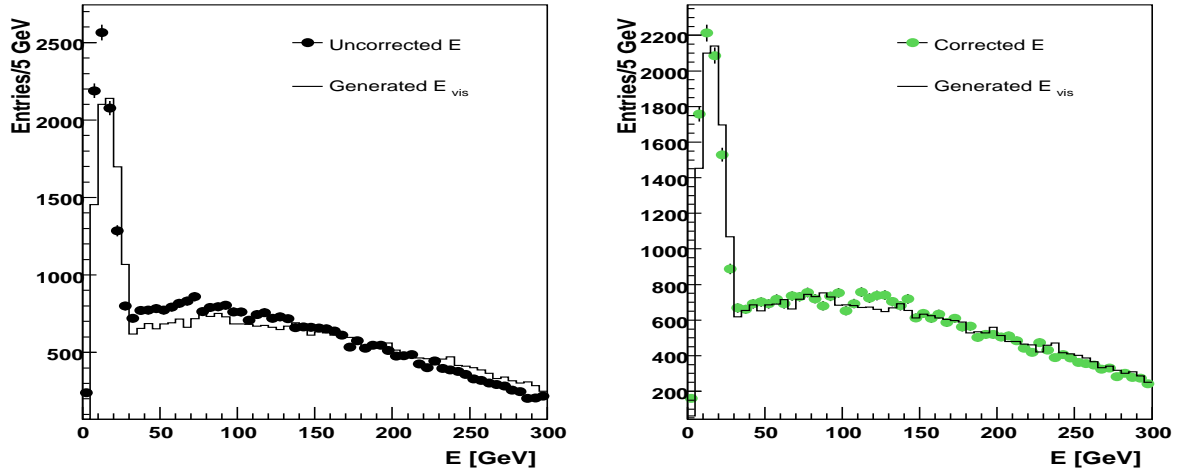


Figure 5.16. Energy spectra for type 2 tau candidates before (left) and after (right) applying the energy corrections. The dots represent the spectrum obtained using the calorimeter cluster energy (left) and the energy of the tau candidates corrected with the optimized method (right). For comparison, on both figures the generated visible energy spectrum is also shown (black line).

5.2.4 Energy correction for type 3 tau candidates

Exploiting again the better tracking resolution at low energies as well as the superiority of the calorimeter energy resolution at the high end of the spectrum, the corrected energy of a type 3 tau candidate is taken to be, similarly to the case of type 2 taus, either the pion response corrected energy (using Eq. 5.1) or the energy of the calorimeter cluster multiplied with a scale factor, depending on whether the uncorrected calorimeter cluster energy is lower or greater than 120 GeV, respectively. A further refinement is to use only the sum of the momentum of the associated tracks for the taus with a calorimeter cluster energy below 25 GeV, which deposit less than 0.1 of their transverse energy in the EM layers. As in the case of type 1 and type 2 tau candidates, the corrections applied to the calorimeter cluster energy are η dependent. The same five η regions as in the case of type 1 tau candidates were used. Figure 5.18 shows these correction factors, which were calculated requiring that the mean value of the FED function in each energy bin was zero. However, using the parametrized form of the correction factors led to the overall mean to be consistently about 2 % below zero for very high energies. To compensate for that, the correction factors for all type 3 tau candidates with calorimeter cluster energy higher than 125 GeV were multiplied with a factor of 1.02. Figure 5.17 shows the FED distribution as a function of η , both before and after the corrections were applied.

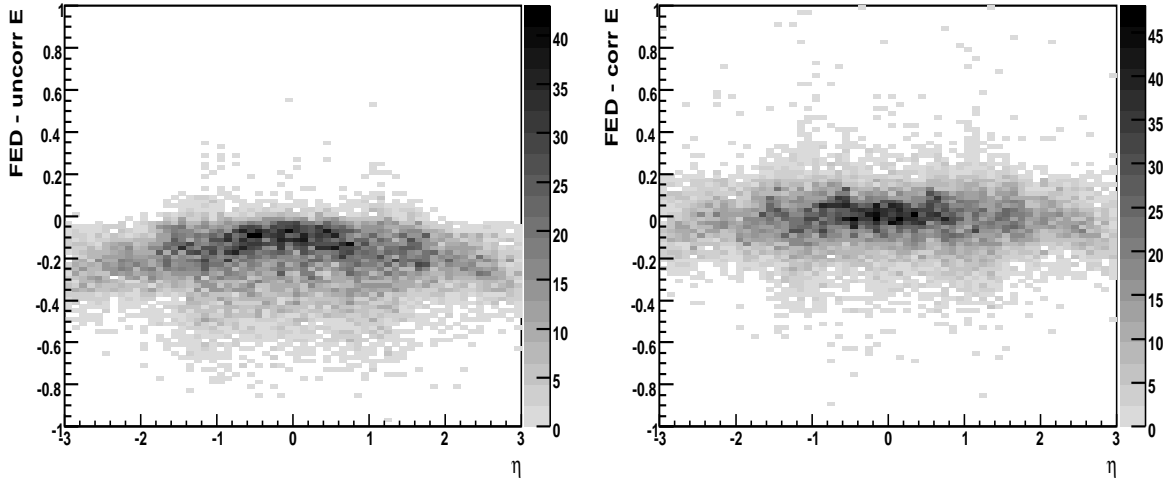


Figure 5.17. *FED* distribution as a function of η for type 3 tau candidates, where the measured E of the tau candidate is given by the energy of the calorimeter cluster (left) or by the corrected energy using the optimized method (right).

In addition to the calorimeter cluster energy and the optimized method described above, two other correction procedures were studied. One option was to use only the charged pion correction method over the whole energy range. As expected, this gave

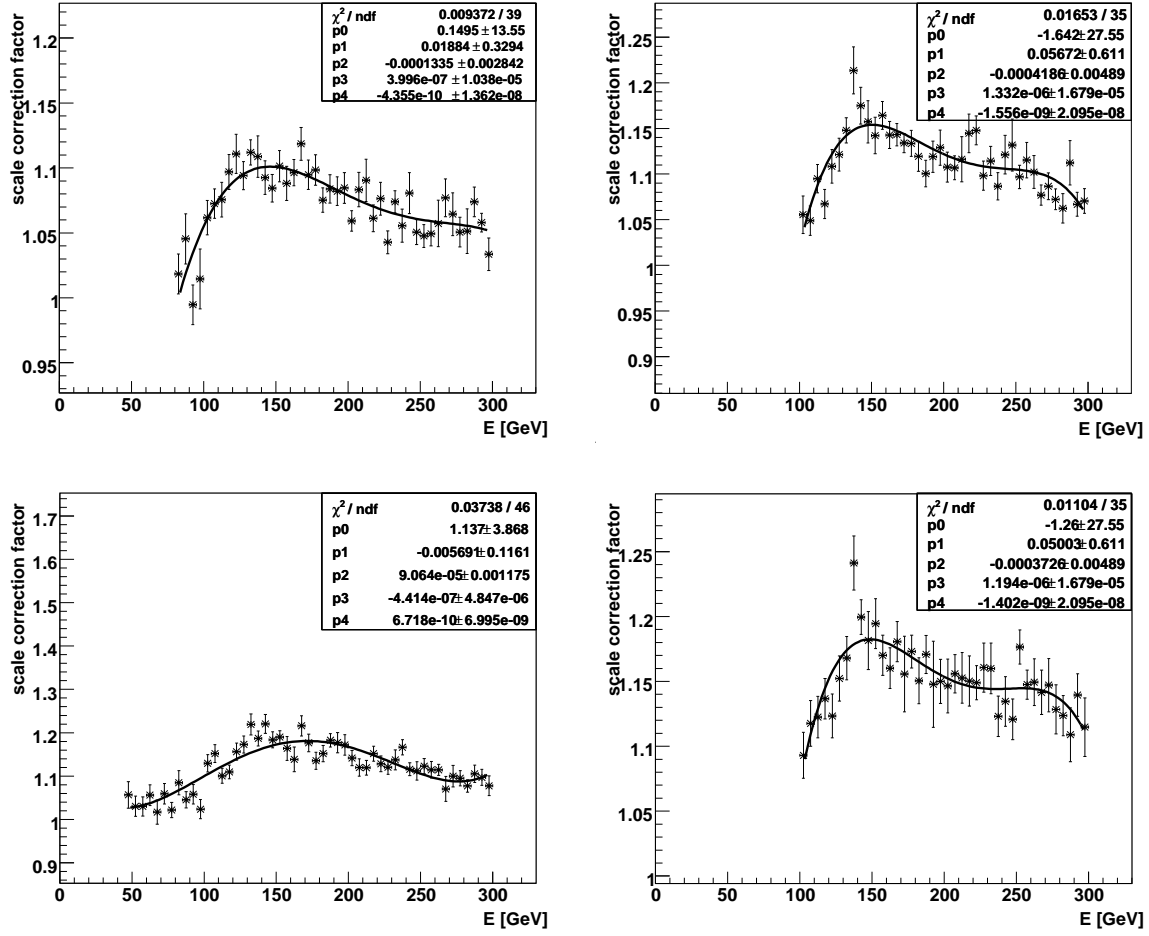


Figure 5.18. Tau energy scale factors for type 3 tau candidates in the η regions $0 < |\eta| < 0.5$ (upper left), $0.5 < |\eta| < 0.9$ (upper right), $0.9 < |\eta| < 1.4$ (lower left), $1.4 < |\eta| < 3$ (lower right). For the $2 < |\eta| < 3$ region, an additional multiplicative factor of 1.06 was used (not shown). On the horizontal axis, E denotes the charged pion corrected energy for the tau candidates with calorimeter cluster energy $E < 100$ GeV, and the calorimeter cluster energy for the rest of the tau candidates.

unsatisfactory results at high energies, due to a combination of the two factors mentioned in the previous chapter about the energy correction of type 2 tau candidates: the tracking resolution becoming increasingly worse with higher energies, and the possible unreliability of the extrapolation of the charged pion response functions beyond 50 GeV. The fourth method was very similar to the optimized method, except that it did not distinguish the tau candidates with low depositions of energy in the EM layers (assumed to correspond to decays into charged pions only) from the other ones at energies below 25 GeV, as was done in the optimized method. Figure 5.19 shows the FED

distributions for the four methods mentioned here as a function of true (generated) visible energy of the tau lepton. Figure 5.20 shows the FED mean and RMS as a function of true visible energy of the tau leptons for the four methods discussed above, while Fig. 5.21 illustrates the effect of the energy corrections on the visible energy spectrum of the tau candidates by comparing both spectra before and after the corrections were applied to the generated one.

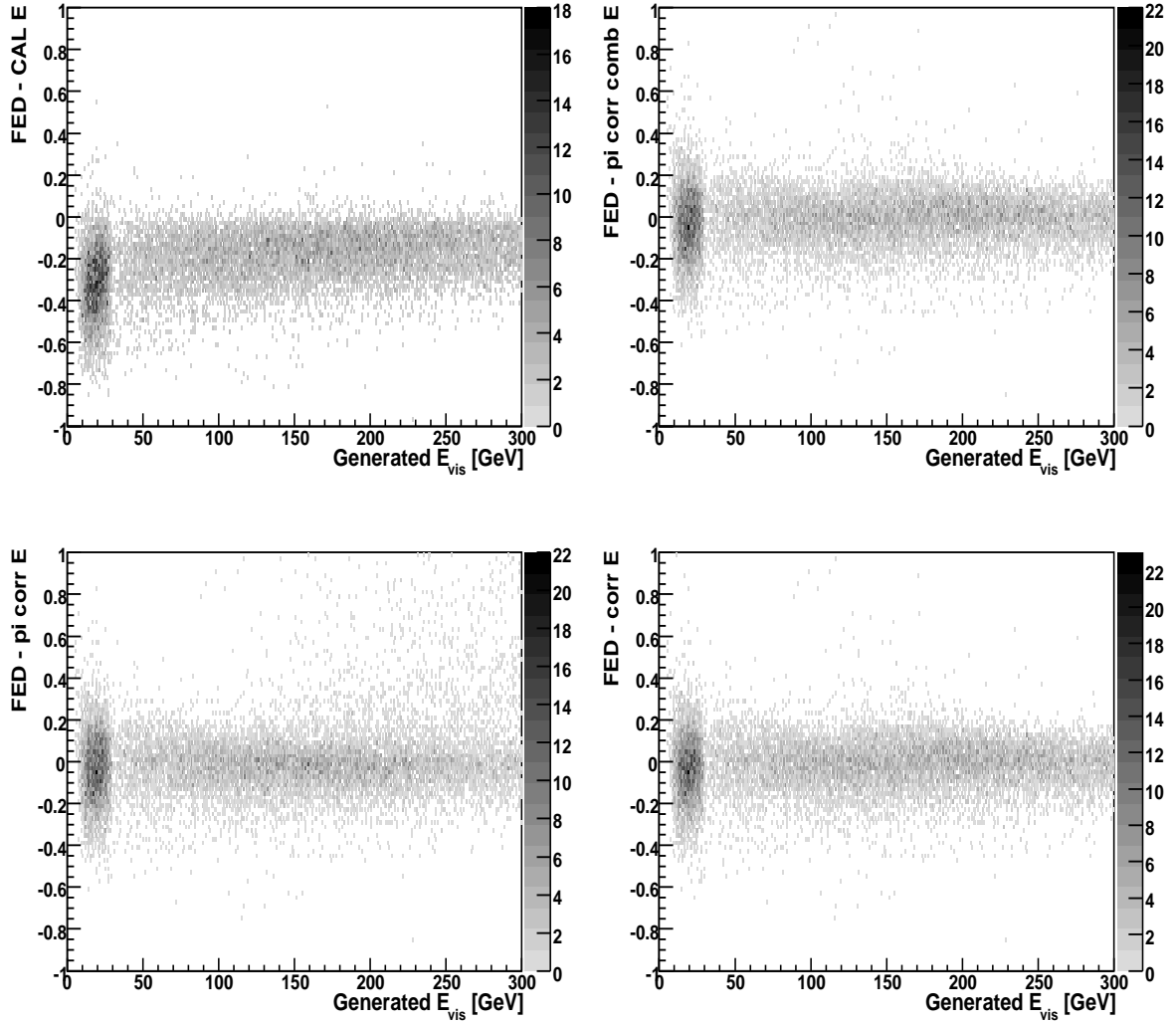


Figure 5.19. *FED* distribution for type 3 tau candidates as a function of the true (generated) visible energy of the tau lepton, for the measured energy in the *FED* function being the energy of the calorimeter cluster (upper left), the charged pion + CAL corrected energy (upper right), the energy corrected using the charged pion response (lower left) and the corrected energy with the optimized method (lower right).

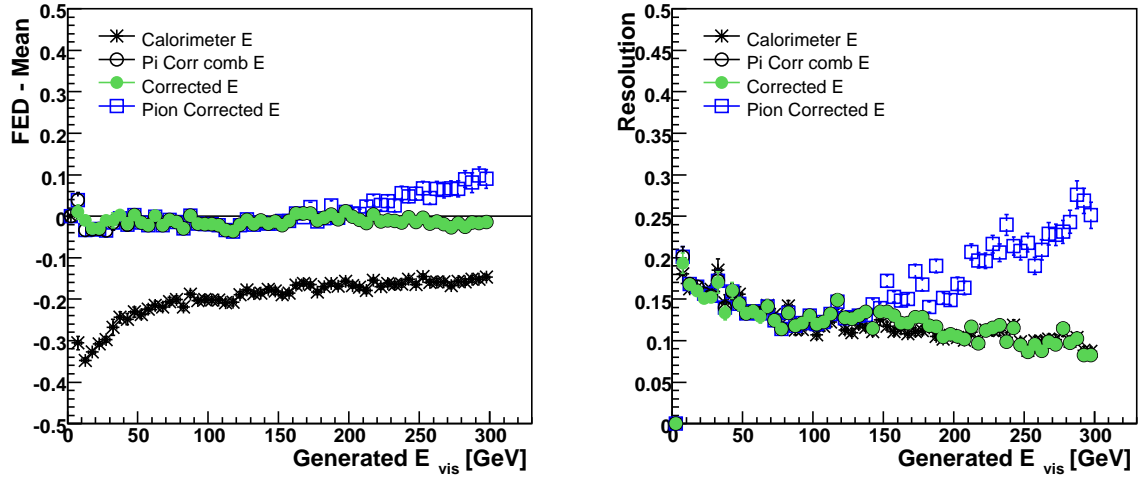


Figure 5.20. The FED mean (left) and FED RMS, or the resolution (right) for type 3 tau candidates as a function of the true (generated) visible energy of the tau lepton, with the measured energy in the FED function being the energy of the calorimeter cluster (asterisks), the charged pion + CAL corrected energy (empty circles), the energy corrected using the charged pion response (empty squares) and the corrected energy with the optimized method (filled circles).

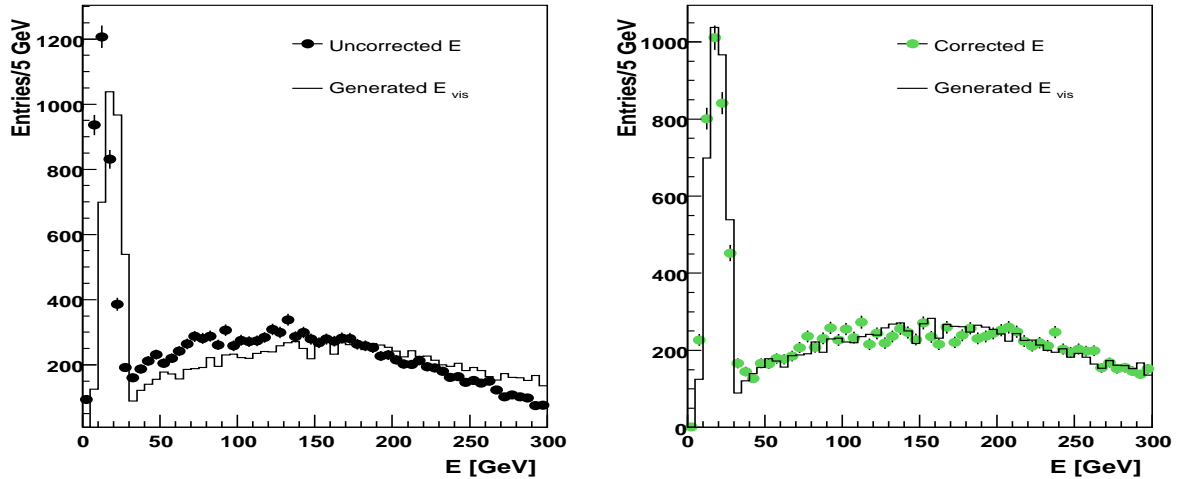


Figure 5.21. Energy spectra for type 3 tau candidates before (left) and after (right) applying the energy corrections. The dots represent the spectrum obtained using the calorimeter cluster E (left) the energy of the tau candidates corrected with the optimized method (right). For comparison, on both figures the generated visible energy spectrum is also shown (black line).

5.2.5 Energy corrections for data

Since the charged pion response in data is not perfectly reproduced in MC, different response curves were used for data. They were obtained using gCALOR [74] instead of GEISHA [70] (the default code used for the simulation of hadronic interactions in MC). A limit of 260 ns on the charge collection time in the calorimeter was placed. This resulted in a better fit to the distributions measured in data (the default configuration for GEISHA used for MC production does not have a limit on the integration time). Figures 5.22 and 5.23 show the response curves for the different regions of the calorimeter. In this analysis the data is assumed to follow the response curves called “gCALOR”, shown in (light) green in Figs. 5.22 and 5.23. A detailed description of these corrections can be found in [69].

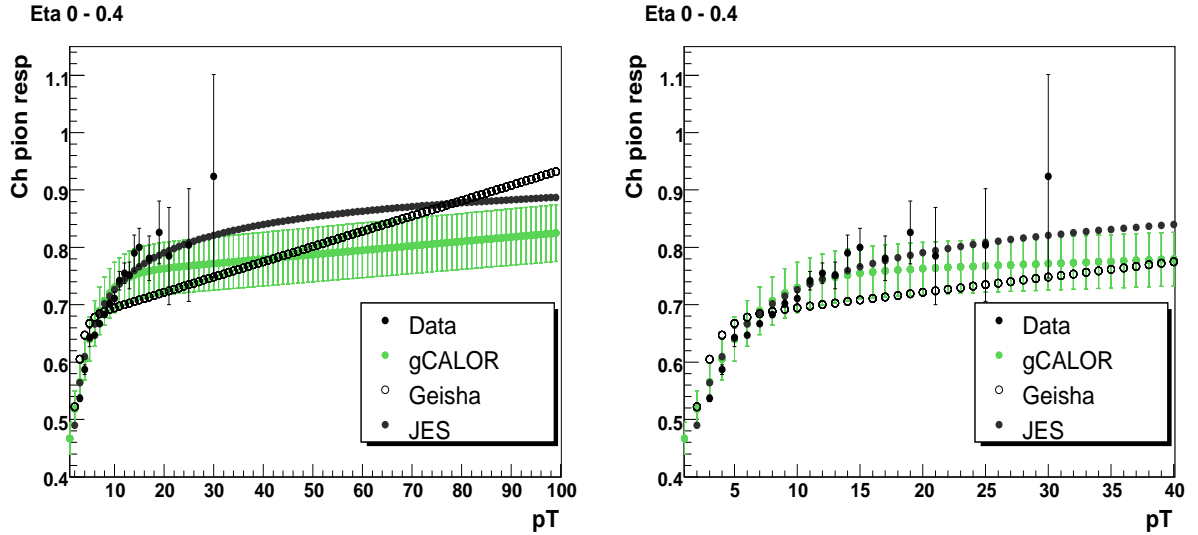


Figure 5.22. Charged pion response used for correcting the energy of the tau candidates in data and MC, in the calorimeter regions $|\eta| < 0.4$. The right plot is a blown-up version of the left plot for the low energy region. Both plots also show the 6 % systematic error on the charged pion response which was used for data.

Several things should be mentioned regarding Fig. 5.22. First, the charged pion measurement in data [64] is a very preliminary result. The data points are background subtracted, therefore the contribution to the response from noise is not included (but this affects more the very low energy regions, as the effect of the noise scales as $1/p_T$) and has a possible trigger bias for energies higher than 10 GeV due to electrons misidentified as pions. According to [64] the most reliable region for the data points is 5-10 GeV, where they agree very well with the gCALOR prediction. The curve labeled “JES” is obtained by the Jet Energy Scale (JES) group using a tuning of the standard MC (with hadronic interactions simulated by GEISHA). The cell level energies deposited by hadrons were scaled in such a way that their sum reproduces the jet response measured in data at very high energies [64]. The response obtained using this method does not

necessarily correspond to the single charged pion response, since the zero suppression algorithm has a different effect in jets compared to isolated pions. Also, even in jets of 500 GeV, only less than 9 % of the pions have energies higher than 30 GeV, with the average pion energy in jets being 11 GeV. Therefore the JES method is expected to make use of mostly low energy pions and extrapolate to higher energies. Finally, the gCALOR and GEISHA curves were obtained using a cone size of 0.3, while for the data points the cone size was 0.5 and for the JES curve a cone size of 0.7 was used. While the charged pion is expected to deposit most of its energy in the $R < 0.3$ cone, the use of larger cone sizes will lead to higher response due to the noise in the detector.

The systematic uncertainty related to this estimation was chosen to be a fixed fraction of the charged pion response obtained using gCALOR, namely 6 %. This value covers the difference between the charged pion response obtained using gCALOR and the one obtained using GEISHA, as well as the difference between the gCALOR estimation and a fit to the data points.

At the time this analysis was completed, the measurements done using gCALOR were available only up to $|\eta| < 1.6$. Those measurements were used to obtain fitting functions for each η region [69]. The function used for the fits was the same as the one used for fitting the GEISHA measurements, given by eq. 5.2. The fit parameters corresponding to the gCALOR measurements for each η region are listed in Table 5.4. A list of the fit parameters resulting from the fits to the measurements using GEISHA can be found in Table 5.3.

To obtain a “gCALOR like” response for the $1.6 < |\eta| < 2.$ region, the response predicted using GEISHA in this region was scaled for each value of the charged pion momentum by the ratio of gCALOR and GEISHA responses in the $1.2 < |\eta| < 1.6$ region corresponding to that particular momentum.

A comparison of the charged pion response obtained using GEISHA and gCALOR in different η regions of the detector is shown in Fig. 5.23.

The effects of using the tau energy corrections on the tau p_T and missing E_T spectra, as well as on the visible mass distributions for each tau type and for the sum of all types, both in data and MC, are described in detail in [69]. A general improvement in the agreement between data and MC was observed after the tau energy corrections were applied. The overall effect of applying these corrections on the visible mass distribution was an absolute/relative decrease in the RMS of this distribution of 7%/11% in data.

	$0. < \eta < 0.4$	$0.4 < \eta < 0.8$	$0.8 < \eta < 1.2$	$1.2 < \eta < 1.6$
p_0	0.401054	0.441244	0.412186	0.318560
p_1	0.325825	0.282039	0.269793	0.362584
p_2 [GeV]	6.252340	7.654280	8.644190	8.686660
p_3 [GeV ⁻¹]	0.0007483	0.0004942	0.0017234	0.0013647

Table 5.4. *Fit parameters for the charged pion response in Monte Carlo using gCALOR for the simulation of hadronic interactions.*

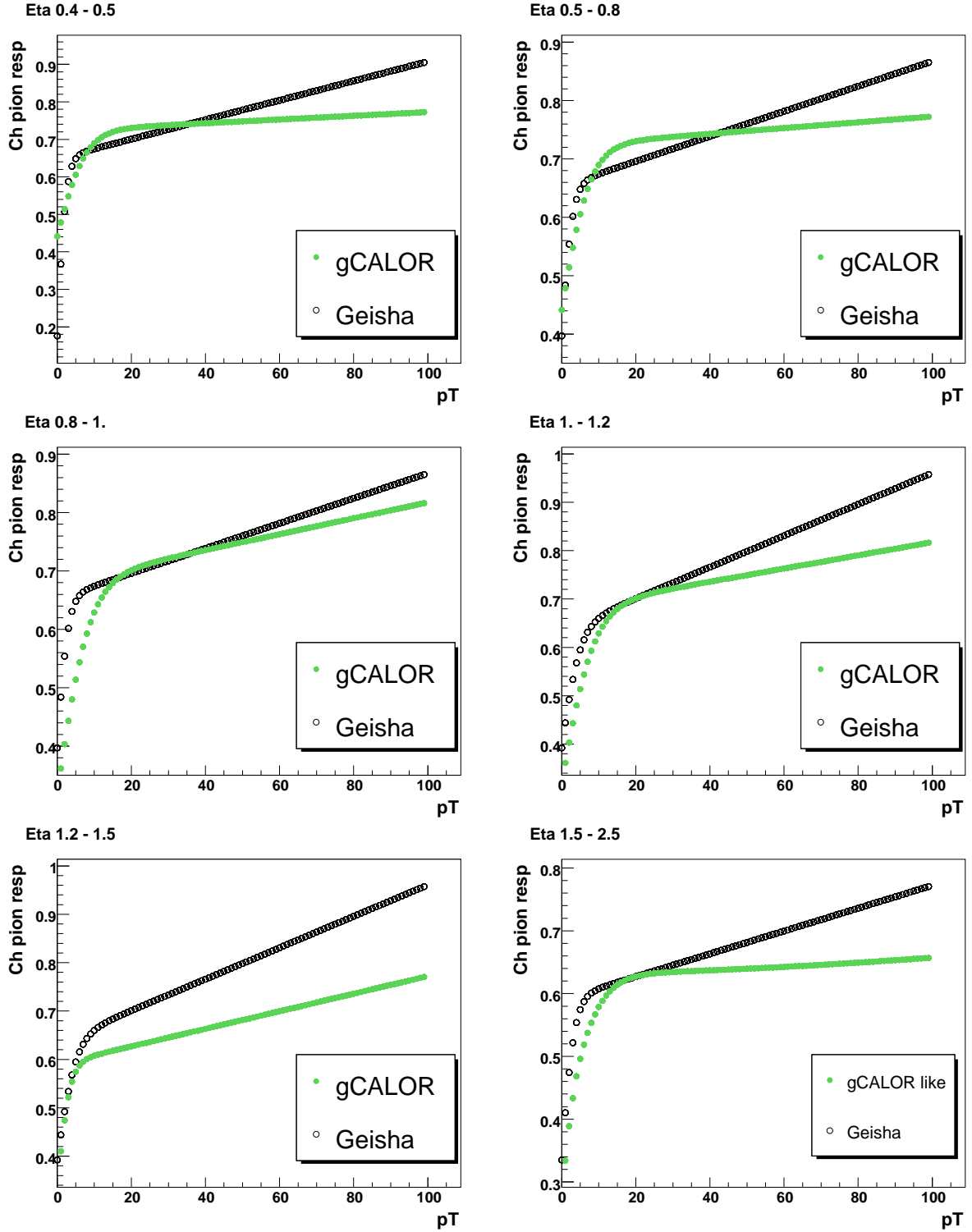


Figure 5.23. Charged pion response as a function of the pion p_T [GeV] used for correcting the energy of the tau candidates in data and MC, in the calorimeter regions $0.4 < |\eta| < 0.5$ (upper left), $0.5 < |\eta| < 0.8$ (upper right), $0.8 < |\eta| < 1.$ (middle left), $1. < |\eta| < 1.2$ (middle right), $1.2 < |\eta| < 1.5$ (lower left) and $1.5 < |\eta| < 2.5$ (lower right).

5.2.6 Missing E_T correction

In order to propagate the energy corrections described above to the missing E_T , we replaced in the \cancel{E}_T calculation the JES corrected energy of the jet which matched the selected tau candidate with the corrected energy of the tau candidate. In the rare cases when no jet matched the tau candidate, the uncorrected energy of the tau candidate was replaced in the missing E_T calculation by its corrected energy. When the tau candidate matched a reconstructed electron no corrections related to the energy of the tau candidate were applied to the missing E_T , since the appropriate electromagnetic response corrections have already been applied. For details on the effects of these corrections in Monte Carlo see [71]. For a comparison between corrected and uncorrected \cancel{E}_T distributions after all cuts in this analysis were applied see [69].

6

Z boson cross section measurement

A measurement of the cross section for Z boson production times the branching ratio of Z boson decaying into tau lepton pairs $\sigma \cdot \text{Br}(Z \rightarrow \tau^+ \tau^-)$ in $p\bar{p}$ collisions at $\sqrt{s} = 1.96$ TeV is described in this chapter. One of the two tau leptons resulting from the Z boson decay is required to decay into a muon and neutrinos, while the other tau lepton is required to decay either hadronically or into an electron and neutrinos. While the branching ratio for the tau lepton to decay into a muon is only 17 %, this channel presents a clear signature of an isolated muon, which helps to distinguish between true $Z \rightarrow \tau^+ \tau^-$ events and the much more abundant multijet QCD events. The presence of a muon in the event is also essential for triggering. Finally, less complications are encountered in this channel compared to the one in which one of the tau leptons decays into an electron, which suffers from a high background due to $Z \rightarrow e^+ e^-$ events.

6.1 Data set

The analysis is based on data collected by the DØ experiment between April 2002 and February 2006 (the whole Run IIa data set). All events were required to fulfill initially either of the following requirements:

- at least one loose muon with a transverse momentum $p_T > 8$ GeV measured with the central tracking detectors;
- at least one loose muon with a transverse momentum $p_T > 5$ GeV measured with the central tracking detectors, at least two tracks with $p_T > 5$ GeV and $p_T > 8$ GeV, respectively, and one tau candidate with $p_T > 5$ GeV as measured by the calorimeter;

Good data quality was assured by rejecting events from all data taking periods in which any of the sub-detectors was not fully operational, as well as events with recognizable noise patterns in the calorimeter.

A single muon trigger was required for each event. The four different triggers corresponding to four major changes in trigger lists are listed in Table 6.1. The luminosity listed for each trigger was calculated after the removal of all events from data taking periods in which any of the sub-detectors was not fully operational. Data from luminosity blocks (*i.e.*, short data taking periods, each corresponding to 1 minute of running) in which the trigger was not valid or normalizable were also rejected in the analysis.

Each trigger consists of a set of requirements at each level of the trigger system, called “terms”. The Level 1 terms for the triggers used in this analysis are defined as follows [75]: the “tight muon scintillator” term requires a coincidence between a hit in the inner scintillator layer and one in the scintillator layer outside the toroid magnet found within a certain distance in η and ϕ from the first hit, while the “loose wire” term requires an A-layer PDT or MDT hit confirmed by an A ϕ or A-layer pixel hit. The Level 2 muon triggers are described in detail in [76]. A “Level 2 medium muon” is required to have at least 3 PDT hits in the A-layer and 3 PDT hits in the B-layer if the muon is central ($|\eta| < 1$) or at least 3 hits in either MDT or pixel detectors of the A layer plus 2 MDT hits in either the B or C layers if it is forward ($1 < |\eta| < 2$).

Trigger List Version	Triggers	Luminosity [pb^{-1}]
v8 - v10.03	MU_W_L2M5_TRK10	31.4
v10.30 - v12.37	MUW_W_L2M3_TRK10	302.3
v13	MUH1_TK12	17.0
	MUH1_TK12_TLM12	336.6
v14	MUH1_TK12_TLM12	316.0
all	all	1003.3

Table 6.1. *Triggers used in the analysis, with the trigger list versions to which they correspond and their luminosity after all data quality criteria have been applied.*

The trigger definitions were:

- MU_W_L2M5_TRK10:
 - Level 1: one muon inside the CFT (wide) region ($|\eta| < 1.5$) passing tight muon scintillator requirement;
 - Level 2: one medium muon with $p_T > 5$ GeV;
 - Level 3: one track with $p_T > 10$ GeV.
- MUW_W_L2M3_TRK10:
 - Level 1: one muon inside the CFT (wide) region ($|\eta| < 1.5$) passing tight scintillator and loose wire requirements;
 - Level 2: one medium muon with $p_T > 3$ GeV;
 - Level 3: one track with $p_T > 10$ GeV.
- MUH1_TK12_TLM12 (or MUH1_TK12):
 - Level 1: one muon inside the CFT (wide) region ($|\eta| < 1.6$) passing tight muon scintillator requirement and one track with $p_T > 10$ GeV;
 - Level 2: no requirement;
 - Level 3: one muon with $p_T > 12$ GeV, matched to a central track.

6.2 Trigger efficiency

The efficiencies for the Level 1, Level 2 and Level 3 terms of each single muon trigger used in this analysis were computed using a method called “tag and probe” on $Z \rightarrow \mu^+\mu^-$ events [59]. The tag and probe method requires a control muon which meets the following criteria:

- the muon must be of “loose” quality;
- the time when the hit in the A-layer scintillator is registred (or B-layer scintillator, if there are no hits in the A-layer scintillator) must be at most 7 ns after a bunch crossing took place;
- the muon must be matched to a track of “medium” quality with $p_T > 30$ GeV;
- the sum of energies of all cells situated in a hollow cone around the direction of the muon with $0.1 < R < 0.4$ and the sum of all tracks in a cone of $R < 0.5$, excluding the muon track, had to be less than 2.5 GeV and 3.5 GeV, respectively;
- at least one single muon trigger must have fired in the event.

The probe had to fulfill the following requirements:

- a track of “loose” quality with $p_T > 20$ GeV;
- the sum of energies of all cells situated in a hollow cone around the direction of the track with $0.1 < R < 0.4$ had to be less than 2.5 GeV, while the sum of all tracks in a cone of $R < 0.5$, excluding the probe track, had to be less than 3.5 GeV;
- acollinearity between tag and probe ($\pi - |\phi_1 - \phi_2| + |\pi - \theta_1 - \theta_2|$) < 0.025 , where ϕ_1 and θ_1 are the azimuthal and polar angles of the tag muon and ϕ_2 and θ_2 are the azimuthal and polar angles of the probe;
- $|z_{tag} - z_{probe}| < 2$ cm, where z is the coordinate of the central track measured at the point of its closest approach to the z axis.

A sample of 92500 events selected from data, spanning the whole data taking period of this analysis, met these requirements and was used for calculating the efficiencies for the different trigger terms. The Level 1 efficiencies were measured with respect to loose muons reconstructed offline and all subsequent efficiencies are determined with respect to muons that have passed all the previous requirements.

Figures 6.1, 6.2, 6.3, 6.4, 6.5 and 6.6 show the trigger efficiencies at Level 1, Level 2 and Level 3 for all triggers used in this analysis, as a function of different parameters, usually η and ϕ or z .

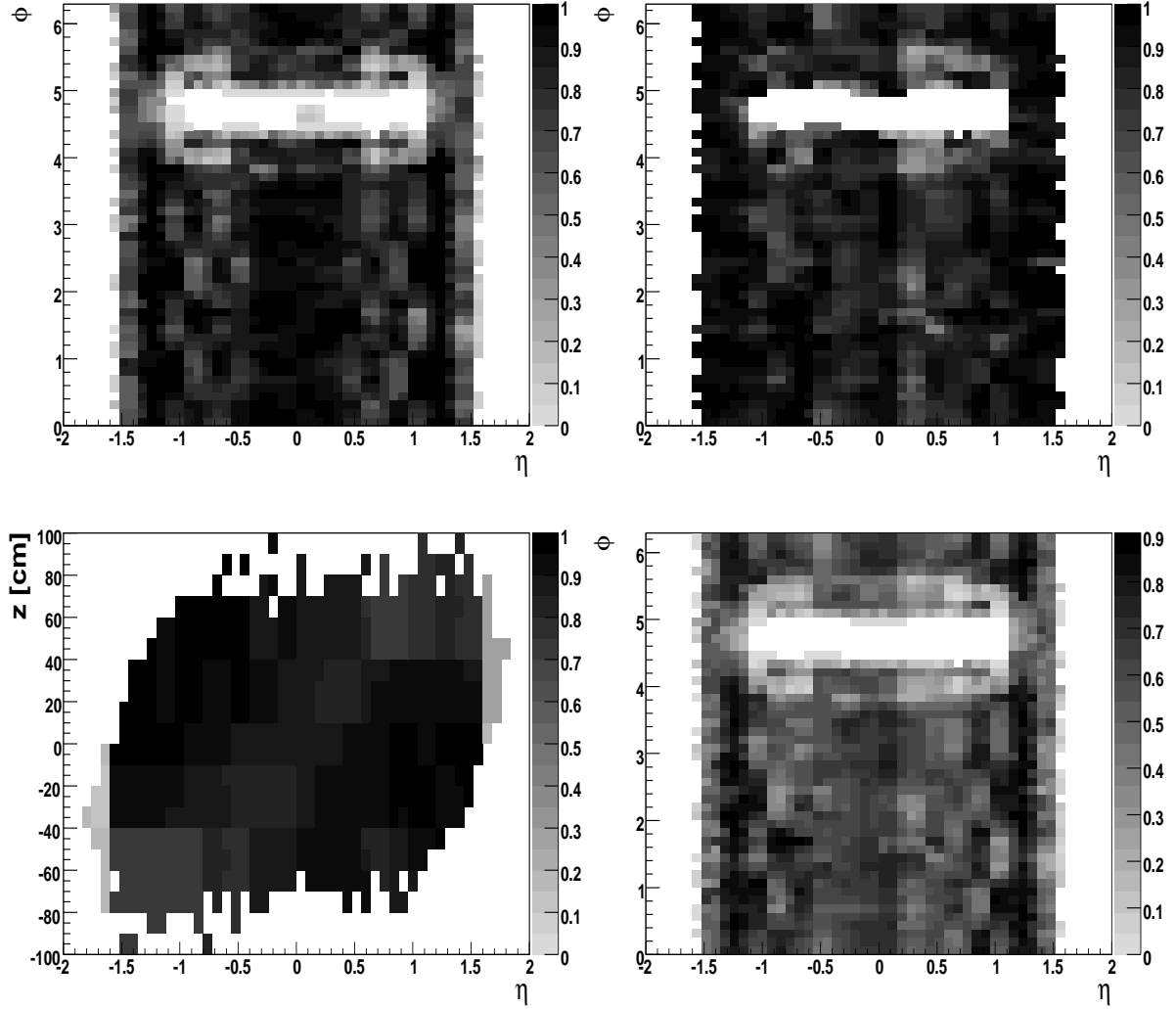


Figure 6.1. *Efficiencies for the MU_W_L2M5_TRK10 trigger: the efficiency as a function of detector η and ϕ for the tight scintillator term at Level 1 (upper left), the efficiency for finding a medium muon with $p_T > 5$ GeV (as measured in the muon chambers) at Level 2 with respect to muons that have passed the Level 1 muon tight scintillator term, as a function of detector η and ϕ (upper right), the efficiency for reconstructing a track with $p_T > 10$ GeV at Level 3 with respect to events with an offline reconstructed loose track as a function of detector η (as measured at the CFT) and the z position of the muon (lower left) and the overall efficiency for the MU_W_L2M5_TRK10 trigger, as a function of detector η and ϕ (lower right).*

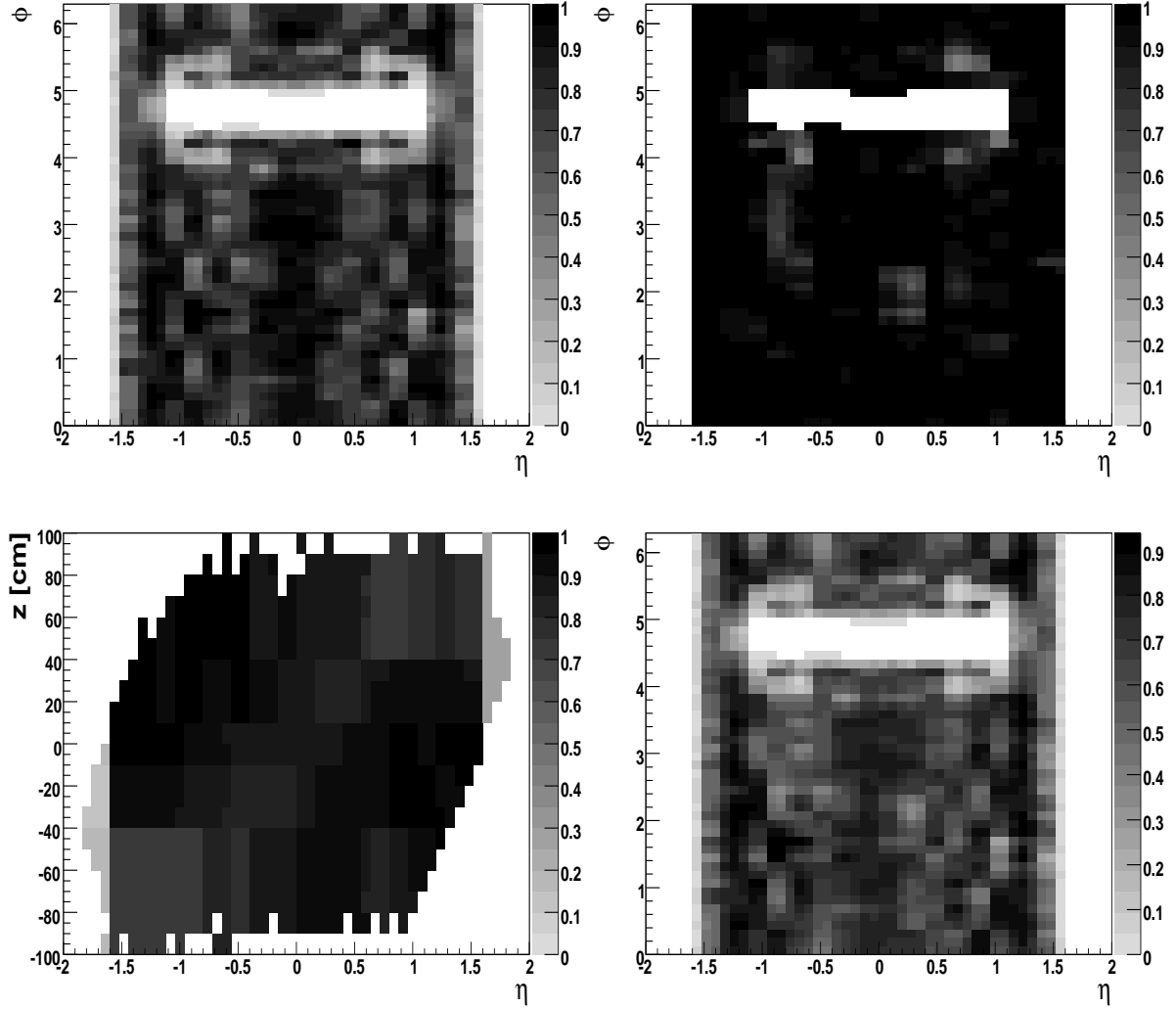


Figure 6.2. *Efficiencies for the MUW_L2M3_TRK10 trigger: the efficiency as a function of detector η and ϕ for the tight scintillator and loose wire term at Level 1 (upper left), the efficiency for finding a medium muon with $p_T > 3$ GeV (as measured in the muon chambers) at Level 2 with respect to muons that have passed the Level 1 muon tight scintillator loose wire term, as a function of detector η and ϕ (upper right), the efficiency for reconstructing a track with $p_T > 10$ GeV at Level 3 with respect to events with an offline reconstructed loose track as a function of detector η (as measured at the CFT) and the z position of the muon (lower left) and the overall efficiency for the MUW_L2M3_TRK10 trigger, as a function of detector η and ϕ (lower right).*

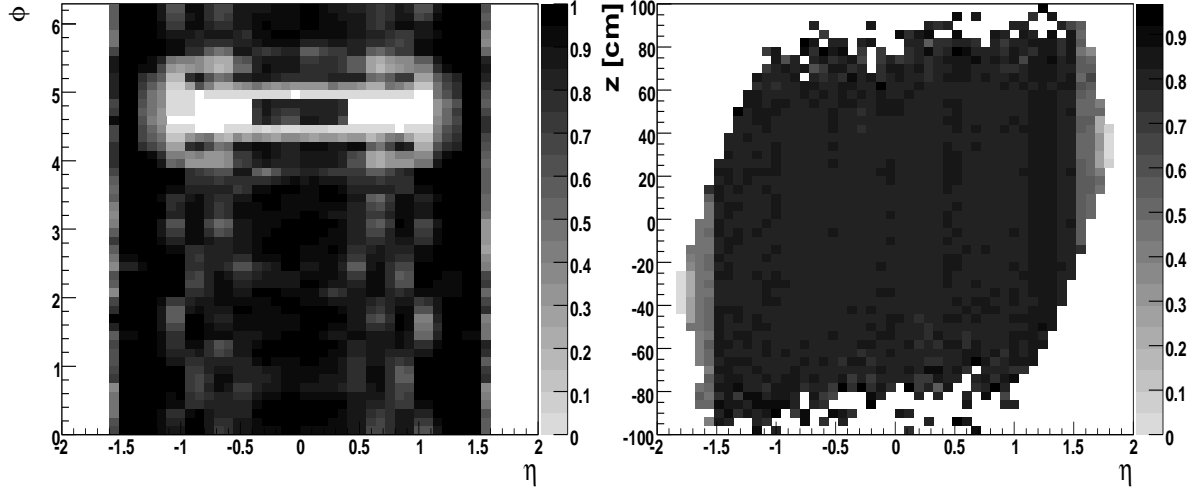


Figure 6.3. Efficiencies for the MUH1-TK12-TLM12 trigger (for v13 period): the efficiency as a function of detector η and ϕ for the tight scintillator term at Level 1 (left) and the efficiency for finding a track with $p_T > 10$ GeV at Level 1 with respect to events with a medium track found offline, as a function of z and detector η (right).

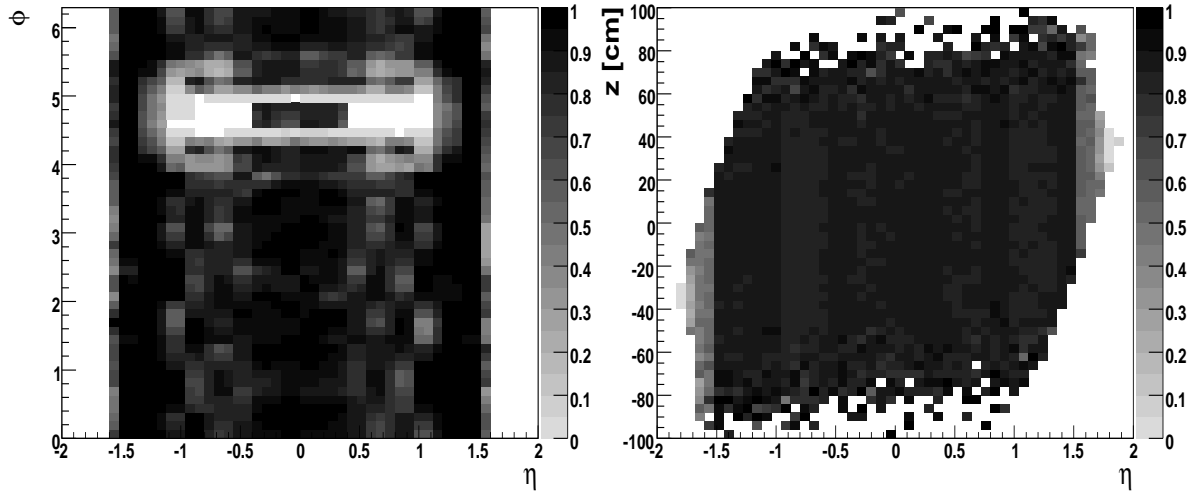


Figure 6.4. Efficiencies for the MUH1-TK12-TLM12 trigger (for v14 period): the efficiency as a function of detector η and ϕ for the tight scintillator term at Level 1 (left) and the efficiency for finding a track with $p_T > 10$ GeV at Level 1 with respect to events with a medium track found offline, as a function of z and detector η (right).

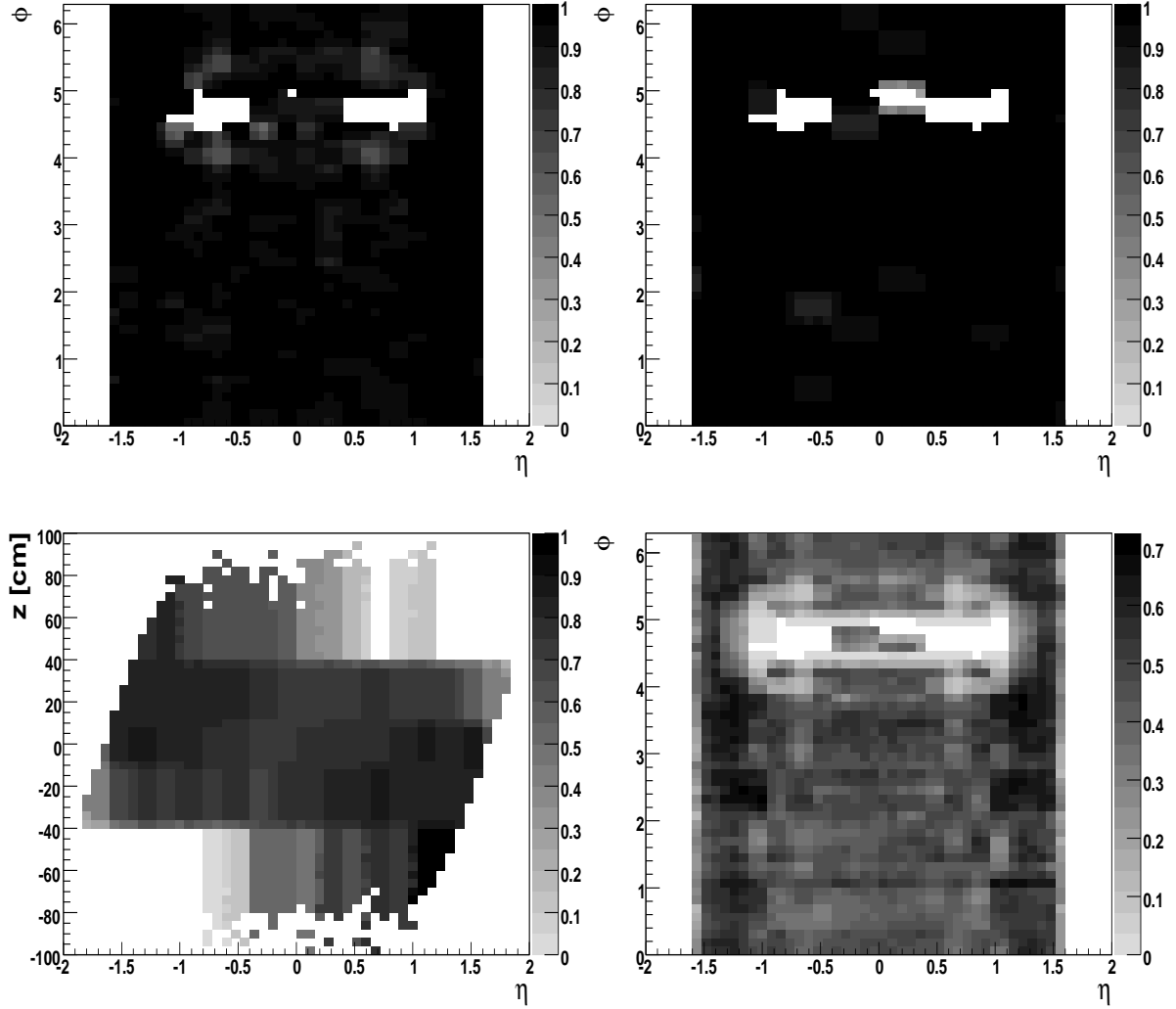


Figure 6.5. Efficiencies for the MUH1_TK12_TLM12 trigger (for v13 period): the efficiency for finding a loose muon at Level 3 with respect to events with an offline reconstructed loose track which passed the tight scintillator term at Level 1, as a function of ϕ and detector η (upper left), the efficiency to find a central track of 12 GeV matching a loose muon at Level 3, with respect to events which passed the tight scintillator term at Level 1, have a medium track reconstructed offline and passed the loose muon term at Level 3, as well as the Level 3 term requiring a track of at least 10 GeV (upper right), the efficiency for the events which passed the Level 1 requirement of having a track of at least 10 GeV, and which have an offline reconstructed track of medium quality or higher, to have a track of at least 12 GeV with 10 hits (lower left) and the overall efficiency for the MUH1_TK12_TLM12 trigger, as a function of detector η and ϕ (lower right).

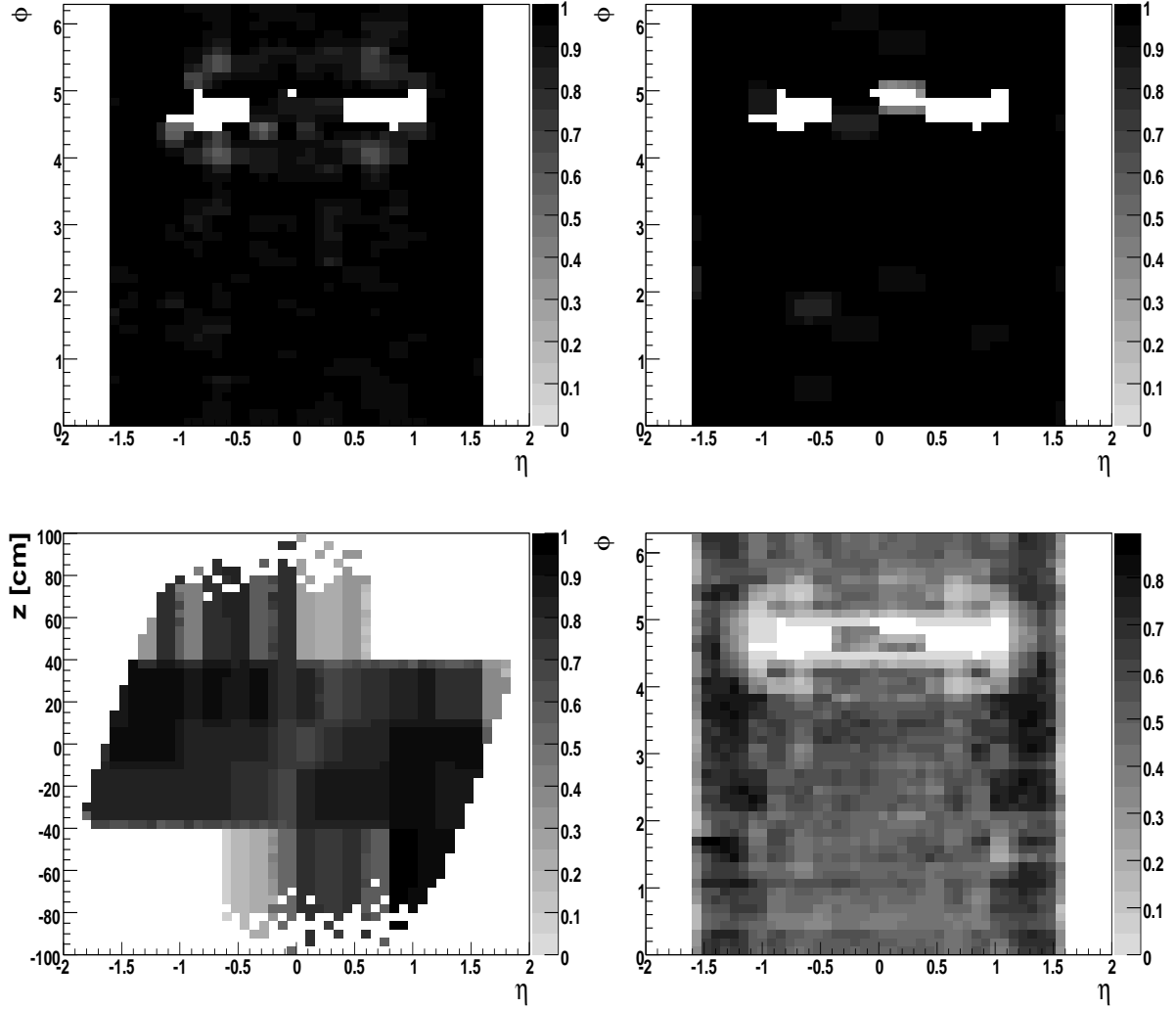


Figure 6.6. Efficiencies for the MUH1_TK12_TLM12 trigger (for v14 period): the efficiency for finding a loose muon at Level 3 with respect to events with an offline reconstructed loose track which passed the tight scintillator term at Level 1, as a function of ϕ and detector η (upper left), the efficiency to find a central track of 12 GeV matching a loose muon at Level 3, with respect to events which passed the tight scintillator term at Level 1, have a medium track reconstructed offline and passed the loose muon term at Level 3, as well as the Level 3 term requiring a track of at least 10 GeV (upper right), the efficiency for the events which passed the Level 1 requirement of having a track of at least 10 GeV, and which have an offline reconstructed track of medium quality or higher, to have a track of at least 12 GeV with 10 hits (lower left) and the overall efficiency for the MUH1_TK12_TLM12 trigger, as a function of detector η and ϕ (lower right).

The overall trigger efficiency was obtained by applying a weight to each MC event equal to the efficiency in the region of phase space occupied by the tagged muon for one of the four different trigger periods. Precisely which trigger period was chosen for a certain MC event was determined randomly while taking into account their respective integrated luminosities listed in Table 6.1.

The definition of the “wide” region changed from $|\eta| < 1.5$ to $|\eta| < 1.6$ with the introduction of the v13 trigger list. For this reason the efficiencies for the wide region trigger terms were split into two periods, before and after the introduction of v13.

The MUH1_TK12_TLM12 trigger was called MUH1_TK12 for a brief period when the v13 trigger list had just started to be used. This was just a name change, so the 17 pb^{-1} collected with MUH1_TK12 were simply added to the luminosity for the v13 period of the MUH1_TK12_TLM12 trigger. Due to a change in the Level 3 efficiency between the periods when the v13, respectively v14 trigger lists were used, the efficiency for the MUH1_TK12_TLM12 was calculated separately for the two periods.

To check for an eventual p_T dependence of the trigger efficiency, the requirement on the momentum of the probe track was lowered to 15 GeV and the efficiency was studied as a function of the momentum of the probe. No p_T dependence was observed for any of the triggers used in this analysis.

The presence of the tau candidate tracks in the event was estimated to lead to an overall increase of 6 % in the efficiency of the L3 track trigger, which was included in the analysis as a correction factor for the efficiency of the MU_W_L2M5_TRK10 and MUW_W_L2M3_TRK10 triggers. A correction of 3.5 % was applied to the estimated efficiency of the MUH1_TK12 and MUH1_TK12_TLM12 to account for the artificial decrease in the measured efficiency using the “tag and probe” method. The method required a match between an offline reconstructed loose track and a L1 track term to calculate the L1 tracking efficiency. However, for about 3.5 % of the events the L1 track term was not recorded due to problems with the readout of the CTT crate (the “crate x13 readout problem”), even though the trigger was actually functional.

The average trigger efficiencies for the four different periods were 55.7 %, 62.6 %, 44.9 % and 50.6 %. The overall trigger efficiency, given these numbers and the luminosities for each trigger was 52.3 %.

6.3 Event simulation

The contribution of the majority of backgrounds as well as the efficiency of the selection for signal $Z \rightarrow \tau^+\tau^-$ events were estimated using Monte Carlo (MC) simulations. All simulated samples were generated with PYTHIA [77] (version 6.323) using the CTEQ6.1L PDF set. The simulation of the DØ detector was done using GEANT3 [78]. The code used for the reconstruction of simulated events is equivalent to the one used for data. Small corrections were applied to all reconstructed objects to improve the agreement between simulation and collider data. In particular, the momentum scale and resolution for muons in the MC were tuned to reproduce the Z boson invariant mass

distribution observed in data. The MC jets were smeared in energy using a random Gaussian distribution to match the resolutions observed in data for different regions of the detector. Overall, good agreement is observed between reconstructed objects in data and MC.

The samples are normalized to the expected number of events evaluated using the luminosity of the data sample and the theoretical values of the NNLO cross sections in the case of Z production [79] or NLO cross sections for all other processes where the NNLO calculation is not available [13]. The W + jets production is normalized from data.

The noise in the detector and the contribution to the event coming from other simultaneous interactions were simulated using zero bias events coming from data. The data quality criteria, used to assure that these events were not affected by coherent noise or other problems with the detector, were the same as the ones applied on the data events. All simulated events with zero bias overlay consisting of collider data that are from periods of data taking in which any of the sub-detectors was not fully operational, as well as data affected by recognizable noise in the detector, were rejected before calculating the normalization of the number of events to theoretical cross sections. Table 6.2 shows the number of MC events contained in each of the samples used for simulation, after all data quality criteria were applied, as well as the values of the cross sections used for the normalization of the contributions corresponding to each of the considered processes.

Since the simulation does not perfectly reproduce the data, several additional corrections had to be applied to the MC events, described in detail in the following subsections.

Process	Mass Range	Number of events	Cross Section [pb]
$Z \rightarrow \tau^+ \tau^-$	15 - 60 GeV	1 757 279	409
	60 - 130 GeV	8 357 107	256.6
	130 - 250 GeV	383 225	1.96
	250 - 500 GeV	96 641	0.16
$t\bar{t} \rightarrow \text{incl.}$		187 128	6.77
$W \rightarrow \tau \nu$		5 889 668	2678
$WW \rightarrow l \nu l \nu$		94 022	1.67
$Z \rightarrow \mu^+ \mu^-$	15 - 60 GeV	1 965 564	409
	60 - 130 GeV	4 806 609	256.6
	130 - 250 GeV	389 120	1.96
	250 - 500 GeV	96 873	0.16
$W \rightarrow \mu \nu$		3 417 941	2678

Table 6.2. Number of MC events used for the simulation of each of the backgrounds, as well as for the $Z \rightarrow \tau^+ \tau^-$ signal simulation, after all data quality criteria were applied. Also shown are the values of the cross sections for each process used for normalization.

6.3.1 Z boson p_T reweighting

The p_T spectrum of the Z boson for events generated with PYTHIA is known to have a different shape compared to the one measured in data [80]. Therefore the p_T of the Z boson was reweighted to fit the differential Z boson cross section as a function of Z boson p_T obtained from Monte Carlo simulation to the one measured in data from [81]. The reweighting is described in [82].

6.3.2 Instantaneous luminosity profile reweighting

The instantaneous luminosity profile of the zero bias data used for overlay in MC events was found to be different from the luminosity profile of the data sample. For the data set used in this analysis the average instantaneous luminosity was $40 \cdot 10^{30} \text{ cm}^{-2}\text{s}^{-1}$, while in MC the average was $29 \cdot 10^{30} \text{ cm}^{-2}\text{s}^{-1}$. Since the tau identification, as well as the efficiency of the muon isolation requirement were found to be dependent on the instantaneous luminosity, each MC event was given a weight equal to the ratio of data to MC normalized numbers of events in the bin of instantaneous luminosity of the zero bias event used as overlay in that particular MC event. Figure 6.7 shows the two normalized luminosity profiles and their ratio which was used to reweight each MC event.

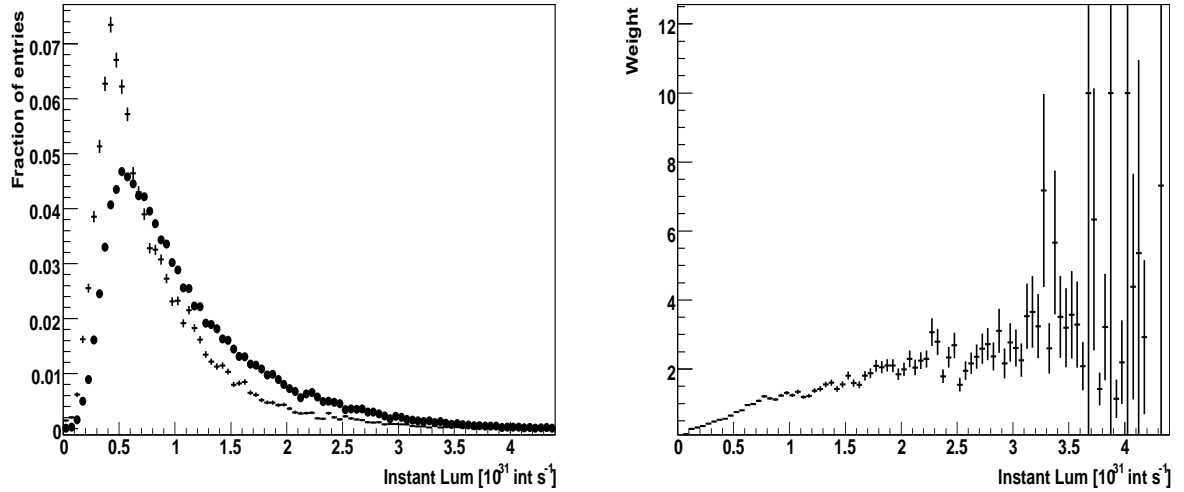


Figure 6.7. *Instantaneous luminosity reweighting: the instantaneous luminosity profiles for data, shown in bold dots, and MC (left) and the weight factors applied to the simulated events as a function of instantaneous luminosity of the underlying event (right)*

6.3.3 Beam shape correction

The tracking efficiency has a strong dependence on the z of the primary vertex. In MC this distribution was simulated using a Gaussian with a width of 25 cm, which was shown [83] to be a rather crude approximation of the distribution measured in data, which is wider and therefore leading to more events falling outside the z acceptance of the tracking system. To correct for this, the MC events were weighted such that the acceptance reproduces the one in data, using the procedure described in [83].

6.3.4 Muon efficiency corrections

The efficiencies for a muon to be reconstructed both in data and MC were calculated using the tag and probe method applied to $Z \rightarrow \mu^+\mu^-$ events. The requirements were the same to those used for the calculation of trigger efficiency, except with the quality of the track probe, which was chosen to be “medium” instead of “loose”. A complete description of the method and the results can be found in [59]. Efficiency correction factors for MC events as a function of different muon position parameters were obtained by dividing the efficiency for data in that particular region of the detector with the one obtained for MC. Both the efficiency to find a loose muon and the efficiency of matching a loose muon to a medium track were corrected using this method. In the first case the correction factors were obtained as a function of detector η and ϕ at the muon system. The average value of the correction was 99.2 %. In the second case the efficiencies were parametrized as a function of the detector η at the CFT and the z of the track, resulting in an average correction factor of 93.1 %. The average efficiencies of finding an isolated muon were studied both in data and MC as a function of the number of jets with transverse momenta greater than 15 GeV, muon p_T , number of vertices and ΔR between the muon and the closest jet and found to be essentially identical, therefore no correction related to the isolation cut efficiency was applied in this analysis.

6.3.5 Tracking efficiency correction for tau candidates

The efficiency for tracks to have at least one SMT hit is known to be higher in MC than in data. To account for this, a similar method to the one used for correcting the muon efficiencies in MC was applied. The probability that a track has at least one SMT hit was measured as a function of the detector η at the CFT and the z coordinate of the track, for both $Z \rightarrow \mu^+\mu^-$ MC and data events. The ratio of data efficiency divided by MC efficiency obtained as a function of the above mentioned parameters was applied to each MC event as a weight, with an average value of 98.1 %. Also, reconstructing a second track close to a first reconstructed track was found to be more efficient in MC compared to data. A correction factor of 0.97 ± 0.028 , obtained by comparing the number of type 3 tau candidates with 2 and 3 tracks in data and MC, was applied as a weight to the simulated events containing type 3 tau candidates.

6.3.6 Vertex efficiency correction

The efficiency for vertex reconstruction was found to be slightly lower in data compared to the Monte Carlo, even after the corrections related to the beam shape were applied [85]. A correction factor of 0.993 ± 0.002 was applied to account for this effect.

6.4 Event selection

At preselection level, each event had to fulfill the following requirements:

- one loose muon matched to a central track of medium quality with $p_T > 15$ GeV and $|\eta_{\text{det}}| < 1.6$;
- no other loose muon matched to a central track with $p_T > 10$ GeV in the event;
- the tagged muon had to be tightly isolated: the sum of energies of all cells situated in a hollow cone around the direction of the muon with $0.1 < R < 0.4$, as well as the sum of all tracks in a cone of $R < 0.5$, excluding the muon track, had to be less than 2.5 GeV;
- one tau candidate with $NN > 0.3$ and corrected $p_T > 15$ GeV;
- the sum of the transverse momenta of all tracks associated to the tau candidate had to be > 15 GeV for type 1 and 3 and > 5 GeV for type 2 tau candidates;
- at least 1 SMT hit on at least one of the tracks associated with the tau candidate;
- type 3 tau candidates with 2 tracks are only considered if both tracks have the same charge;
- the tau candidate must have a charge opposite to that of the muon;
- the distances in the z direction between the muon and the primary vertex, the tau candidate and the primary vertex, as well as the distance between the muon and the tau candidate had to be less than 1 cm;
- no other loose muon matching the tau candidate;
- one single muon trigger per trigger list must have fired (see Table 6.1).

In total 8316 events passed these criteria. It is expected that the $b\bar{b}$ production (QCD background) as well as the events where a W boson was produced in association with one or more jets contribute to this sample in approximately the same measure as the $Z \rightarrow \tau^+\tau^-$ signal. In order to reduce the $W + \text{jets}$ background, an upper limit on a variable which gives an approximation of the W mass, called M_W , was used:

$$M_W = \sqrt{2E^\nu E^\mu (1 - \cos\Delta\phi)}, \quad (6.1)$$

where E^ν is an approximation of the neutrino energy calculated using the transverse momentum of the muon p_T^μ , the energy of the muon E^μ and the missing transverse energy \cancel{E}_T , given by:

$$E^\nu = \cancel{E}_T E^\mu / p_T^\mu \quad (6.2)$$

and $\Delta\phi$ is the angle between the missing E_T and the muon in the $r\phi$ plane.

For the final selection the lower limit on the NN output for the tau candidates was raised to 0.9 for types 1 and 2, and to 0.95 for type 3 tau candidates. The final selection also required $M_W < 20$ GeV. A total of 1511 events passed all the selection criteria in the data sample.

6.5 Background

The dominant background is from multijet (QCD) processes, mainly from $b\bar{b}$ events where the muon isolation requirement is met and a jet satisfies the tau candidate selection criteria. Another significant source of events with isolated muons and tau candidates from misidentified jets is the W + jets production, where the W boson decays into a muon and a neutrino. The $Z \rightarrow \mu^+\mu^-$ background is reduced due to the requirement that no other loose muon should be found in the event. However, a small number of events will pass this requirement, due to the fact that one of the muons is not identified as a muon. Small contributions are also expected from $W \rightarrow \tau\nu$ and $WW \rightarrow l\nu l\nu$, as well as $t\bar{t}$ production. The contributions from WZ and ZZ events were estimated to yield below one event each after the final cuts and were therefore considered negligible in this analysis. All backgrounds, except the QCD one, were estimated using MC simulations.

6.5.1 QCD background

The QCD background is estimated using the events that fulfill all requirements for the final signal sample selection, except that the muon and the tau candidate have the same charge. We will call this the same sign (SS) sample.

To test the assumption that the number of SS events is equal to the number of opposite sign (OS) background events, a special data sample was selected, named “QCD sample” from here on, in which the events passed all other requirements placed on the signal sample, but failed the muon isolation criteria and the requirement on the tau NN output. More precisely, the new requirements were that the sum of energies of all cells situated in a cone around the direction of the muon with $R < 0.4$, but outside a cone around the same direction with $R < 0.1$, had to be greater than 2.5 GeV but less than 10 GeV, and the sum of the momenta of all tracks in a cone of $R < 0.5$, excluding the muon track, had to be in the same interval (2.5 – 10 GeV) as well. To avoid the contribution from $Z \rightarrow \tau^+\tau^-$ signal events, an upper limit on the tau NN output was

placed at 0.8. The limit on the muon p_T was lowered to 10 GeV to increase the number of events in the sample.

This is a sample that is expected to be completely dominated by multijet processes, but may also include events in which a W decaying into a muon was produced in association with a jet. The W+jet contribution was reduced by placing a limit on the azimuthal angle ϕ between the muon and the tau and requiring that they are back to back ($\phi > 2.5$ radians).

A slight excess of OS events was observed in the QCD sample. This excess was studied as a function of tau type, tau candidate p_T and NN output. Figure 6.8 shows the OS/SS ratio as a function of p_T and NN output for the three types of tau candidates in the QCD sample. No significant dependence on p_T or tau NN output was observed. Correction factors $f_{\text{QCD}}^1 = 1.13 \pm 0.031$, $f_{\text{QCD}}^2 = 1.08 \pm 0.011$ and $f_{\text{QCD}}^3 = 1.06 \pm 0.007$ for each tau type were obtained. Finally, the number of events in the SS sample is corrected for the contribution from $Z \rightarrow \mu^+\mu^-$, $Z \rightarrow \tau^+\tau^-$ and $W \rightarrow \tau\nu$ obtained from MC, with a total of 3 events for type 1, 8 for type 2 and 12 for type 3 tau candidates after all cuts. To account for the higher probability for charge misidentification in data, a factor of 2 was applied to the contribution from $Z \rightarrow \mu\mu$ and $Z \rightarrow \tau\tau$, obtained from [84]. The more substantial contribution from $W \rightarrow \mu\nu$ events is accounted for separately.

6.5.2 W + jets background

A part of the W + jets background has already been included in the SS sample which is used as an estimation of the QCD background. However, we do expect a significant excess of OS events compared to the number of SS events due to fact that a high percentage of W + 1 jet events come from quark jets. One can estimate the number of W + jets events in data by selecting a sample that is expected to have a large contribution from that channel and low or negligible contributions from Z boson production. Such a W + jets enriched sample can be obtained by requiring an isolated muon with $p_T > 20$ GeV, a tau with $0.3 < NN < 0.8$, $|\phi_\mu - \phi_\tau| < 2.7$ and $M_W > 40$ GeV. We can expect that mostly QCD and W + jets events will contribute to this sample. Table 6.3 shows the number of events expected when using these requirements for the W + jets $\rightarrow \mu\nu$ + jets MC for each tau type. as well as the numbers observed in the W + jets data sample. We use the fact that for QCD events we expect an excess of OS events compared to SS of f_{QCD}^i , as obtained in the previous section. The factors $f_W^1 = 2.39$, $f_W^2 = 3.15$ and $f_W^3 = 1.6$ for the W + jets background were estimated from data, in the sample with the cuts listed above, but requiring a tighter cut on M_W , namely $M_W > 60$ GeV. Given this, we can calculate the number of W + jets events in the W + jets enriched data sample by solving the following system of two equations, separately for each tau type i :

$$N_W^i + N_{\text{QCD}}^i = N_{\text{OS}}^i + N_{\text{SS}}^i, \quad (6.3)$$

$$\frac{f_W^i - 1}{f_W^i + 1} N_W^i + \frac{f_{\text{QCD}}^i - 1}{f_{\text{QCD}}^i + 1} N_{\text{QCD}}^i = N_{\text{OS}}^i - N_{\text{SS}}^i. \quad (6.4)$$

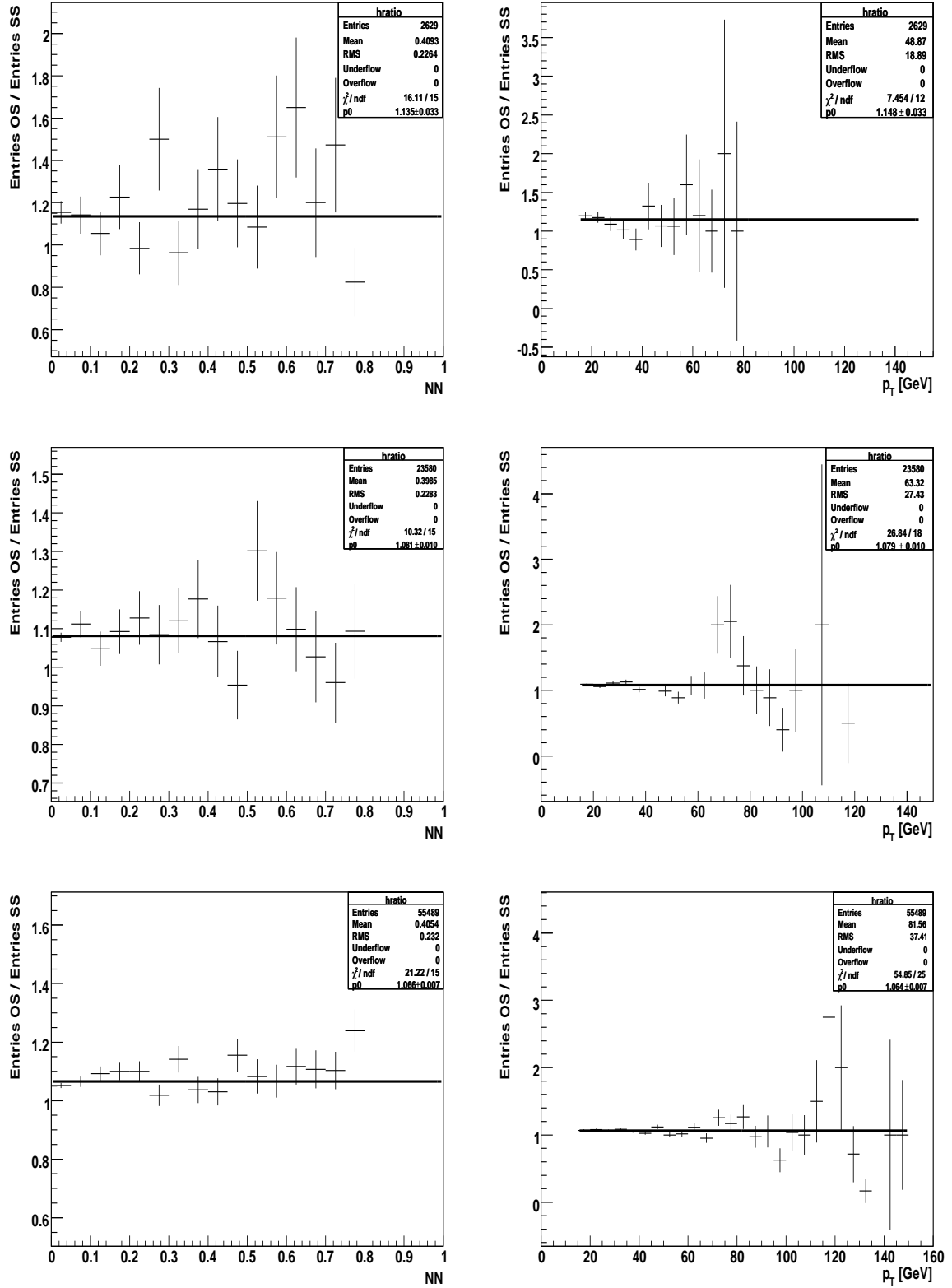


Figure 6.8. The OS/SS ratio as a function of NN output and p_T for the three types of tau candidates in the QCD sample: type 1 (top), type 2 (middle) and type 3 (bottom).

The ratio between the number of events in data calculated from these equations and the number of events estimated from MC for each tau type was used as a normalization factor for this background in the signal region. The estimated additional contributions to the data sample from $W \rightarrow \tau\nu$, WW , $Z \rightarrow \mu\mu$ events and from $Z \rightarrow \tau\tau$ events, with a total of $(18 \pm 9) \%$ for type 1, $(26 \pm 13) \%$ for type 2 and $(11 \pm 5) \%$ for type 3, were also taken into account when calculating the normalization factors. The normalization factors obtained were 0.97 for type 1, 0.89 for type 2 and 0.77 for type 3.

Sample	Type 1	Type 2	Type 3
MC	58 - 21	330 - 88	1132 - 587
Data	69 - 31	393 - 125	975 - 618

Table 6.3. *Numbers of OS and SS events (written as OS - SS) in data and in the $W \rightarrow \mu\nu$ MC, obtained running with the requirements for the W enriched sample in data.*

The uncertainties on the normalization factors discussed above, as well as on the charge correlation estimated from data (and possibly influenced by the presence of QCD, $Z \rightarrow \mu\mu$ and $Z \rightarrow \tau\tau$ events in the $W + \text{jets}$ sample), combined with the statistical uncertainties of the $W + \text{jets}$ samples from data and MC are taken as a systematic uncertainty on this background. Their total values are 23 % for type 1, 28 % for type 2 and 19 % for type 3. The estimated number of $W + \text{jets}$ events in the signal sample, not considering the ones already included in the SS sample, is 14 ± 5 (after all cuts).

6.6 Charge mis-identification correction

It is estimated from MC that a fraction of $5.3 \cdot 10^{-3}$ of all $Z \rightarrow \tau^+\tau^-$ events will get a wrong sign for either the muon or the tau candidate, therefore appearing as SS events. From the number of $Z \rightarrow \tau^+\tau^-$ events obtained from subtracting the estimated background from the number of events in the final sample, we calculate that the number of $Z \rightarrow \tau^+\tau^-$ events reconstructed as SS is 8.3.

The fraction of events in which one of the leptons has an incorrectly identified charge is significantly higher in data than in Monte Carlo. A correction factor of 2_{-1}^{+2} [84] which takes into account this effect was applied to the number of simulated events with mis-identified charge. Therefore we estimate that 17 events should be added to the number of events in the OS sample when calculating the $Z \rightarrow \tau^+\tau^-$ cross section, as a second order correction.

6.7 Estimating the $Z \rightarrow \tau^+\tau^-$ signal

In this section we show a comparison of several distributions measured in data to the sum of all backgrounds added to a $Z \rightarrow \tau^+\tau^-$ signal normalized with the Standard Model NNLO cross section from [93–95]. The comparison was made at three successive selection levels: preselection, preselection and requiring NN output to be greater than 0.9 for types 1 and 2 and greater than 0.95 for type 3, and finally after all selection requirements were applied, by also requesting $M_W < 20$ GeV. It is worth noting that while most processes estimated to contribute to these distributions are illustrated on their own, the multijet QCD background is shown together with the fraction of $W \rightarrow \mu\nu + \text{jets}$ events which falls into the same sign (SS) data sample. The SS distributions are multiplied with the factors f_i , which are f_{QCD}^i corrected for the contribution of $Z \rightarrow \tau^+\tau^-$, $Z \rightarrow \mu^+\mu^-$ and $W \rightarrow \tau\nu$ events to the SS sample. Therefore the illustrated $W \rightarrow \mu\nu + \text{jets}$ contribution shows in fact only the estimated excess of this background in the opposite sign (OS) sample, as opposed to the whole contribution.

Figure 6.9 shows the muon η_{det} , ϕ and p_T distributions at preselection level, while Fig. 6.10 and 6.11 show the tau candidate η , NN output and p_T distributions, as well as the \cancel{E}_T distributions for each tau type at preselection level. Figures 6.12 and 6.13 show the M_W and visible mass distributions at preselection level, where the visible mass is defined as:

$$\text{Visible Mass} = \sqrt{(P_\mu + P_\tau + \cancel{P}_T)^2}, \quad (6.5)$$

with $P_{\mu,\tau} = (E_{\mu,\tau}, P_{\mu,\tau}^x, P_{\mu,\tau}^y, P_{\mu,\tau}^z)$ and $\cancel{P}_T = (\cancel{E}_T, \cancel{E}_T^x, \cancel{E}_T^y, 0)$. The metric used for the four-vector product is $(1, -1, -1, -1)$.

Figures 6.14 and 6.17 illustrate several same control distributions after requiring $\text{NN} > 0.9$ (0.95 for type 3 tau candidates) and after all selection criteria were applied, respectively: muon detector η , ϕ and p_T , tau candidate p_T and η , as well as the \cancel{E}_T distribution, for the sum of all tau types. Figures 6.15 and 6.16 show the M_W and the visible mass distributions after requiring $\text{NN} > 0.9$ (0.95 for type 3 tau candidates). Figure 6.18 illustrates the visible mass distributions for each tau type and for the sum of all types after all selection requirements were placed on the events on linear scale, while Fig. 6.19 shows the visible mass distribution on logarithmic scale for all events in the selected sample. Finally, the number of events for each tau-type and the contribution to type 3 taus from 2- and 3-prongs for each of the selection levels mentioned above are shown in Fig. 6.20. Good agreement is observed between data and the sum of MC signal and background in all of these distributions.

Table 6.4 shows the number of events expected from each of the backgrounds, as well as from $Z \rightarrow \tau^+\tau^-$ signal normalized to the NNLO cross section from [93–95]. It also shows the total number of expected background and signal events in comparison to the number of events observed in data, for the three levels of selection mentioned above: preselection, preselection + NN output > 0.9 (0.95 for type 3 tau candidates) and after all selection criteria were applied. Tables 6.5, 6.6 and 6.7 show the same numbers for each of the three types.

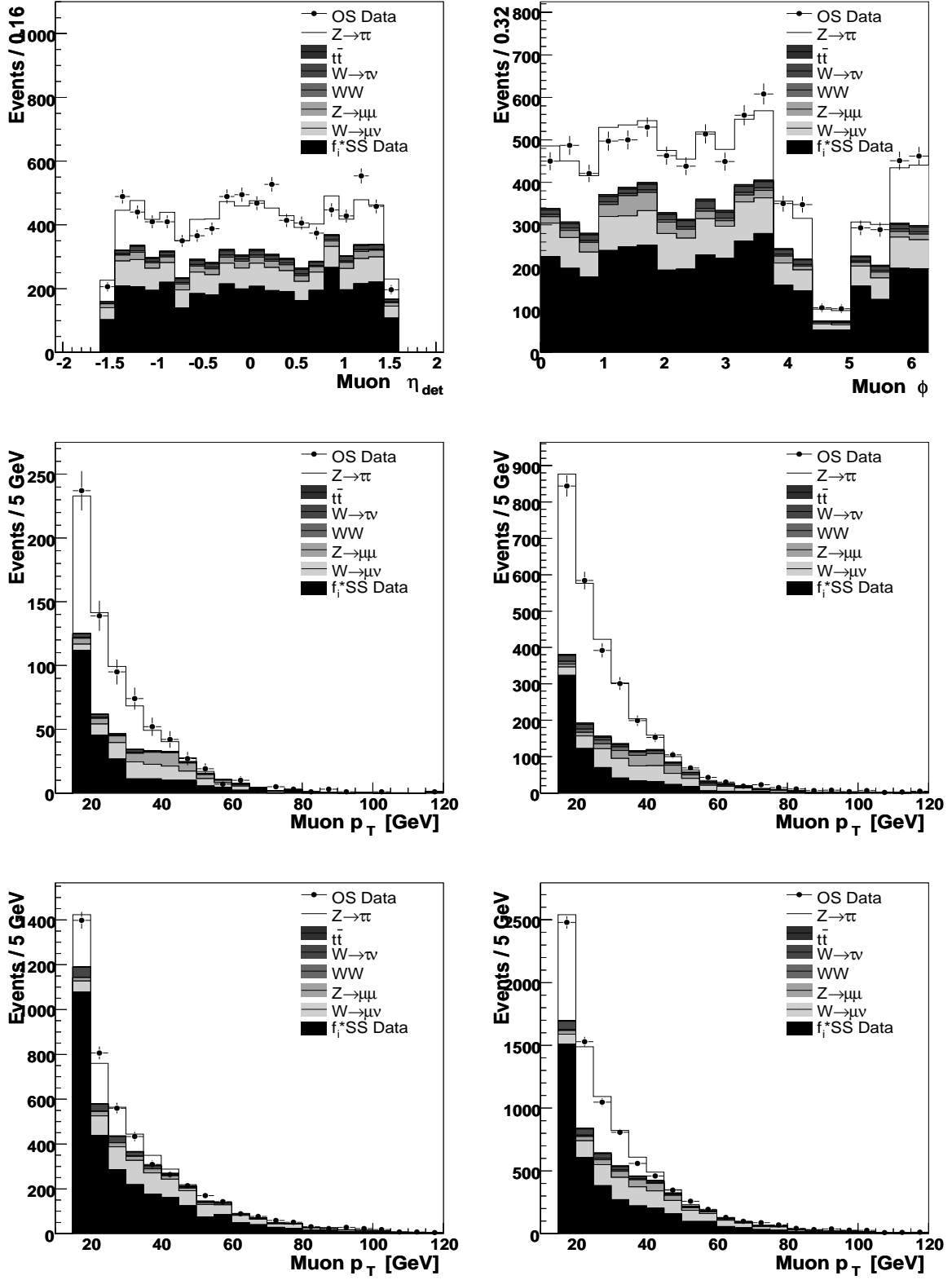


Figure 6.9. Muon distributions at preselection level: detector η (upper left), ϕ (upper right) and p_T when the tau candidate in the muon-tau lepton pair is of type 1 (middle left), type 2 (middle right), type 3 (lower left) or any type (lower right).

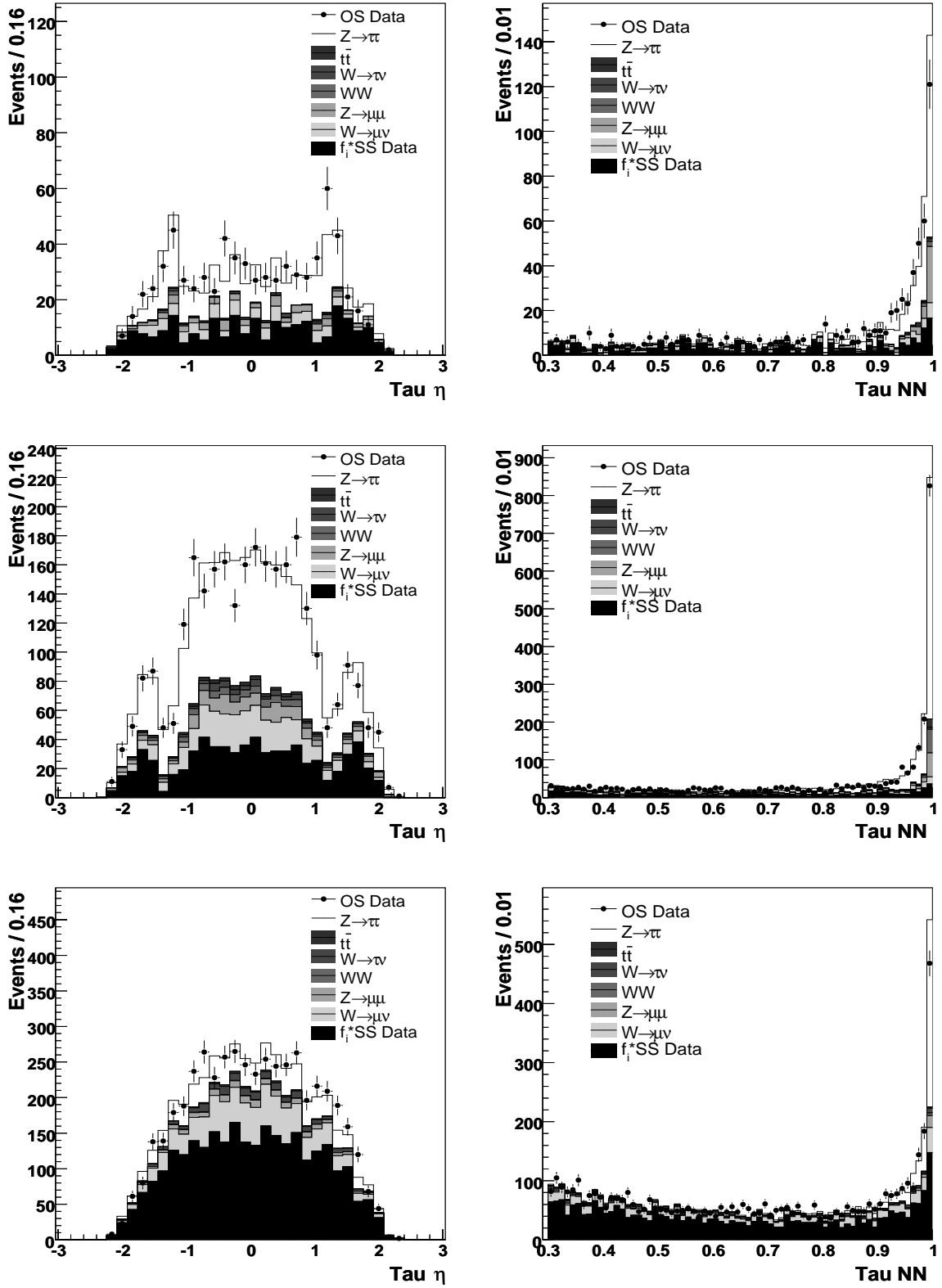


Figure 6.10. Tau candidate η (left) and NN output (right) distributions at preselection level, when the tau candidate is of type 1 (upper row), type 2 (middle row) and type 3 (lower row).

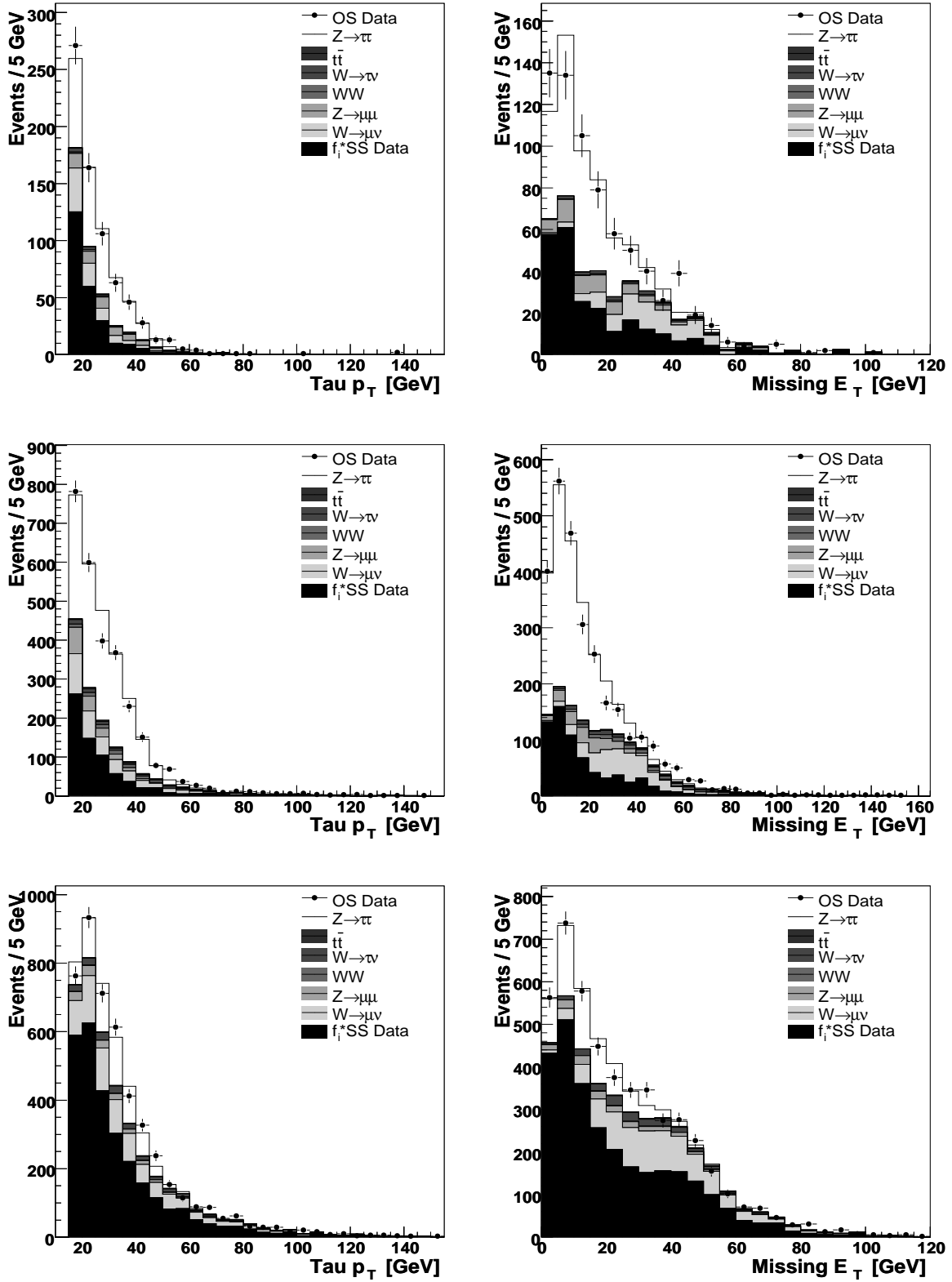


Figure 6.11. Tau candidate p_T (left) and missing E_T (right) distributions at preselection level, when the tau candidate in the muon-tau lepton pair is of type 1 (upper row), type 2 (middle row), type 3 (lower row)

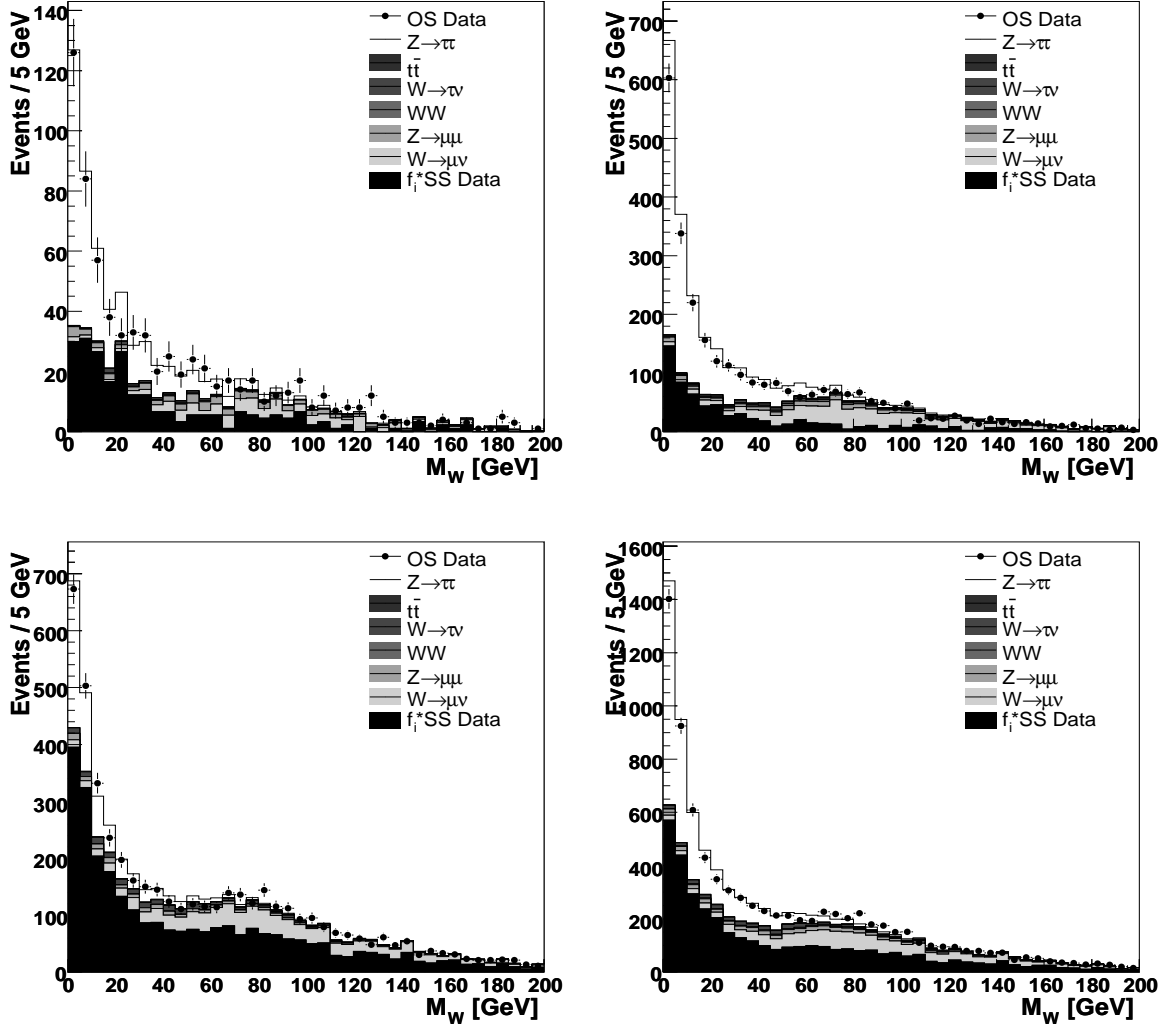


Figure 6.12. Distributions of the M_W variable at preselection level, when the tau candidate in the muon-tau lepton pair is of type 1 (upper left), type 2 (upper right), type 3 (lower left) or any type (lower right).

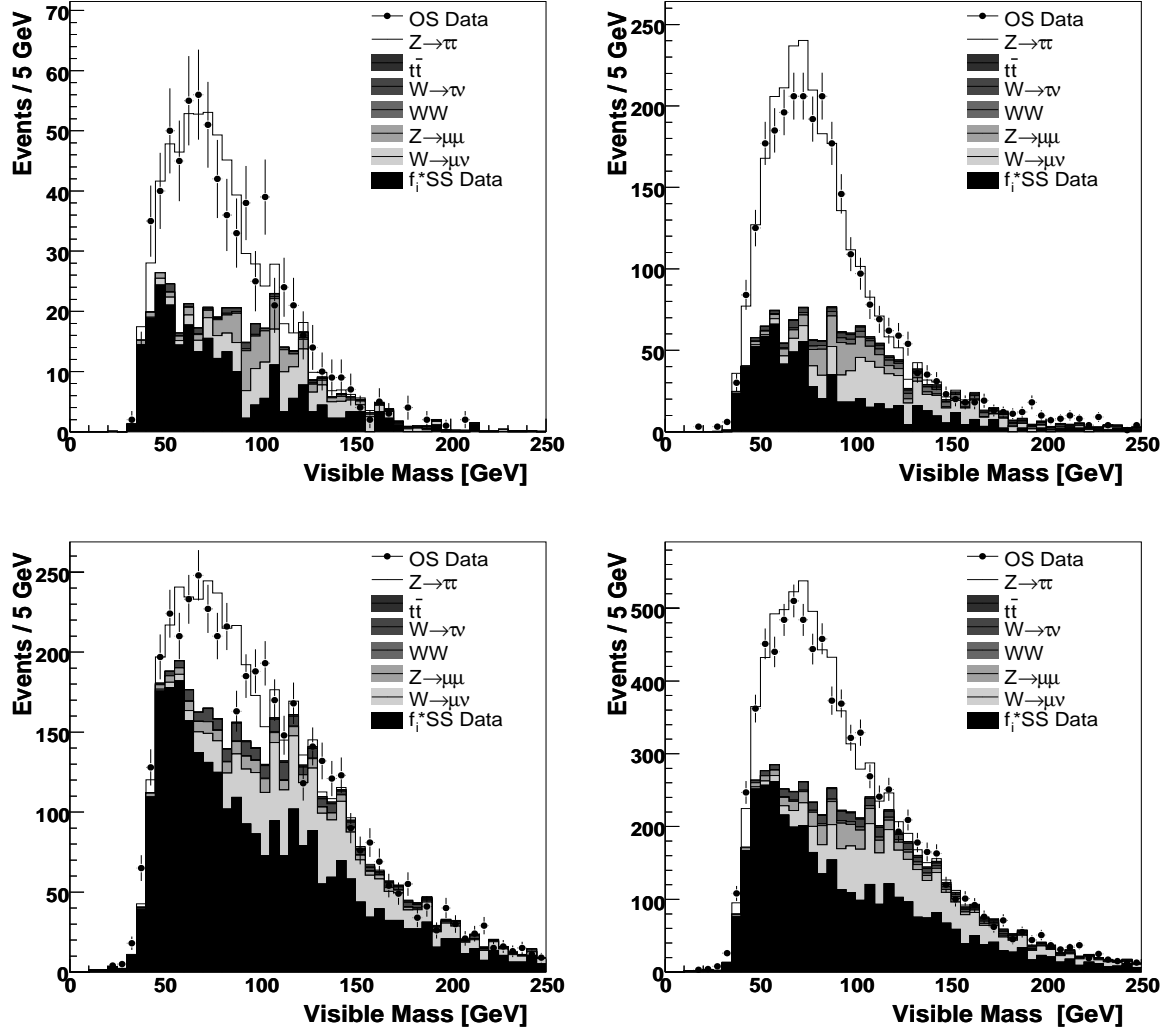


Figure 6.13. Visible mass distributions at preselection level, when the tau candidate in the muon-tau lepton pair is of type 1 (upper left), type 2 (upper right), type 3 (lower left) or any type (lower right).

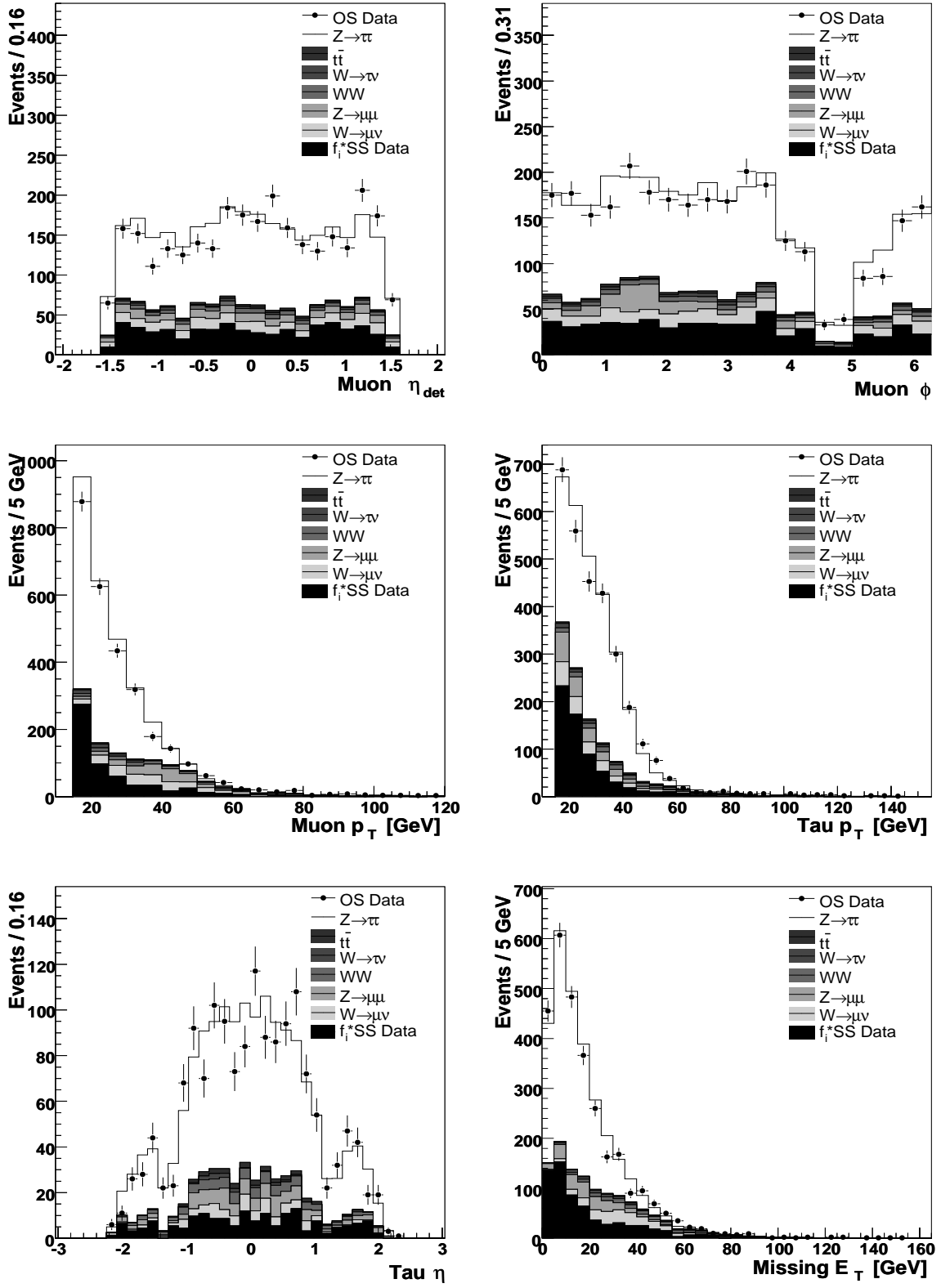


Figure 6.14. Control distributions after the $NN > 0.9$ cut: muon detector η (upper left), ϕ (upper right) and p_T (middle left), tau candidate p_T (middle right) and η (lower left); the \cancel{E}_T distribution is also shown (lower right).

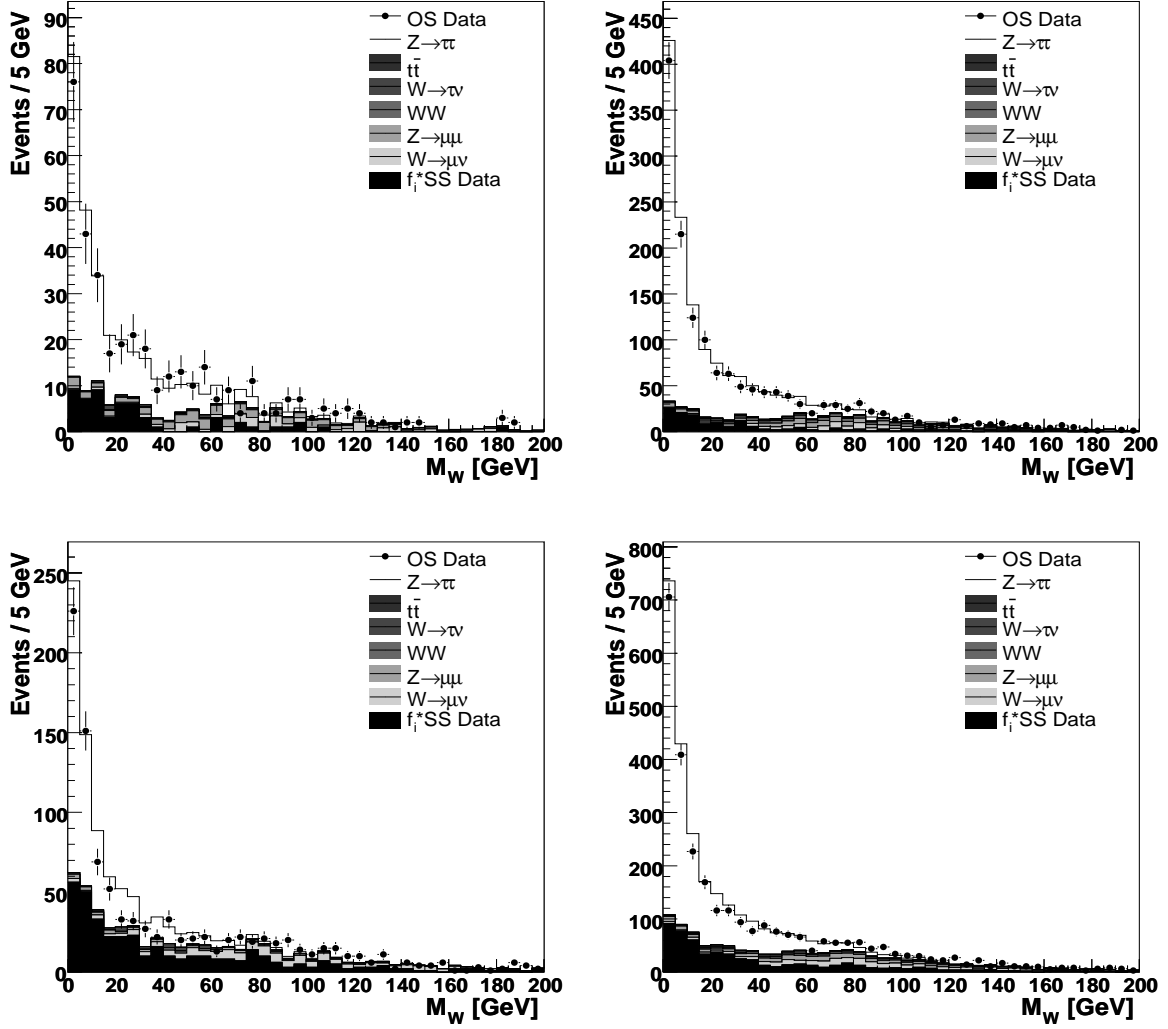


Figure 6.15. Distributions of the M_W variable after the $NN > 0.9$ cut, when the tau candidate in the muon-tau lepton pair is of type 1 (upper left), type 2 (upper right), type 3 (lower left) or any type (lower right).

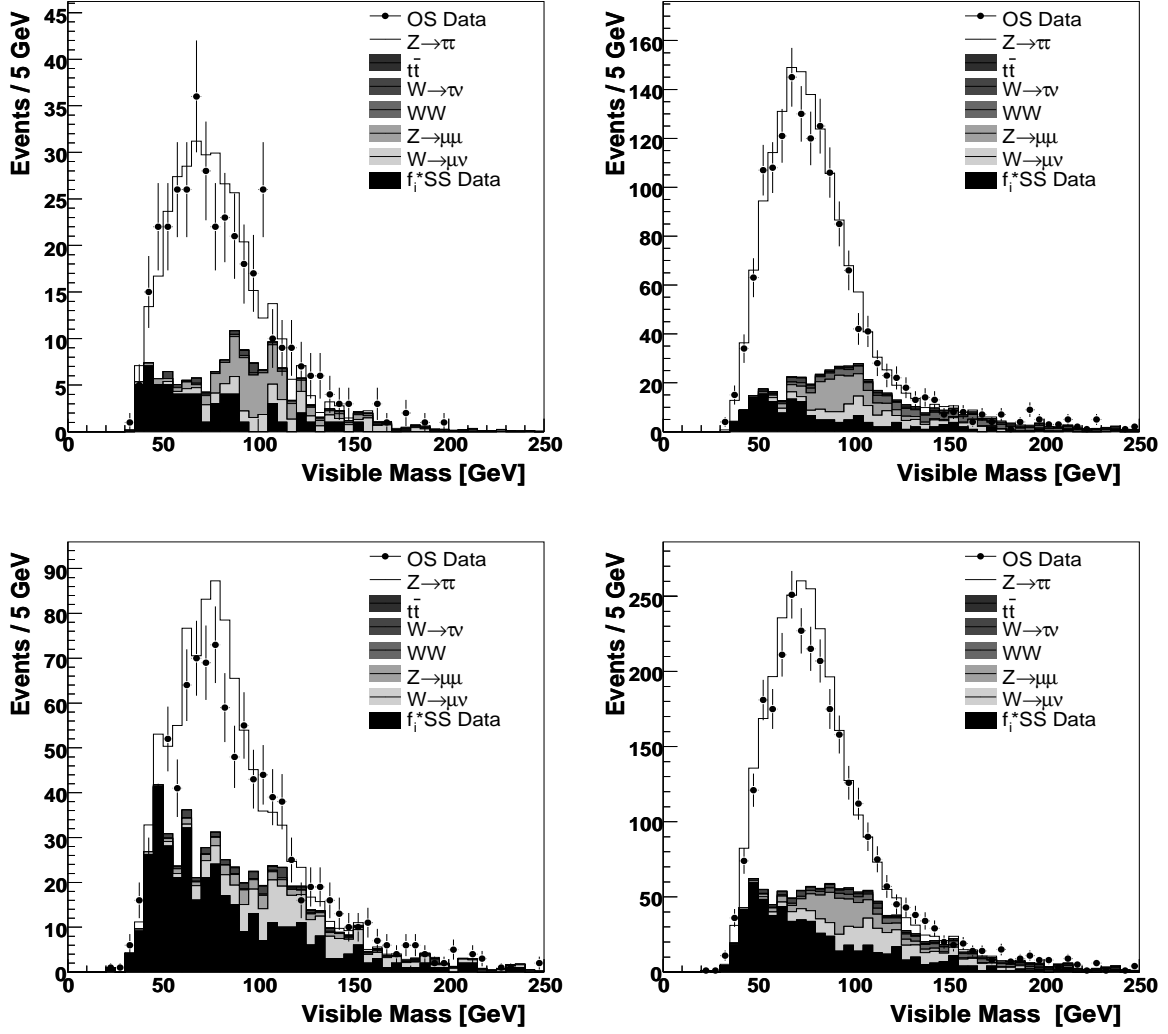


Figure 6.16. Visible mass distributions after the $NN > 0.9$ cut, when the tau candidate in the muon-tau lepton pair is of type 1 (upper left), type 2 (upper right), type 3 (lower left) or any type (lower right).

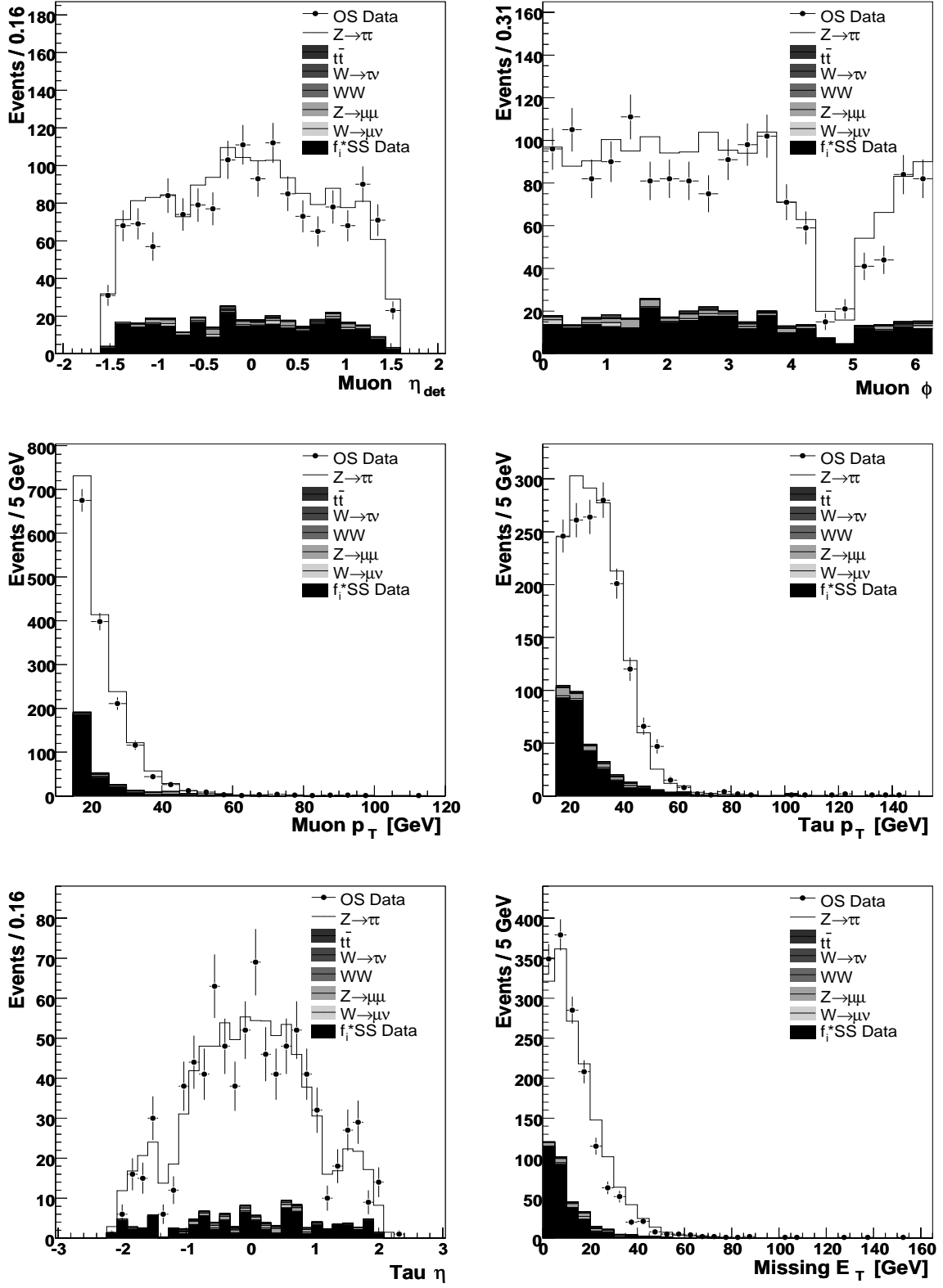


Figure 6.17. Control distributions after all cuts: muon detector η (upper left), ϕ (upper right) and p_T (middle left), tau candidate p_T (middle right) and η (lower left); the \cancel{E}_T distribution is also shown (lower right).

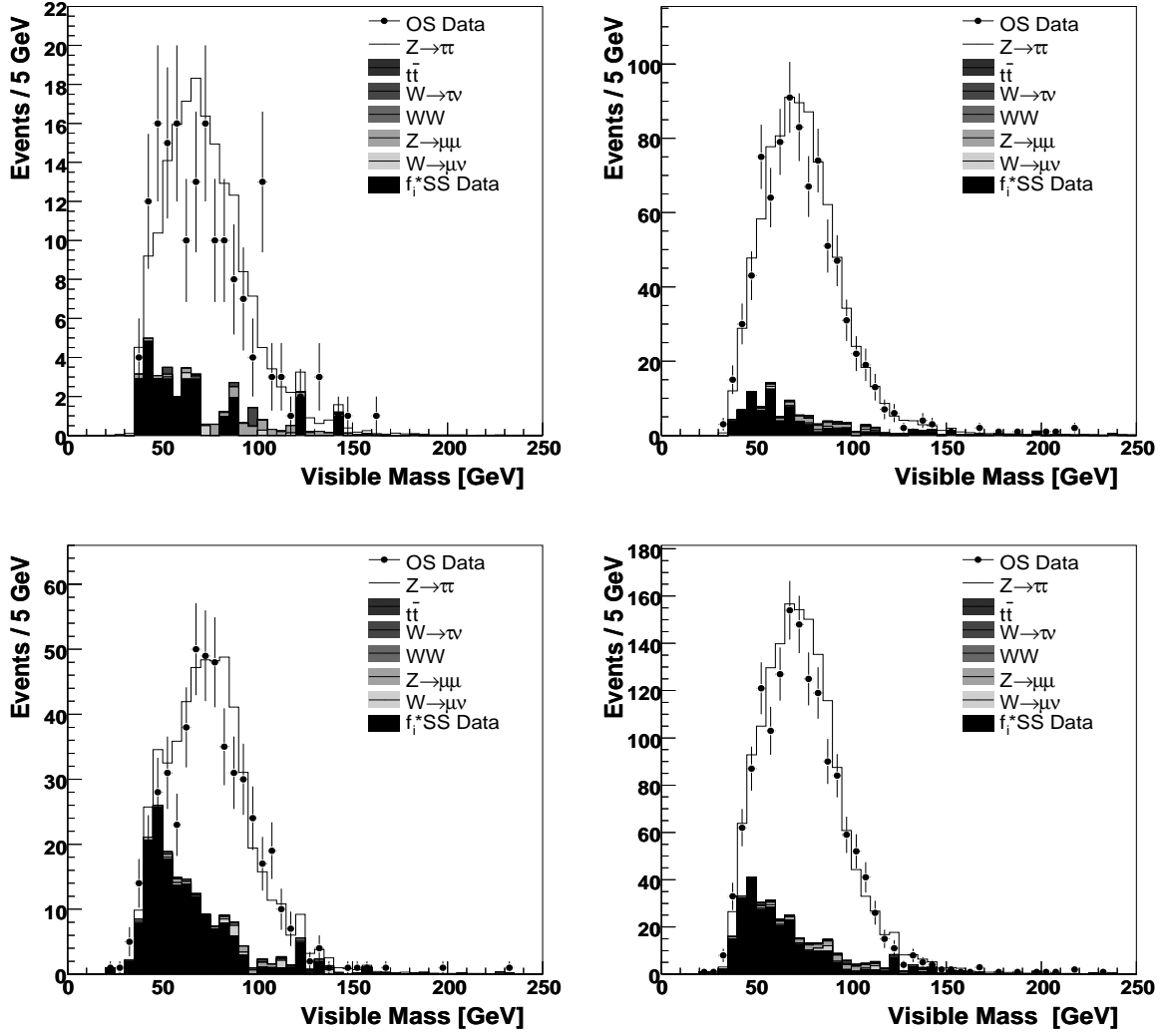


Figure 6.18. Visible mass distributions after all cuts, when the tau candidate in the muon-tau lepton pair is of type 1 (upper left), type 2 (upper right), type 3 (lower left) or any type (lower right).

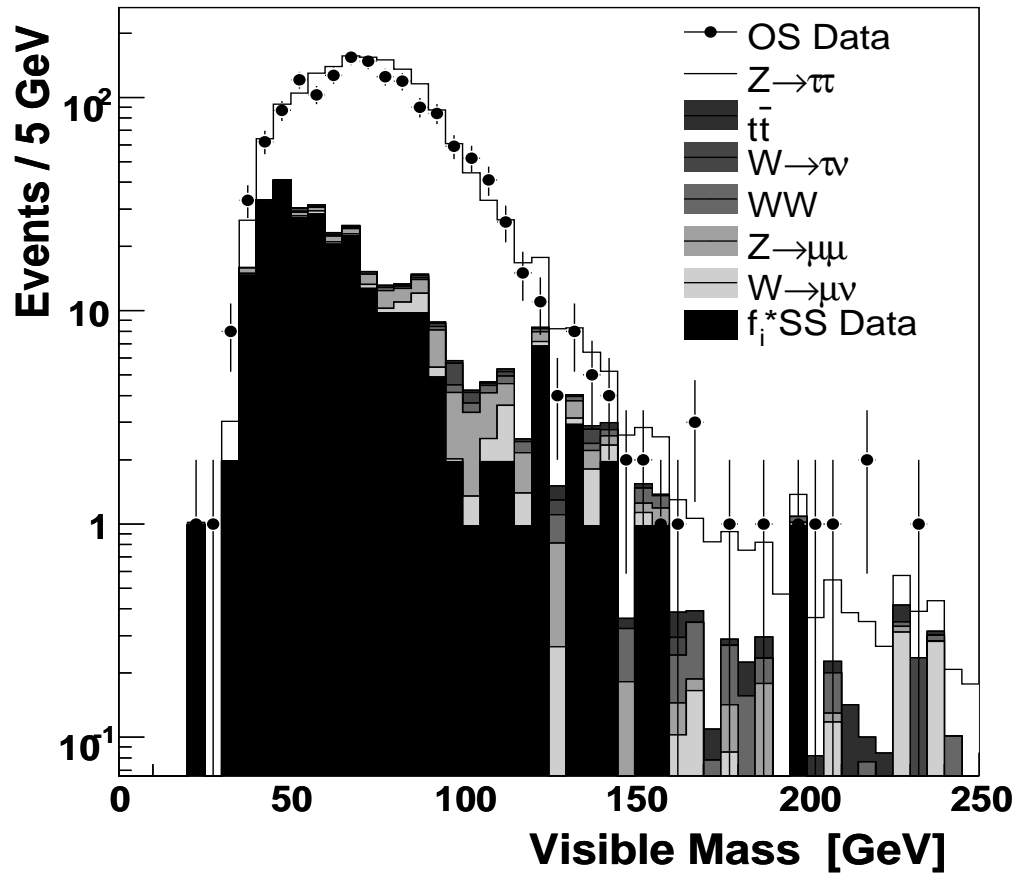


Figure 6.19. Visible mass distribution after all cuts, on logarithmic scale, for the sum of all tau types.

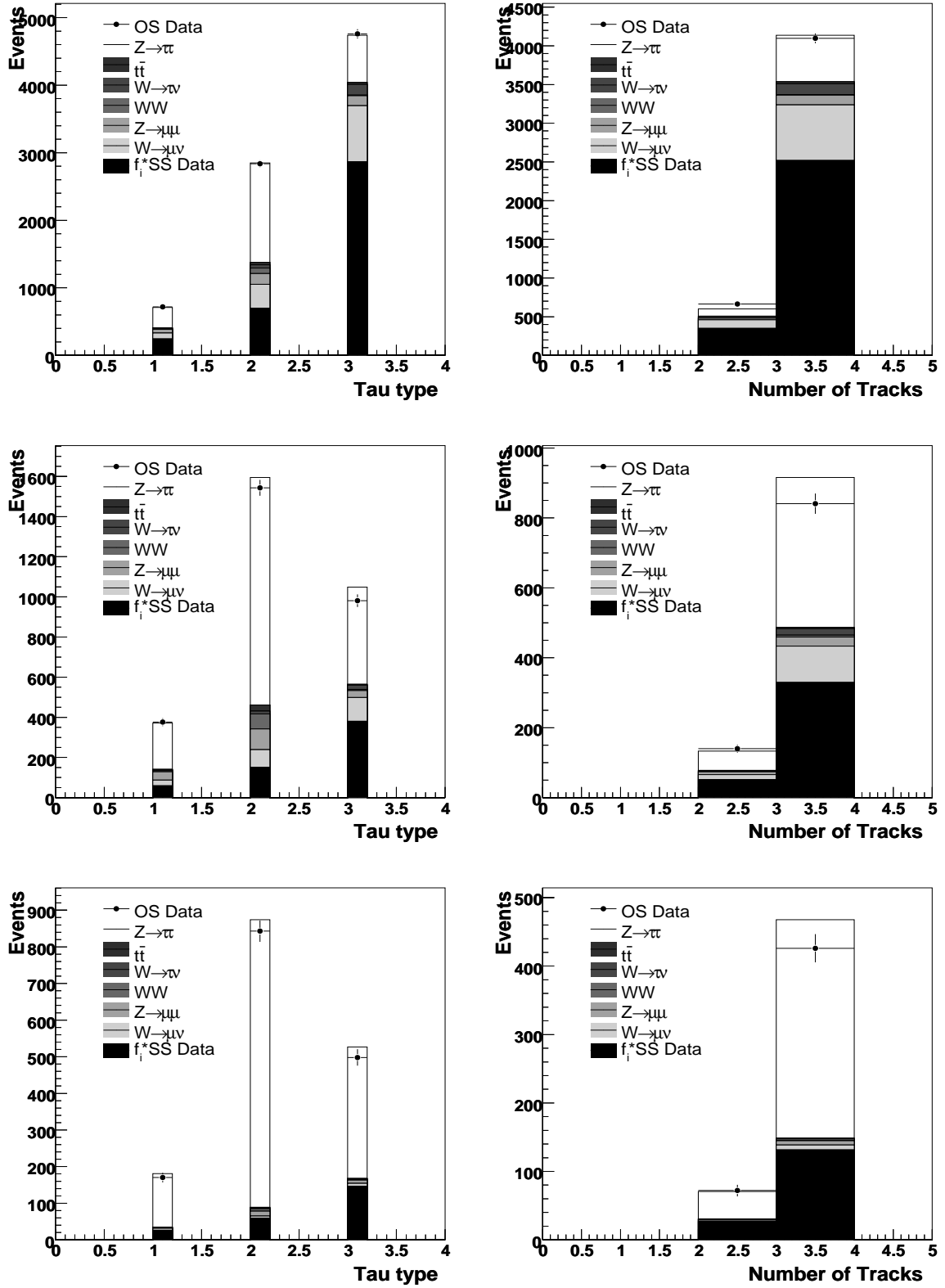


Figure 6.20. Number of events for each tau-type (left) and number of tracks associated to the tagged type 3 tau candidates (right), at preselection level (upper row), after NN > 0.9 cut (middle row) and after all cuts (lower row).

Process	Preselection	Presel + NN > 0.9 (0.95-type3)	after all cuts
$Z \rightarrow \tau^+\tau^-$	2464 ± 12	1845 ± 10	1290 ± 8
$t\bar{t}$	65 ± 2	34 ± 1	3.1 ± 0.3
$W \rightarrow \tau\nu$	228 ± 9	40 ± 4	6.6 ± 1.7
WW	95 ± 1	86 ± 1	7.6 ± 0.4
$Z \rightarrow \mu^+\mu^-$	418 ± 5	189 ± 3	29 ± 1.2
$W \rightarrow \mu\nu$	1981 ± 38	360 ± 16	23 ± 3.5
QCD	3057 ± 57	442 ± 23	231 ± 16
Predicted	8308 ± 69	2996 ± 30	1590 ± 18
Data OS - SS	8316 - 3634	2907 - 596	1511 - 265

Table 6.4. Number of events expected for the sum of all tau candidate types from each of the backgrounds, as well as from $Z \rightarrow \tau^+\tau^-$ signal normalized with the NNLO cross section, the sum of background and signal and the number of events observed in data, for the three selection levels mentioned in the text: preselection, preselection + NN output > 0.9 (0.95 for type 3) and after all selection criteria were applied.

Process	Preselection	Presel + NN > 0.9	after all cuts
$Z \rightarrow \tau^+\tau^-$	302 ± 4	230 ± 4	146 ± 3
$t\bar{t}$	2.7 ± 0.3	2 ± 0.3	0.2 ± 0.1
$W \rightarrow \tau\nu$	10 ± 2	4 ± 1	1.5 ± 0.8
WW	7 ± 0.3	6 ± 0.3	0.4 ± 0.1
$Z \rightarrow \mu^+\mu^-$	58 ± 2	43 ± 1.5	6 ± 0.6
$W \rightarrow \mu\nu$	127 ± 11	42 ± 5	2.1 ± 1
QCD	208 ± 15	46 ± 8	25 ± 5.5
Predicted	715 ± 18	373 ± 11	181 ± 7
Data OS - SS	720 - 221	380 - 58	170 - 28

Table 6.5. Type 1 tau candidates: Number of events expected from each of the backgrounds, as well as from $Z \rightarrow \tau^+\tau^-$ signal normalized with the NNLO cross section, the sum of background and signal and the number of events observed in data, for the three selection levels mentioned in the text: preselection, preselection + NN output > 0.9 and after all selection criteria were applied.

Process	Preselection	Presel + NN > 0.9	after all cuts
$Z \rightarrow \tau^+ \tau^-$	1469 ± 9	1131 ± 8	786 ± 7
$t\bar{t}$	33 ± 1	28 ± 1	2.4 ± 0.3
$W \rightarrow \tau \nu$	50 ± 4	14 ± 2.2	1.4 ± 0.7
WW	79 ± 1	74 ± 1	6.9 ± 0.3
$Z \rightarrow \mu^+ \mu^-$	176 ± 3	108 ± 3	14 ± 0.8
$W \rightarrow \mu \nu$	470 ± 18	116 ± 9	6.7 ± 1.9
QCD	584 ± 25	123 ± 12	61 ± 8
Predicted	2861 ± 32	1594 ± 18	878 ± 12
Data OS - SS	2836 - 655	1546 - 159	843 - 76

Table 6.6. Type 2 tau candidates: Number of events expected from each of the backgrounds, as well as from $Z \rightarrow \tau^+ \tau^-$ signal normalized with the NNLO cross section, the sum of background and signal and the number of events observed in data, for the three selection levels mentioned in the text: preselection, preselection + NN output > 0.9 and after all selection criteria were applied.

Process	Preselection	Presel + NN > 0.95	after all cuts
$Z \rightarrow \tau^+ \tau^-$	693 ± 6	484 ± 5	358 ± 5
$t\bar{t}$	29 ± 1	4 ± 0.4	0.5 ± 0.1
$W \rightarrow \tau \nu$	168 ± 7	22 ± 2.7	3.7 ± 1.2
WW	9 ± 0.4	6 ± 0.5	0.5 ± 0.1
$Z \rightarrow \mu^+ \mu^-$	184 ± 3	38 ± 1	9 ± 0.7
$W \rightarrow \mu \nu$	1384 ± 32	202 ± 13	14 ± 2.7
QCD	2265 ± 47	273 ± 18	145 ± 13
Predicted	4732 ± 59	1029 ± 23	531 ± 15
Data OS - SS	4760 - 2758	981 - 379	498 - 161

Table 6.7. Type 3 tau candidates: Number of events expected from each of the backgrounds, as well as from $Z \rightarrow \tau^+ \tau^-$ signal normalized with the NNLO cross section, the sum of background and signal and the number of events observed in data, for the three selection levels mentioned in the text: preselection, preselection + NN output > 0.95 and after all selection criteria were applied.

6.8 Systematic uncertainties

The systematic uncertainty related to tau energy corrections was estimated by scaling the charged pion response used for data by the difference found between the response measured in data and the response obtained using G_{CALOR} on one side as well as the largest difference between the charged pion response obtained using G_{CALOR} and G_{HEISHA} on the other side of the response curve and recalculating the acceptance applying all selection requirements. The value of the uncertainty on the cross section measurement was found to be 1.0 % and was given by the small variations in yield when the charged pion response was varied as described above.

NN systematic uncertainties were calculated using statistical ensembles of events in which each input variable was allowed to fluctuate within the difference observed between the distributions of that particular variable in data and MC. The RMS of the ratio of the number of events passing a certain NN cut to the number of events in the ensembles, called ensemble cut ratio, was taken as a measure of the uncertainty corresponding to a particular variable. The RMS of the ensemble cut ratio distributions obtained by varying each input variable were then summed quadratically and the square root of the sum was taken as the overall systematic uncertainty corresponding to the cut on the NN output. The estimated uncertainties were 4 % for type 1, 1.2 % for type 2 and 4 % for type 3 tau candidates [90].

The uncertainty on tau candidate track reconstruction is taken to be the same as the uncertainty on reconstructing muon tracks with at least one SMT hit, namely 1 % (see [59]). A systematic uncertainty related to the beam shape correction of 1 % was added in quadrature to this value. The uncertainty on the correction factor due to tracking for type 3 taus (0.8 %) is added in quadrature as well, resulting in a total uncertainty related to the tau tracks of 1.6 %.

The systematic uncertainties on background estimates are derived from the errors quoted for each estimate in section 6.5. A systematic uncertainty of 5 % on the QCD background was derived from the statistical uncertainty on the fits from which the f_i factors were obtained, added to the estimated effects on f_i from their possible dependence on NN and also taking into account a possible contribution from W+jets production to the QCD sample, which would result in a slight increase of the f_i factors. This results in a systematic uncertainty on the cross section of 0.7 %, for the sum of all types. When added in quadrature to the statistical uncertainty (1.4 %), the total uncertainty on the cross section measurement due to the QCD background becomes 1.6 %. The systematic uncertainties of 23 % for type 1, 28 % for type 2 and 19 % for type 3 on the W + jets background were derived in section 6.5.

The systematic uncertainty due to the charge misidentification is 1 %. This uncertainty was chosen to cover the range between 1 and 4 for the multiplicative factor applied to the number of events which ended up in the SS sample for the $Z \rightarrow \tau\tau$ and $Z \rightarrow \mu\mu$. This multiplicative factor is meant as a MC correction, since it was observed that the charged misidentification happens more often in data than in MC.

The uncertainty on trigger efficiency was calculated by the Muon Id group (see [59]) taking into account a variety of effects such as the tag and probe bias, the variation with an additional cut and background contamination, missing Level 3 information for a small fraction of the events, variations in time or due to increasing luminosity, the choice of binning and the choice of parameters, the CTT data quality and the limited statistics. The estimated values were 1.4 % for the triggers before the v13 trigger list and 4.8 % for the MUH1_TK12_TLM12 trigger. However, a large part of the uncertainty for the MUH1_TK12_TLM12 trigger (3.5 %) was due to the unknown effect of the CTT data quality on the trigger efficiency. Since a correction factor is applied in this analysis to account for that effect, a lower systematic uncertainty of 1.8 % is quoted here. Another significant part of the systematic uncertainty for this trigger was due to the beam shape effect, which is a shift rather than a systematic uncertainty. Since this was corrected for in the analysis and a separate uncertainty of 1 % accounts for any residual effects after the correction, this term can be dropped. With this, the systematic uncertainty for the MUH1_TK12_TLM12 trigger becomes 3.3 %. Finally, a systematic uncertainty of 1 % was added to both triggers to account for the overall L3 trigger efficiency correction of 2 %, which took into account the increase of the L3 track trigger efficiency due to the tau candidate tracks. With this, the trigger uncertainties become 1.7 % for the triggers before the v13 trigger list and 3.4 % for the MUH1_TK12_TLM12 trigger. Therefore, the overall uncertainty on the trigger efficiency is 2.7 %.

The systematic uncertainties on muon identification (0.4 %) and muon track matching (0.8 %) were also taken from [59]. An uncertainty due to muon smearing of 0.4 % was obtained by running without the muon smearing. This value is also consistent with the value obtained in [86]. A systematic uncertainty of 0.2 % from [85] was associated to the vertex reconstruction efficiency.

The efficiency of selecting events without recognizable noise patterns in the calorimeter (“CAL flag efficiency”) was measured for two subsets of the data. The results obtained were 95.4 % and 95.8 % respectively. An efficiency of 97.1 % was found in [87], while in [86] this efficiency was estimated as 96.5 %. A value of 96.1 % was chosen in this analysis, with a 1 % systematic uncertainty which covers the whole range of measured efficiencies listed above. A systematic uncertainty of 0.6 % was calculated to be due to the available MC statistics for all MC samples used in this analysis. The systematic uncertainty due to the $Z \rightarrow \tau^+\tau^-$ cross sections used to estimate the number of $Z \rightarrow \tau^+\tau^-$ events coming from outside the 60 – 130 GeV mass region was calculated to be below 0.1 % and therefore deemed negligible.

The PDF uncertainty was estimated using the NLO Melnikov-Petriello code [88, 89] using the CTEQ6.1M error sets. The uncertainty found using this procedure was +1.6 % and -2.0 %. A symmetrized value of 1.8 % corresponding to the CTEQ6.1M error sets was added in quadrature to the difference in acceptance when using the MRST2004 PDFs at NLO plus the additional variation when going from NLO to NNLO with MRST2004 (0.9 %), resulting in a total PDF uncertainty of 2.0 %.

The uncertainty on the total integrated luminosity is 6.1 % [91]. Table 6.8 summarizes all the systematic uncertainties, differentiated by tau type as well as for the sum of all types.

Source	Type 1	Type 2	Type 3	All types
Tau Energy Scale	1.0 %	1.0 %	1.0 %	1.0 %
Tau NN	4.0 %	1.2 %	4.0 %	2.4 %
Tau track reconstruction	1.4 %	1.4 %	2.2 %	1.6 %
QCD background	3.8 %	1.2 %	4.4 %	1.5 %
$W \rightarrow \mu\nu$ background	0.2 %	0.1 %	0.5 %	0.4 %
Charge misidentification	1.0 %	1.0 %	1.0 %	1.0 %
Trigger	2.7 %	2.7 %	2.7 %	2.7 %
Muon identification	0.4 %	0.4 %	0.4 %	0.4 %
Muon track match	0.8 %	0.8 %	0.8 %	0.8 %
Muon smearing	0.4 %	0.4 %	0.4 %	0.4 %
Vertex reconstruction	0.2 %	0.2 %	0.2 %	0.2 %
CAL flag efficiency	1.0 %	1.0 %	1.0 %	1.0 %
MC statistics	0.6 %	0.6 %	0.6 %	0.6 %
PDF	2.0 %	2.0 %	2.0 %	2.0 %
Total (except Luminosity)	6.9 %	4.4 %	7.5 %	5.1 %
Luminosity	6.1 %	6.1 %	6.1 %	6.1 %

Table 6.8. *Systematic uncertainties on $\sigma(p\bar{p} \rightarrow Z) \cdot \text{Br}(Z \rightarrow \tau^+\tau^-)$ measurement.*

6.9 Results

The cross section times branching ratio for $p\bar{p} \rightarrow Z/\gamma^* \rightarrow \tau^+\tau^-$ is given by the number of signal events divided by the product of the total efficiency and the integrated luminosity. The number of signal events estimated from Table 6.4, with the second order correction for signal events reconstructed as SS, is 1227. Since Table 6.4 shows the estimated number of events from the Z boson mass range 15 – 500 GeV, other corrections have to be made in order to compare the result of this analysis with theoretical cross sections. The number of events expected from the mass region 15 – 60 GeV (7) as well as from the 130 – 500 GeV mass region (26) were subtracted from the number of signal events in data. The total efficiency for $Z \rightarrow \tau^+\tau^-$ events in the 60 – 130 GeV mass region is $4.9 \cdot 10^{-3}$, which also includes the trigger efficiency of 52.3 %. Given the systematic uncertainties listed in Table 6.8 and an integrated luminosity of 1003 pb^{-1} , we estimate that for the Z boson mass region of 60 – 130 GeV:

$$\sigma(p\bar{p} \rightarrow Z/\gamma^*) \cdot \text{Br}(Z/\gamma^* \rightarrow \tau^+\tau^-) = 245 \pm 8 \text{ (stat)} \pm 12 \text{ (sys)} \pm 15 \text{ (lumi)} \text{ pb},$$

which is in good agreement with the standard model NNLO prediction of $256.6^{+5.1}_{-12}$ pb [93–95]. Finally, a factor of 0.98 [93–95] was applied to estimate the pure Z cross section as opposed to the Z/γ^* cross section for this mass region. Therefore we obtain:

$$\sigma(p\bar{p} \rightarrow Z) \cdot \text{Br}(Z \rightarrow \tau^+\tau^-) = 240 \pm 8 \text{ (stat)} \pm 12 \text{ (sys)} \pm 15 \text{ (lumi)} \text{ pb},$$

which is again in good agreement with the standard model NNLO prediction of $251.9^{+5.0}_{-11.8}$ pb [93–95] resulting from using the MRST2004 NNLO parton density functions, as well as with the $241.6^{+3.6}_{-3.2}$ pb [79] value obtained using CTEQ6.1M NNLO PDFs.

The cross section results for the separate tau candidate types are:

$$\sigma(p\bar{p} \rightarrow Z) \cdot \text{Br}(Z \rightarrow \tau^+\tau^-) = 238 \pm 24 \text{ (stat)} \pm 16 \text{ (sys)} \pm 15 \text{ (lumi)} \text{ pb for type 1,}$$

$$\sigma(p\bar{p} \rightarrow Z) \cdot \text{Br}(Z \rightarrow \tau^+\tau^-) = 244 \pm 10 \text{ (stat)} \pm 11 \text{ (sys)} \pm 15 \text{ (lumi)} \text{ pb for type 2,}$$

$$\sigma(p\bar{p} \rightarrow Z) \cdot \text{Br}(Z \rightarrow \tau^+\tau^-) = 236 \pm 16 \text{ (stat)} \pm 18 \text{ (sys)} \pm 15 \text{ (lumi)} \text{ pb for type 3.}$$

The previous DØ result was $237 \pm 15 \text{ (stat)} \pm 18 \text{ (sys)} \pm 15 \text{ (lumi)} \text{ pb}$ [92]. However, one should bear in mind that the luminosity estimate used in the analysis published in [92] was 14 % lower than the value we calculate now for the data used in that analysis. This was a problem common to all DØ analyses from Run IIa done before 2006 [91], including the results in the $Z \rightarrow e^+e^-$ and $Z \rightarrow \mu^+\mu^-$ channels shown in Fig. 6.21. This figure gives a comparison of the result obtained in this thesis with other Z cross section measurements, as well as with the theoretical calculation from [93–95]. The good agreement with all these independent estimates convincingly demonstrates the ability of the DØ experiment to identify and reconstruct tau leptons and thus experimentally establishes our sensitivity for observing signatures such as $H \rightarrow \tau^+\tau^-$.

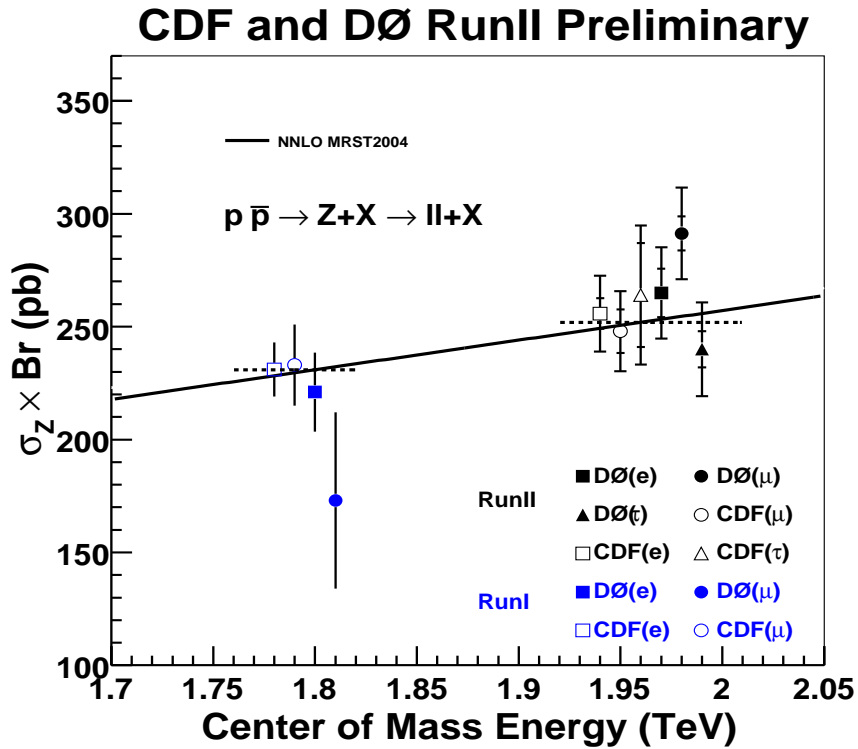


Figure 6.21. Comparison of the available measured Z cross section times branching ratios performed by DØ and CDF in all lepton channels [96–100] to the theoretical predictions from [93–95]. Two sets of measurements are shown, obtained at $\sqrt{s} = 1.8 \text{ TeV}$ (Run I) and $\sqrt{s} = 1.96 \text{ TeV}$ (Run II). For clarity some of the results were represented at slightly higher or lower center of mass energies. The dashed horizontal lines indicate the theoretical predictions at those two center of mass energy values.

Limits on neutral Higgs boson production

7.1 Limits on SM Higgs boson production

The $\sigma \cdot \text{Br}(\text{p}\bar{\text{p}} \rightarrow \text{Z} \rightarrow \tau^+\tau^-)$ analysis presented in the previous chapter shows good agreement between data and the expected contribution from Standard Model processes. Since no obvious excess of events was observed, indicating the lack of additional resonant production of tau lepton pairs, the analysis can be used to establish limits on the production of a neutral Higgs boson. This is done for a Higgs boson with hypothetical mass equal to or higher than the Z boson mass, assuming the theoretical prediction for the Z boson contribution to the visible mass peak [93–95] is correct. The $\text{Z} \rightarrow \tau^+\tau^-$ events are treated as irreducible background, since there is no distinction between such events and the ones in which a Higgs boson decays into a tau lepton pair, besides the difference in mass between the two bosons (the difference in the tau lepton polarization coming from the fact that the Higgs boson is a scalar and the Z boson a vector is not one that we can easily exploit).

To set the limits, the visible mass distribution of the final selection sample is used, as given in Figs. 6.18 and 6.19, both in linear and logarithmic scales. This variable provides good separation between signal and background, since the signal from Higgs boson production with a mass above 90 GeV would appear as an excess of events in the high visible mass region, beyond the Z boson peak. An example of this separation and of the visible mass distribution for a Higgs boson with a mass of 160 GeV is shown in Fig. 7.1. Note that in this figure the Higgs boson production cross section is largely exaggerated compared to the expected SM cross section. Figure 6.19 shows that the data distribution is well described by the SM background prediction and no data excess above the background is apparent. It is therefore concluded that a signal is not observed. To quantify the possible level of observable signal, cross section times branching fraction limits are calculated for the process $\text{p}\bar{\text{p}} \rightarrow \text{H} \rightarrow \tau^+\tau^-$, using a semi-frequentist approach also known as the “LEP CL_s method” [101–104].

The two most important features of this method are the use of modified frequentist confidence levels and the log-likelihood ratio test statistic. The test statistic is the ratio of Poisson likelihoods for signal + background to background-only hypotheses, $Q = L(s+b)/L(b)$. If s is the number of signal events, b the number of background events and d the observed number of events in data, the definition is:

$$Q = \frac{e^{-(s+b)}(s+b)^d}{d!} \bigg/ \frac{e^{-b}b^d}{d!} = \frac{e^{-(s+b)}(s+b)^d}{e^{-b}b^d}. \quad (7.1)$$

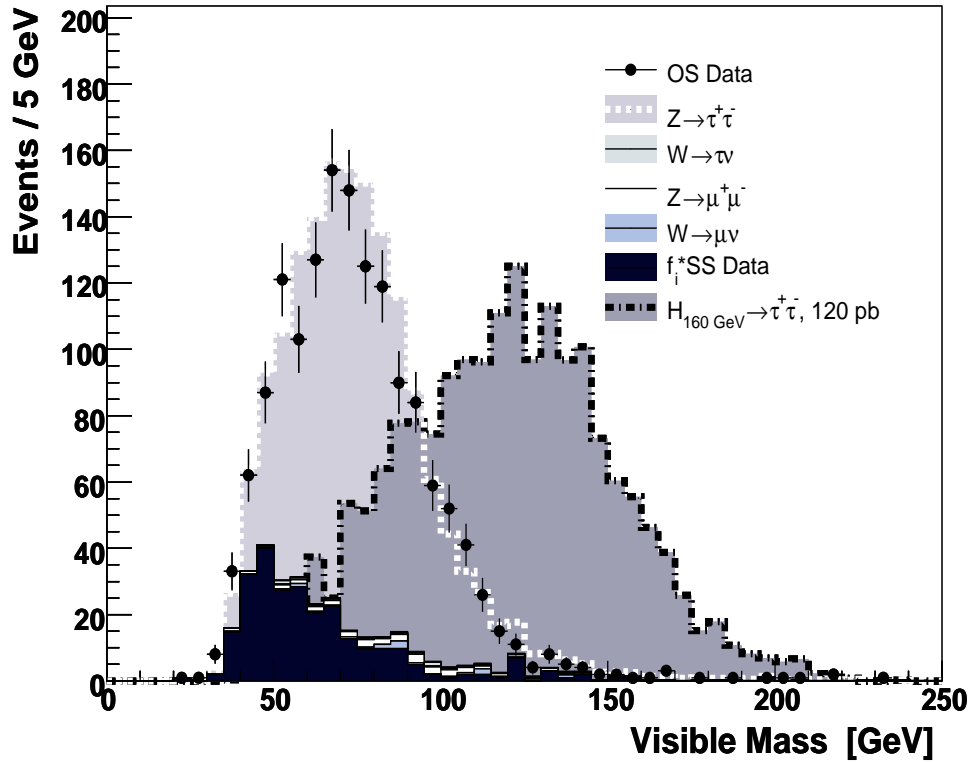


Figure 7.1. The separation between the known SM backgrounds and the Higgs boson as given by the visible mass distribution. The signal distribution illustrated here corresponds to a Higgs boson with mass of 160 GeV and is normalized using a cross section of 120 pb.

Each bin of the visible mass histogram is considered as a separate experiment. The test statistics for the ensemble of all bins is the product of the individual test statistics for each bin in the mass distribution:

$$Q' = \prod_i Q_i. \quad (7.2)$$

For reasons of computational efficiency, a slightly different form of this test statistics is used, called log-likelihood ratio (LLR) $\chi = -2\ln(Q)$. For each bin with d observed data events

$$\chi_d = -2\ln(Q_d) = 2 \left[s - d \ln \left(1 + \frac{s}{b} \right) \right], \quad (7.3)$$

which gives for the whole visible mass distribution the statistic

$$\chi'_d = -2\ln(Q'_d) = 2 \left[\sum_i s_i - \sum_i d_i \ln \left(1 + \frac{s_i}{b_i} \right) \right]. \quad (7.4)$$

Based on the LLR test statistic, the frequentist confidence level for the existence of some signal in addition to the expected background (the signal-plus-background hypothesis) is given by

$$CL_{s+b} = P_{s+b}(\chi' \leq \chi'_d) = \int_{-\infty}^{\chi'_d} \frac{dP_{s+b}}{d\chi'} d\chi', \quad (7.5)$$

while the confidence level for the background-only hypothesis is

$$CL_b = P_b(\chi' \leq \chi'_d) = \int_{-\infty}^{\chi'_d} \frac{dP_b}{d\chi'} d\chi', \quad (7.6)$$

where the differential probability $dP_n/d\chi$ is defined by a population of χ_n in which n is Poisson distributed with mean value n . In practice, these Poisson distributions are sampled randomly over many Monte Carlo iterations (trials) or pseudo-experiments to simulate representative outcomes of repeated experiments measuring the values s , b and d . Another method described in [104] computes instead the Poisson probability distribution function (PDF) for each instance of the test statistic. The prescription is to then iteratively combine channels (or bins) by convoluting the PDFs of each. In this method, an approximation is introduced to shorten the computation time by binning the PDFs and populating each bin with some number of MC trials. The modified frequentist confidence level, or CL_s , is defined as:

$$CL_s = CL_{s+b}/CL_b. \quad (7.7)$$

Each systematic uncertainty is taken into account by smearing the probability density functions (PDFs) P_{s+b} and P_b with a Gaussian distribution. This is done while maintaining the correlations between bins, as well as between signal and background, using a matrix of correlation coefficients. The systematic uncertainties used for limit calculation are essentially the same as in Chapter 6 and are listed in Table 7.1. The difference between the theoretical estimations for the Z boson cross section from [93–95] and [79] is added as a PDF uncertainty of 4 % to the 2 % estimate from the previous chapter.

A set of 10^5 pseudo-experiments simulates the expectations for signal and background (s_i and b_i) in each bin i of the visible mass histogram. Performing a pseudo-experiment means that two random numbers are generated, one for the signal and one for the background. These numbers are generated according to two Poissonian distributions, one for signal and one for background, both smeared by Gaussian distributions corresponding to each systematic uncertainty and having as their mean the number of signal, respectively background events expected for that particular bin. For the signal, this number corresponds to a certain cross section, which is varied up and down until CL_s reaches a value of 5 %. The LLR is calculated for each pseudo-experiment and the width of the LLR distribution gives an estimate of how sensitive the analysis is to a signal-like fluctuation in data, a high value compared to the signal expectation indicating a low sensitivity. The signal hypothesis is excluded at 95 % confidence level if $CL_s < 5$ %.

Source	Background (%)				Signal (%)
	$Z \rightarrow \tau^+\tau^-$	$W \rightarrow \tau\nu, WW, Z \rightarrow \mu^+\mu^-, t\bar{t}$	$W \rightarrow \mu\nu$	QCD	$H \rightarrow \tau^+\tau^-$
Tau Energy Scale	1.0	1.0	1.0		1.0
Tau NN	2.4	2.4			2.4
Tau track reconstruction	1.6	1.6			1.6
QCD background				5	
$W \rightarrow \mu\nu$ background			28		
Charge misidentification	1.0	1.0			1.0
Trigger	2.7	2.7			2.7
Muon identification	0.4	0.4			0.4
Muon track match	0.8	0.8			0.8
Muon smearing	0.4	0.4			0.4
Vertex reconstruction	0.2	0.2			0.2
CAL flag efficiency	1.0	1.0			1.0
MC statistics	0.6	0.6			0.6
PDF	4.5				4.2
Total (except Lum.)	6.2	4.4	28	5	6.0
Luminosity	6.1	6.1			6.1
Total	8.7	7.5	28	5	8.5

Table 7.1. *Systematic uncertainties (in %) on accepted numbers of events categorized by background and signal source. The uncertainties are row-wise fully correlated.*

The smearing for each systematic uncertainty reduces the separation between signal and background due to the broadening of the PDFs. Systematic uncertainties are often estimated rather than measured, their value being typically overestimated as a sign of caution. Two limit setting procedures, both using the LEP CL_s method but based on two different approaches for treating the systematic uncertainties, have been used to calculate upper limits on $p\bar{p} \rightarrow H \rightarrow \tau^+\tau^-$ production and are briefly described below. The first one is the TLimit method [104,105] as implemented in ROOT [106]. The TLimit code calculates the observed cross section limit, as well as the median expected limit in the case where no signal would be present. Each source of systematic uncertainty is described by a number, which is used for the Gaussian smearing of the Poisson distributions used for sampling the number of signal and background events when the pseudo-experiments are performed.

The results of the cross section times branching fraction limit as a function of the Higgs boson mass hypothesis are given in Table 7.2 and illustrated in Fig. 7.2. The expected limit follows a distribution, which is characterised by both a mean or median value and a width. As an indication of the width of the expected limit distribution, the expected limits corresponding to one standard deviation in the signal-plus-background over background-only confidence level are considered and indicated in Fig. 7.2 by the yellow (light grey) shaded band around the median expected limit.

m_H (GeV)	90	100	110	120	130	140	150	160	170
Expected limit (pb)	31.1	24.5	15.1	10.1	7.8	4.4	3.2	2.8	1.7
Observed limit (pb)	21.7	18.3	10.8	6.8	3.9	2.5	2.1	1.2	1.1

Table 7.2. *Expected and observed upper limits on $\sigma(p\bar{p} \rightarrow H) \cdot \text{Br}(H \rightarrow \tau^+\tau^-)$ obtained using TLimit, as a function of the Higgs boson mass hypothesis.*

The second limit setting procedure uses a method for treating systematic uncertainties called “profiling” (within DØ this method is also known as “clfit2”), described in [107,108]. Given a set of predictions, observations and systematic uncertainties, one can define a model which represents the best fit to the data observation within the constraints of the systematic uncertainties. This is done by minimising

$$\chi^2 = 2 \sum_i \left[(p'_i - d_i) - d_i \ln \left(\frac{p'_i}{d_i} \right) \right] + \sum_k S_k^2, \quad (7.8)$$

by fitting the parameters S_k , where

$$p'_i = p_i \prod_{k=1}^K (1 + f_k^i S_k) \quad (7.9)$$

are the systematically varied predictions for bin i and f_k^i are the contributed sizes of each of the K sources of uncertainty. The values S_k are random numbers generated using a Gaussian distribution centered at 0 and having a width equal to 1. The fitted values of S_k give the best estimates for each background source. To properly incorporate the profile likelihood into the limit calculation, the profile likelihood must be recalculated each time a pseudoexperiment is simulated. This is equivalent to performing a best fit for each simulated outcome of the experiment.

For comparison the expected and observed limits obtained using the clfit2 method, which are the lowest ones to date, are also shown in Fig. 7.2 along with the ones obtained using TLimit. Table 7.3 shows the observed and expected limit results obtained using this method, along with the Standard Model prediction for the cross section times branching ratio of the process $\sigma(p\bar{p} \rightarrow H) \cdot \text{Br}(H \rightarrow \tau^+\tau^-)$ from [109].

m_H (GeV)	90	100	110	120	130	140	150	160	170
Exp. lim. (pb)	32.1	21.5	11.1	7.1	4.5	3.3	2.6	2.1	1.6
Obs. lim. (pb)	22.5	17.9	15.9	6.3	3.7	2.5	1.8	1.5	1.2
SM pred. (pb)		0.131	0.098	0.068	0.043	0.023	0.010	0.002	0.0003

Table 7.3. *Expected and observed upper limits on $\sigma(p\bar{p} \rightarrow H) \cdot \text{Br}(H \rightarrow \tau^+\tau^-)$ obtained using the clfit2 method, as a function of the Higgs boson mass hypothesis. The theoretical Standard Model prediction of $\sigma \cdot \text{Br}$ for this process [109] is also shown for each Higgs boson mass value.*

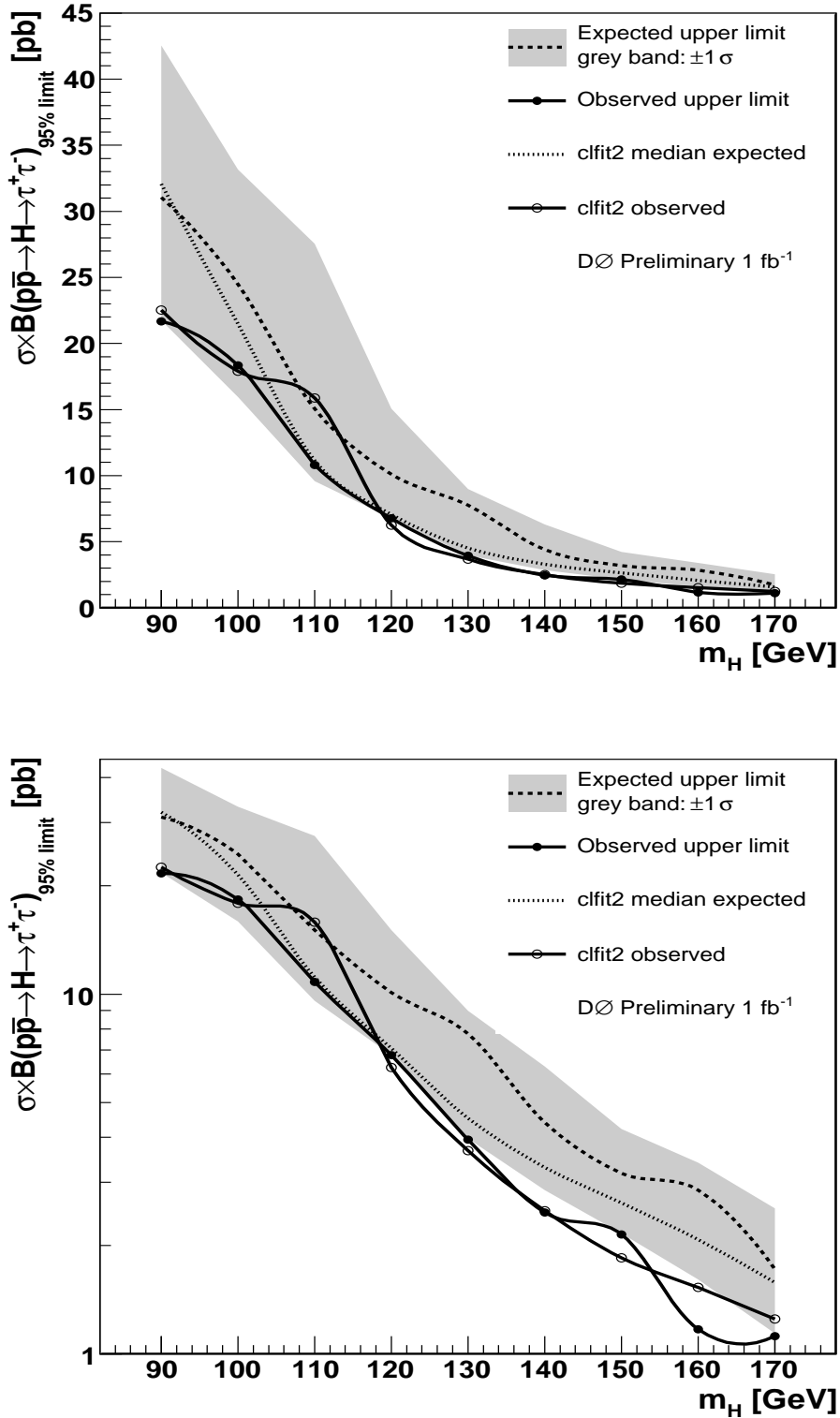


Figure 7.2. Expected and observed upper limits on $\sigma(p\bar{p} \rightarrow H) \cdot \text{Br}(H \rightarrow \tau^+\tau^-)$ as a function of the Higgs boson mass hypothesis, in linear (upper) and in logarithmic (lower) scale, for both TLimit and clfit2 methods.

Figure 7.3 shows the ratio between the expected or observed limits obtained using both methods described above and the theoretical Standard Model prediction of $\sigma \cdot \text{Br}$ for the $\sigma(p\bar{p} \rightarrow H) \cdot \text{Br}(H \rightarrow \tau^+\tau^-)$ process from [109]. These results set the tightest limits to date on the cross section times branching ratio for the process $p\bar{p} \rightarrow H \rightarrow \tau^+\tau^-$ for a Higgs boson with a mass below 130 GeV and are comparable for the rest of the studied mass interval with the recent preliminary results obtained by the CDF experiment [40], which are based on 1.8 fb^{-1} of integrated luminosity and use three separate channels: $H \rightarrow \tau(\rightarrow \mu\nu_\tau\nu_\mu)\tau(\rightarrow e\nu_\tau\nu_e)$, $H \rightarrow \tau(\rightarrow \mu\nu_\tau\nu_\mu)\tau(\rightarrow \text{hadrons})$ and $H \rightarrow \tau(\rightarrow e\nu_\tau\nu_e)\tau(\rightarrow \text{hadrons})$. However, this analysis is still far from probing the existence or inexistence of a Standard Model Higgs boson. The upper limits set here are higher than the theoretical SM Higgs boson cross section by factors of 80 – 160 for the relevant Higgs boson mass interval.

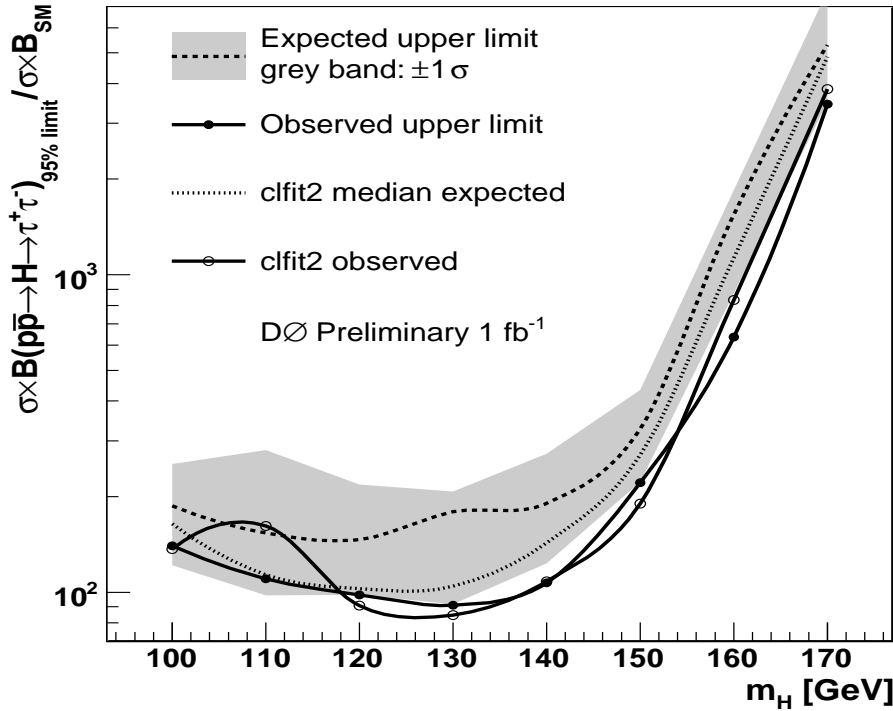


Figure 7.3. The ratio between the expected or observed limits (obtained using *TLimit* and *clfit2*) and the theoretical Standard Model prediction [109] of $\sigma \cdot \text{Br}$ for the process $\sigma(p\bar{p} \rightarrow H) \cdot \text{Br}(H \rightarrow \tau^+\tau^-)$, in logarithmic scale.

Figure 7.4 shows the visible mass distribution and in addition, for several Higgs boson mass hypotheses, the contribution of a Higgs boson signal normalized by the cross section times branching fraction that corresponds to the observed limits obtained using *TLimit*, in linear scale. Figure 7.5 shows the same distributions in logarithmic scale to better emphasize the low possible Higgs boson contribution at high m_H values.

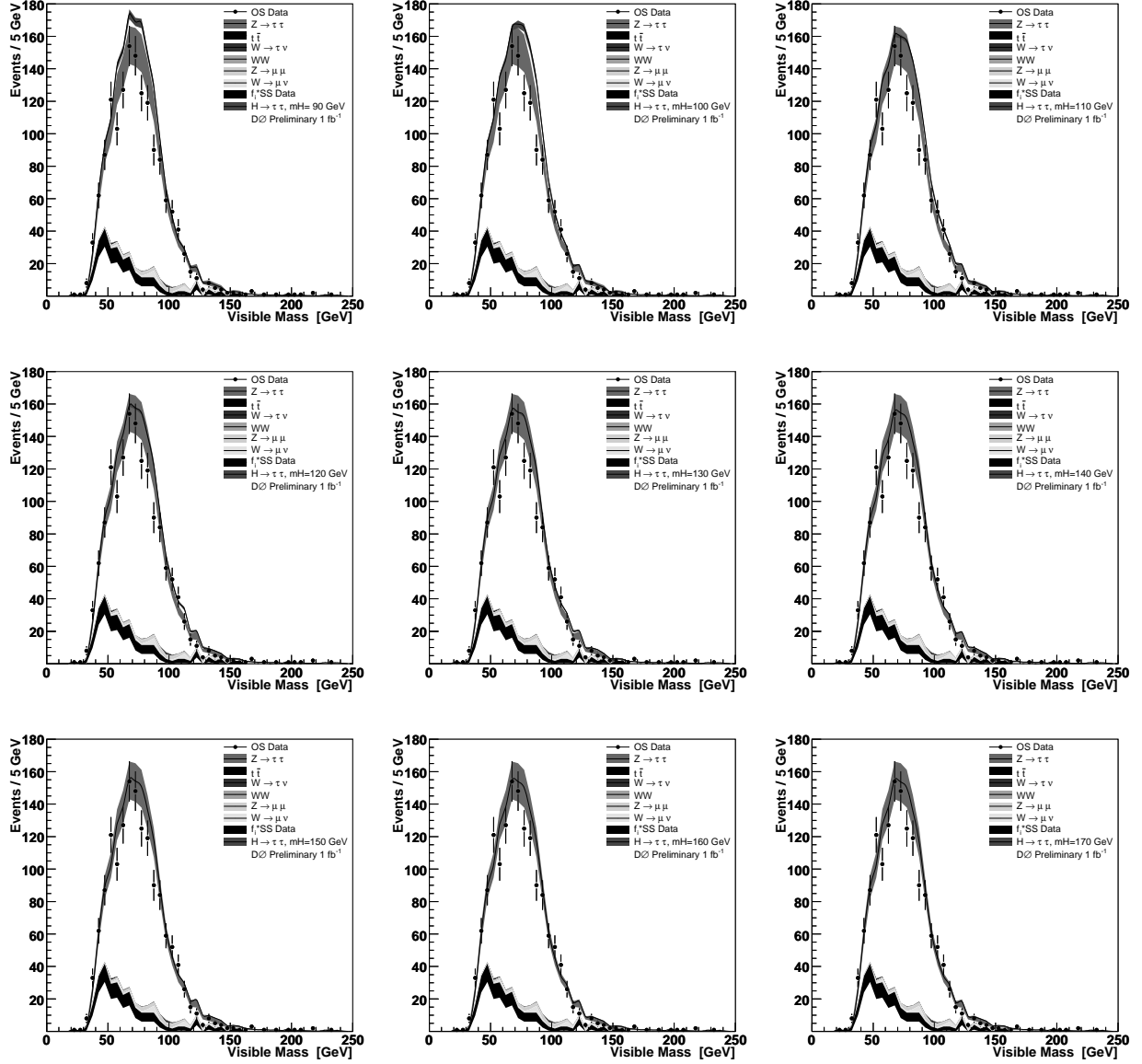


Figure 7.4. Visible mass distribution for tau lepton pairs. For each of the Higgs boson mass hypotheses $m_H=90$ GeV (upper left), 100 GeV (upper middle), 110 GeV (upper right), 120 GeV (middle left), 130 GeV (middle), 140 GeV (middle right), 150 GeV (lower left), 160 GeV (lower middle) and 170 GeV (lower right) the amount of Higgs boson signal on top of the SM background is indicated by the black line and orange band. The SM background prediction is broken down in its components and plotted in an accumulated way. The Higgs boson signal is normalized to the observed limit obtained using the TLimit method. The vertical scale is linear in number of events.

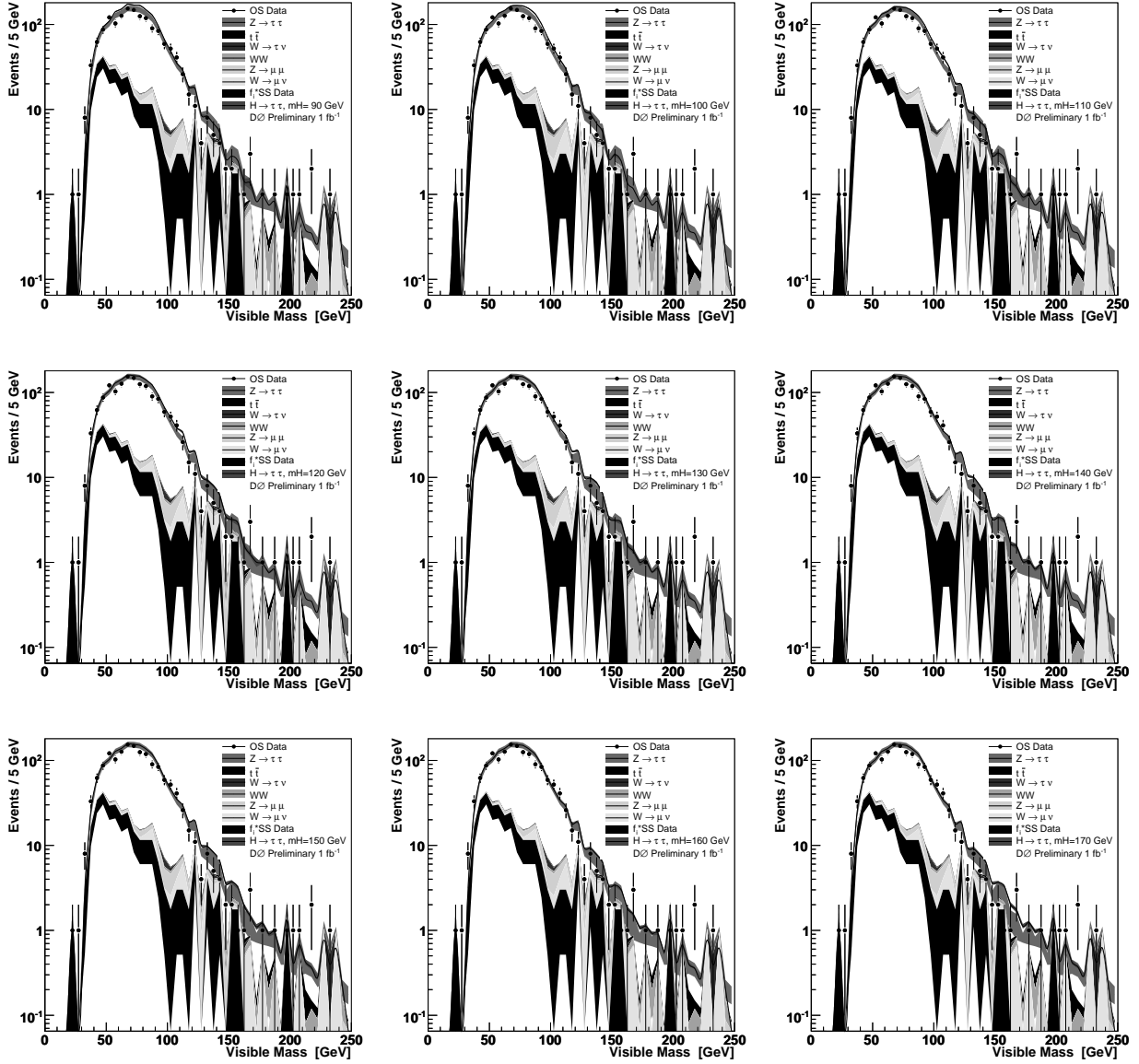


Figure 7.5. Visible mass distribution for tau lepton pairs. For each of the Higgs boson mass hypotheses $m_H=90$ GeV (upper left), 100 GeV (upper middle), 110 GeV (upper right), 120 GeV (middle left), 130 GeV (middle), 140 GeV (middle right), 150 GeV (lower left), 160 GeV (lower middle) and 170 GeV (lower right) the amount of Higgs boson signal on top of the SM background is indicated by the black line and orange band. The SM background prediction is broken down in its components and plotted in an accumulated way. The Higgs boson signal is normalized to the observed limit obtained using the TLimit method. The vertical scale is logarithmic in number of events.

7.2 Limits in the $\tan\beta - m_A$ plane for the MSSM

A search for neutral MSSM Higgs bosons was carried out in the $\tau^+\tau^-$ channel and interpreted within the four benchmark scenarios from [33,34] which were briefly discussed in Section 2.6. The process which is expected for most MSSM Higgs bosons masses to have the highest cross section is, as in the case for the SM Higgs boson production at the Tevatron, the gluon-gluon fusion shown in Fig. 7.6. For high values of $\tan\beta$, the $b\bar{b}$ annihilation is expected to contribute significantly as well, as shown in Section 2.6. The cross section times branching ratio of the Higgs bosons were calculated for each of these scenarios using FEYNHIGGS 2.6.2 [110]. The top-quark mass used for these calculations was the world average value of 172.6 GeV [111]. The cross sections for the processes $p\bar{p} \rightarrow h, A, H \rightarrow \tau^+\tau^-$ at each $(\tan\beta, m_A)$ point were calculated by adding the cross sections for gluon-gluon fusion and $b\bar{b}$ annihilation. The cross sections for the process $p\bar{p} \rightarrow A \rightarrow \tau^+\tau^-$ was used for the actual limit setting. In the region where either h or H is degenerate in mass with A , the cross section for the additional degenerate state was added to the cross section for the A . The limits in the $\tan\beta - m_A$ plane were calculated based on the limits set on Higgs boson production in the previous section, obtained with the profiling (clfit2) method.

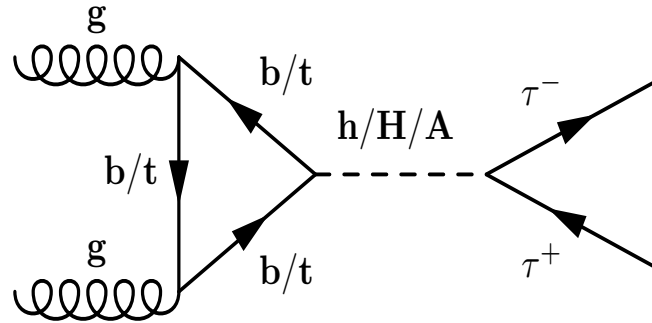


Figure 7.6. Production of the MSSM Higgs boson through gluon-gluon fusion and subsequent decay into a tau lepton pair.

It is worth noting that since A is a pseudo-scalar (CP-odd), while h and H are scalar (CP-even, like the SM Higgs boson), the angular distributions for the decay $A \rightarrow \tau^+\tau^-$ will be slightly different from the angular distributions of the $h, H \rightarrow \tau^+\tau^-$ decay. The efficiencies calculated in the previous section for the SM Higgs boson are thus only an approximation of the efficiencies for the $A \rightarrow \tau^+\tau^-$ process. This effect was studied at LEP and was found to be negligible. Also, the limits set here only hold for the assumption of a narrow Higgs boson resonance. Given the benchmark scenarios followed here for setting the limits in the $\tan\beta - m_A$ plane and the experimental resolution of the Higgs boson resonance in the $\tau^+\tau^-$ channel, the effect of the MSSM Higgs boson width is considered to be negligible as well. Table 7.4 gives the expected and observed upper limits on $\tan\beta$ set by the analysis presented here.

m_A (GeV)	90	100	110	120	130	140	150	160	170
Exp. lim. ($m_h^{\max}, \mu < 0$)	55.2	57.6	52.2	51.4	50.2	51.8	55.2	58.2	59.7
Exp. lim. ($m_h^{\max}, \mu > 0$)	57.2	59.9	54.0	53.2	52.0	53.7	57.4	60.7	62.3
Exp. lim. (no mix, $\mu < 0$)	55.8	58.3	52.8	52.0	50.8	52.4	55.9	59.0	60.5
Exp. lim. (no mix, $\mu > 0$)	56.3	58.9	53.2	52.4	51.2	52.9	56.5	59.6	61.1
Obs. lim. ($m_h^{\max}, \mu < 0$)	47.8	54.6	64.7	50.1	46.8	46.7	48.0	51.8	55.3
Obs. lim. ($m_h^{\max}, \mu > 0$)	46.4	52.8	62.1	48.3	45.3	45.2	46.5	50.0	53.2
Obs. lim. (no mix, $\mu < 0$)	46.9	53.4	62.9	49.0	49.6	45.7	47.0	50.6	53.9
Obs. lim. (no mix, $\mu > 0$)	47.2	53.8	63.6	49.4	50.1	46.0	47.3	51.1	54.4

Table 7.4. Expected and observed upper limits on $\tan\beta$ as a function of m_A using the cross section limits on Higgs boson production obtained with the profiling (clfit2) method, for the four benchmark scenarios from [33,34] briefly described in Section 2.6.

Figure 7.7 (left) shows the excluded regions in the $\tan\beta - m_A$ plane corresponding to the two m_h^{\max} scenarios ($\mu < 0$ and $\mu > 0$), while Fig. 7.7 (right) shows the excluded regions in the same plane which correspond to the two no-mixing scenarios ($\mu < 0$ and $\mu > 0$). These limits are comparable with the ones obtained by CDF with 1.8 fb^{-1} of data. As shown in the figures, only the region $4 < \tan\beta < 55$ is still allowed for possible realisations of the MSSM, as long as the extrapolation from the two cases that were investigated - the no-mixing and the maximal-mixing scenarios - is considered valid.

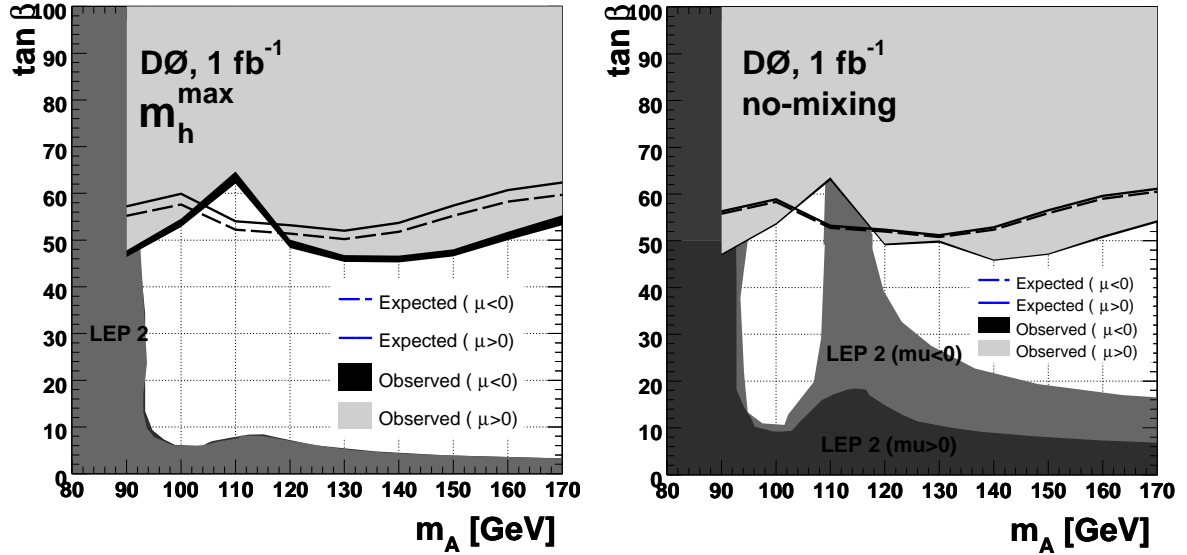


Figure 7.7. Excluded regions for $\tan\beta$ as a function of m_A using the cross section limits on Higgs boson production obtained with the profiling (clfit2) method, for the four benchmark scenarios from [33,34] briefly described in Section 2.6.

Conclusions and outlook

The cross section times branching ratio $\sigma \cdot \text{Br}$ for the process $p\bar{p} \rightarrow Z \rightarrow \tau^+\tau^-$ was measured at $\sqrt{s} = 1.96$ GeV using 1.0 fb^{-1} of data collected by the DØ experiment. This measurement was performed in the channel in which one of the tau leptons decays to a muon and neutrinos, while the other decays either hadronically or to an electron and neutrinos. The result of this measurement is $240 \pm 8 \text{ (stat)} \pm 12 \text{ (syst)} \pm 15 \text{ (lumi) pb}$, in good agreement with the theoretical predictions of $241.6^{+3.6}_{-3.2} \text{ pb}$ [79] or $251.9^{+5.1}_{-12} \text{ pb}$ [93–95], as well as with other measurements performed by the DØ and CDF experiments in all channels in which the Z boson decays leptonically [96–100]. This is the most precise Z boson cross section measurement to date performed in the tau lepton channel at hadron colliders. The analysis demonstrates that the DØ experiment can identify tau leptons decaying to hadrons with good efficiency and good background rejection, a challenging task in an environment dominated by QCD jets. This achievement can now be used as a basis for other analyses using hadronic tau lepton decays. The result was presented at the Lepton-Photon 2007 conference [112] as preliminary and is currently prepared for publication in 2008.

As no evidence for additional sources of resonant $\tau^+\tau^-$ events was found, limits on the production of a neutral Higgs boson were set. The Higgs boson is an essential ingredient of electroweak symmetry breaking in the Standard Model of particle physics, but so far has remained unobserved experimentally. The results obtained in this thesis set the tightest limits to date on the cross section times branching ratio for the process $p\bar{p} \rightarrow H \rightarrow \tau^+\tau^-$ for a Higgs boson with a mass below 130 GeV and are comparable for the rest of the studied mass interval with the recent preliminary results obtained by the CDF experiment [40], which are based on 1.8 fb^{-1} of integrated luminosity and use three separate channels: $H \rightarrow \tau(\rightarrow \mu\nu_\tau\nu_\mu)\tau(\rightarrow e\nu_\tau\nu_e)$, $H \rightarrow \tau(\rightarrow \mu\nu_\tau\nu_\mu)\tau(\rightarrow \text{hadrons})$ and $H \rightarrow \tau(\rightarrow e\nu_\tau\nu_e)\tau(\rightarrow \text{hadrons})$.

Even in the most sensitive region, for a Higgs boson mass of 100 – 150 GeV, this analysis is still far from probing the existence or inexistence of a Standard Model Higgs boson. The upper limits set here are higher than the theoretical SM Higgs boson cross section by factors of 80 – 160 for this particular Higgs boson mass interval, and even higher for lower or higher mass values.

Final states leading to high-mass tau lepton pairs can also arise from various physics processes beyond the Standard Model, including the production of neutral Higgs bosons in the Minimal Supersymmetric Standard Model (MSSM). A search for a Higgs boson decaying to tau leptons is of particular interest in models with more than one Higgs doublet, where production rates for $p\bar{p} \rightarrow H \rightarrow \tau^+\tau^-$ can potentially be large enough for an observation at the Tevatron.

Within the MSSM, if the mass of the CP-odd neutral scalar Higgs boson m_A is low and $\tan\beta$ (the ratio of vacuum expectation values of the two supersymmetric Higgs doublets) is large, the Higgs boson production via b quarks can be greatly enhanced, by a factor of $\tan^2\beta$. The gluon-gluon fusion cross section is slightly enhanced as well in this case, in comparison to the cross section for the equivalent SM process. Besides, one of the CP-even neutral Higgs bosons (h or H) is degenerate with A, which effectively doubles the cross section. In this region, decays of the Higgs boson to $b\bar{b}$ (90 %) and $\tau^+\tau^-$ (9 %) dominate. The advantage of the $\tau^+\tau^-$ channel over the $b\bar{b}$ one is that it entails a significantly lower amount of background from QCD processes and is less sensitive to radiative corrections, which largely compensates for the lower branching ratio.

Since no excess of events with respect to the expected contributions from the Standard Model processes was observed, upper limits on $\tan\beta$ were set for certain MSSM benchmark scenarios [33,34] using the cross section limits on the $p\bar{p} \rightarrow H \rightarrow \tau^+\tau^-$ obtained with the profiling method. These limits exclude $\tan\beta$ values above 40 – 60 for the Higgs boson mass interval 90 – 170 GeV, being comparable with those set by the CDF experiment [40] for the entire Higgs boson mass range studied in this thesis. Lower limits of typically 4 – 20 were set on $\tan\beta$ at LEP [35]. For a certain scenario within MSSM (no-mixing, $\mu < 0$), the mass region 112 – 120 GeV is already excluded [113].

The data set collected by the DØ experiment at the time this analysis was completed already reached 3.4 fb^{-1} and the Tevatron is expected to deliver 8 fb^{-1} by 2010. Higher luminosity, the inclusion of the channel $p\bar{p} \rightarrow H \rightarrow \tau(\rightarrow e\nu_\tau\nu_e)\tau(\rightarrow \text{hadrons})$ and allowing more than one trigger to fire will lead to a significant increase in sensitivity for this search. Another possible improvement could be the implementation of multivariate analysis techniques such as neural networks or decision trees, which would allow to make use of the differences between the signal and background distributions of several kinematic variables. Finally the combination of the results from the two experiments at Fermilab, DØ and CDF, is desirable for obtaining the best possible outcome. If supersymmetry exists, the process $p\bar{p} \rightarrow H \rightarrow \tau^+\tau^-$ is one of the most sensitive channels for a discovery at the Tevatron.

Bibliography

- [1] R. Ellis, J. Silk, “New Frontiers in Cosmology and Galaxy Formation: Challenges for the Future”, to appear in “Structure Formation in the Universe”, Ed. G. Chabrier, Cambridge University Press, arXiv:astro-ph/0712.2865v1 (2007).
- [2] A. Albrecht *et al.*, “Report of the Dark Energy Task Force”, arXiv:astro-ph/0609591v1 (2006).
- [3] S.L. Glashow, “Partial symmetries of Weak Interactions”, *Nucl. Phys.* 22, 579 (1961).
- [4] A. Salam, “Elementary Particle Theory”, Ed. N. Svartholm. Almquist and Wiksell, Stockholm, p. 376 (1968).
- [5] S. Weinberg, “A Model of Leptons”, *Phys. Rev. Lett.* 19, 1264 (1967).
- [6] M.L. Perl *et al.*, “Evidence for anomalous lepton production in e^+e^- annihilation”, *Phys. Rev. Lett.* 35, 1489 (1975).
- [7] UA1 Collaboration (G. Arnison *et al.*), “Experimental observation of isolated large transverse energy electrons with associated missing energy at $\sqrt{s} = 540$ GeV”, *Phys. Lett.* B122, 103 (1983).
- [8] UA2 Collaboration (M. Banner *et al.*), “Observation of Single Isolated Electrons of High Transverse Momentum in Events with Missing Transverse Energy at the CERN $p\bar{p}$ Collider”, *Phys. Lett.* B122, 476 (1983).
- [9] UA1 Collaboration (G. Arnison *et al.*), “Experimental observation of lepton pairs of invariant mass around $95 \text{ GeV}/c^2$ at the CERN SPS collider”, *Phys. Lett.* B126, 398 (1983).
- [10] UA2 Collaboration (M. Bagnaia *et al.*), “Evidence for $Z^0 \rightarrow e^+e^-$ at the CERN anti-p p Collider”, *Phys. Lett.* B 129, 130 (1983).
- [11] Super-Kamiokande Collaboration (Y. Ashie *et al.*), *Phys. Rev. Lett.* 93, 101801 (2004).
- [12] P.W. Higgs, “Broken Symmetries and the masses of gauge bosons”, *Phys. Rev. Lett.* 13, 508 (1964).
- [13] W.-M. Yao *et al.*, *Journal of Physics* G33, 1 (2006).
- [14] D.J. Gross and F. Wilczek, *Phys. Rev. Lett.* 30, 1343 (1973).

- [15] H.D. Politzer, *Phys. Rev. Lett.* 30, 1346 (1973).
- [16] O. Brein, A. Djouadi and R. Harlander, “NNLO QCD corrections to the Higgs-strahlung processes at hadron colliders”, *Phys. Lett.* B579, 149 (2004).
- [17] A. Djouadi, J. Kalinowski and M. Spira, “HDECAY: A program for Higgs boson decays in the Standard Model and its supersymmetric extension”, *Comput. Phys. Commun.* 108, 56 (1998).
- [18] R. Barate *et al.*, “Search for the standard model Higgs boson at LEP”, *Phys. Lett.* B565, 61 (2003).
- [19] The LEP Electroweak Working Group. A Combination of Preliminary, Electroweak Measurements and Constraints on the Standard Model. LEP EW WG Plots for the Winter 2008, <http://lepewwg.web.cern.ch/LEPEWWG> (2008).
- [20] The Tevatron New-Phenomena and Higgs working group, for the CDF and DØ Collaborations, “Combined CDF and DØ Upper Limits on Standard Model Higgs-Boson Production with up to 2.4 fb^{-1} of data”, arXiv:0804.3423v1 [hep-ex] (2008).
- [21] T. Hahn, S. Heinemeyer, F. Maltoni, G. Weiglein, S. Willenbrock, “SM and MSSM Higgs Boson Production Cross Sections at the Tevatron and LHC”, contribution to *Tev4LHC Workshop, 2005 - 2006*, arXiv:hep-ph/0607308v2 (2006).
- [22] C. Quigg, “The Electroweak Theory”, in *Flavor Physics for the Millennium: TASI 2000*, Ed. J.L. Rosner (World Scientific, Singapore, 2001), p. 367, arXiv:hep-ph/0204104 (2001).
- [23] U. Amaldi, W. de Boer, H. Furstenau, “Comparison of grand unified theories with electroweak and strong coupling constants measured at LEP”, *Phys.Lett.* B260, 447 (1991).
- [24] H.P. Nilles, *Phys. Rep.* 110, 1 (1984).
- [25] H.E. Haber and G.L. Kane, *Phys. Rep.* 117, 75 (1985).
- [26] C. Balazs, H.-J. He and C.P. Yuan, *Phys. Rev.* D60, 114001 (1999).
- [27] M. Spira, *Nucl. Inst. Meth.* A389, 357 (1997).
- [28] TeV4LHC Higgs Working Group (U. Aglietti *et al.*), “Tevatron-for-LHC Report: Higgs”, arXiv:hep-ph/0612172v2 (2007).
- [29] S. Heinemeyer, W. Hollik and G. Weiglein, *Eur. Phys. J.* C9, 343 (1999).

- [30] G. Degrandi, S. Heinemeyer, W. Hollik, P. Slavich and G. Weiglein, *Eur. Phys. J.* C28, 133 (2003).
- [31] B. Allanach, A. Djouadi, J. Kneur, W. Porod and P. Slavich, *JHEP* 0409, 044 (2004).
- [32] B. Ananthanarayan, G. Lazarides, Q. Sha, “Top-Quark-Mass Prediction from Supersymmetric Grand Unified Theories”, *Phys. Rev.* D44, 16131615 (1991).
- [33] M. Carena, S. Heinemeyer, C. Wagner, G. Weiglein, “Suggestions for Improved Benchmark Scenarios for Higgs-Boson Searches at LEP2”, contribution to the workshop “New Theoretical Developments for Higgs Physics at LEP2”, CERN, Oct. 1999, arXiv:hep-ph/9912223 (1999).
- [34] M. Carena, S. Heinemeyer, C. Wagner, G. Weiglein, *Eur. Phys. J.* C26, 601 (2003).
- [35] ALEPH, DELPHI, L3, OPAL Collaborations. The LEP Working Group for Higgs Boson Searches, “Search for Neutral MSSM Higgs Bosons at LEP”, *Eur. Phys. J.* C47, 547 (2006).
- [36] DØ Collaboration (V.M. Abazov *et al.*), “Search for neutral supersymmetric Higgs bosons in multijet events at $\sqrt{s} = 1.96$ TeV”, *Phys. Rev. Lett.* 95, 151801 (2005).
- [37] CDF Collaboration (A. Abulencia *et al.*), “Search for neutral MSSM Higgs bosons decaying to τ pairs in $p\bar{p}$ collisions at $\sqrt{s} = 1.96$ TeV”, *Phys. Rev. Lett.* 96, 011802 (2006).
- [38] R. Eusebi, “Search for charged Higgs in $t\bar{t}$ decay products from proton-antiproton collisions at $\sqrt{s} = 1.96$ TeV, PhD thesis, University of Rochester, hep-ex/0510065, CDF Note 7250 (2005).
- [39] M. Carena, S. Heinemeyer, C.E.M. Wagner, G. Weiglein, “MSSM Higgs Boson Searches at the Tevatron and the LHC: Impact of Different Benchmark Scenarios”, arXiv:hep-ph/0511023 (2005).
- [40] CDF Collaboration, “Search for Neutral MSSM Higgs Bosons Decaying to Tau Pairs with 1.8 fb⁻¹ of Data”, CDF Note 9071 (2007).
- [41] DØ Collaboration (V. Abazov *et al.*), “The Upgraded DØ Detector”, *Nucl. Inst. Meth.* A565, 463 (2006).
- [42] P. Azzi *et al.*, “Radiation damage experience at CDF with SVX”, *Nucl. Inst. Meth.* A383, 155 (1998).

- [43] P. F. Derwent, “Radiation monitoring for vertex detectors at the Tevatron”, *Nucl. Instr. Meth.* A447, 110 (2000).
- [44] S.N. Ahmed *et al.*, “DØ SMT Radiation Protection System”, DØ Note 3915 (2001).
- [45] S.N. Ahmed *et al.*, “DØ SMT Radiation Monitoring System”, DØ Note 4022 (2002).
- [46] S. de Jong, “Status of the OPAL microvertex detector and new radiation monitoring and beam dump system”, *Nucl. Instr. Meth.* A418, 22 (1998).
- [47] S. de Jong, C.F. Galea, C.M. Anastasoie, “Radiation dose history in the SMT”, DØ Note 4653 (2004).
- [48] R.E. Kalman, *J. Bas. Eng.* 82D, 35 (1960);
- [49] R.E. Kalman and R.S. Bucy, *J. Bas. Eng.* 83D, 95 (1961).
- [50] P. Billoir and S. Qian (ZEUS exp.), *Nucl. Inst. Meth.* A294, 219 (1990).
- [51] E.J. Wolin and L.L. Ho, *Nucl. Instr. Meth.* A329, 493 (1993).
- [52] H. Greenlee, “The DØ Kalman track fit”, DØ Note 4303 (2003).
- [53] A. Khanov, “HFT: histogramming method for finding tracks. The algorithm description”, DØ Note 3778 (2000).
- [54] P.V.C. Hough, “Machine Analysis of Bubble Chamber Pictures”, Int. Conf. on High Energy Accelerators and Instrumentation, CERN (1959).
- [55] G. Borissov, “Status of DØ track reconstruction”. Talk given at All DØ meeting, 14th February 2003 (2003).
- [56] G. Borissov, “Ordering a chaos or... technical details of AA tracking”. Talk given at All DØ meeting, 28th February 2003 (2003).
- [57] A. Schwartzman and C. Tully, “Primary vertex reconstruction by means of adaptive vertex fitting”, DØ Note 4918 (2005).
- [58] Y. Peters, A. Schwartzman and M. Strauss, “Certification of the adaptive primary vertex in p17”, DØ Note 5192 (2006).
- [59] P. Calfayan *et al.*, “Muon Identification Certification for p17 data”, DØ Note 5157 (2007).

- [60] L. Wang, J. Hays, C. Schwanenberger and J. Mitrevski, “Electron Likelihood efficiency in p17”, DØ Note 5114 (2006).
- [61] G. Blazey *et al.*, “Run II Jet Physics: Proceedings of the Run II QCD and Weak Boson Physics Workshop”, arXiv:hep-ex/0005012v2 (2000).
- [62] U. Bassler and G. Bernardi, “Towards a coherent treatment of calorimetric energies: Missing transverse energy, jets, E.M. objects and the T42 algorithm”, DØ Note 4124 (2003).
- [63] J.-R. Vilmant, U. Bassler, G. Bernardi, S. Trincaz-Duvold, “Technical description of the T42 algorithm on calorimeter objects reconstruction”, DØ Note 4146 (2003).
- [64] DØ JES Group, “Jet Energy Scale Determination at DØ Run II (final p17 version)”, DØ Note 5382 (2007).
- [65] L. Duflot and Melissa Ridel, “The CellNN algorithm: cell level clustering in the DØ calorimeter”, DØ Note 3923 (2001).
- [66] S. Protopopescu and P. Svoisky, “Tau identification with neural networks for p17 data”, DØ Note 5094 (2006).
- [67] C.F. Galea, “Tau Identification at DØ”, Proc. “Physics at LHC 2006, Cracow, Poland”, *Acta Phys. Pol.* B38, 3024 (2007).
- [68] DØ Collaboration (S. Abachi *et al.*), “The DØ Detector”, *Nucl. Inst. Meth.* A338, 185 (1994).
- [69] C.F. Galea, C. Biscarat, J. Stark, S. de Jong, “Tau energy corrections for data and MC in p17”, DØ Note 5533 (2007).
- [70] H.C. Fesefeldt, University of Aachen Technical Report PITHA 85-02 (1985).
- [71] C.F. Galea, S. de Jong, S. Protopopescu, “Tau Energy Correction in Monte Carlo”, DØ Note 5303 (2006).
- [72] C. Biscarat, “Tau-ID in the search for SUSY in the jets+tau+MET signature”. Talk given at the DØ Tau-id meeting from January 31st, 2007 (2007).
- [73] C. Biscarat, S. Protopopescu, “p17 Single tau Monte Carlo sample generation “, DØ Note 4924 (2006).
- [74] C. Zeitnitz, T. A. Gabriel, “The GEANT-CALOR interface and benchmark calculations for ZEUS calorimeters”, *Nucl. Instr. Meth.* A349, 106 (1994).

- [75] J. Temple, R. McCroskey and K. Johns, “Upgrade of Level 1 Muon Trigger Logic for the v13 Trigger List”, DØ Note 4566 (2006).
- [76] A. Maciel, S. Uzunyan, C. Leonidopoulos, J. Kowalkowski, “The L2-Muon Trigger Methods and Algorithms”, DØ Note 4756 (2005).
- [77] T. Sjöstrand *et al.*, Comput. Phys. Commun. **135**, 238 (2001).
- [78] R. Brun and F. Carminati, CERN Program Library Long Writeup W5013, unpublished (1993).
- [79] T. Nunnemann, “NNLO Cross-Sections for Drell-Yan, Z and W Production using Modern Parton Distribution Functions”, DØ Note 4476 (2004).
- [80] B. Tiller, T. Nunnemann, “Measurement of the differential Z^0 -boson production cross-section as a function of transverse momentum”, DØ Note 4660 (2004).
- [81] DØ Collaboration (V.M. Abazov *et al.*), “Measurement of the Shape of the Boson-Transverse Momentum Distribution in $p\bar{p} \rightarrow Z/\gamma^* \rightarrow e^+e^- + X$ Events Produced at $\sqrt{s} = 1.96$ TeV”, *Phys. Rev. Lett.* 100, 102002 (2008).
- [82] M. Shamim, T. Bolton, “Generator Level Reweighting of Z boson p_T ”, DØ Note 5565 (2008).
- [83] H. Schellman, “The longitudinal shape of the luminous region at DØ”, DØ Note 5142 (2006).
- [84] Mike Cook, “WW production cross section measurement and limits on anomalous TGCs”, talk during the plenary session of the DØ Collaboration, February 20th, 2008 (2008).
- [85] B. Martin dit Latour, Y. Arnoud, G. Sajot, E. Shabalina, “Final measurement of the $t\bar{t}$ production cross-section at $\sqrt{s} = 1.96$ TeV in the ee final state using p17 data set”, DØ Note 5579 (2008).
- [86] A. Bellavance *et al.*, “Measurement of $p\bar{p} \rightarrow \mu^+\mu^-$ yield in the Z mass region for DØ Run 2A data”, DØ Note 5269 (2006).
- [87] S.-J. Park, M. Begel, “Efficiency of the Data Quality Calorimeter Flags”, DØ Note 5324 (2007).
- [88] K. Melnikov, F. Petriello, “Electroweak gauge boson production at hadron colliders through $\mathcal{O}(\alpha_s^2)$ ”, *Phys. Rev. D* 74, 114017 (2006).

- [89] C. Anastasiou, L.J. Dixon, K. Melnikov, F. Petriello, “High-precision QCD at hadron colliders: Electroweak gauge boson rapidity distributions at NNLO”, *Phys. Rev. D* **69**, 094008 (2004).
- [90] S. Protopopescu, P. Svoisky, “Systematic uncertainty of τ identification neural network for p17 data”, DØ Note 5408 (2007).
- [91] G. Snow for the Luminosity Working Group, “Adjustments to the Measured Integrated Luminosity for Run IIa”, DØ Note 5139 (2006).
- [92] DØ Collaboration (V.M. Abazov *et al.*), “First measurement of $\sigma(p\bar{p} \rightarrow Z) \times \text{Br}(Z \rightarrow \tau^+\tau^-)$ at $\sqrt{s} = 1.96$ TeV”, *Phys. Rev. D* **71**, 072004 (2005).
- [93] R. Hamberg, W.L. van Neerven and W.B. Kilgore, *Nucl. Phys.* B359, 343 (1991), and its errata in B644, p. 403. Additional description of uncertainties can be found in hep-ph/0308087 (2003).
- [94] A.D. Martin, R.G. Roberts, W.J. Stirling, R.S. Thorne, *Phys. Lett.* B604, 61 (2004).
- [95] J.D. Hobbs, T. Nunnemann and R. Van Kooten on behalf of the Z analysts, “Study of the $p\bar{p} \rightarrow Z/\gamma^* \rightarrow ee$ and $p\bar{p} \rightarrow Z/\gamma^* \rightarrow \mu\mu$ Event Yields as a Luminosity Cross Check”, DØ Note 5268 (2006).
- [96] CDF Collaboration (F. Abe *et al.*), “Measurement of $\sigma\text{B}(W \rightarrow e\nu)$ and $\sigma\text{B}(Z^0 \rightarrow e^+e^-)$ in $p\bar{p}$ Collisions at $\sqrt{s} = 1.8$ TeV”, *Phys. Rev. Lett.* **76**, 3070 (1996).
- [97] CDF Collaboration (F. Abe *et al.*), “Measurement of Z^0 and Drell-Yan Production Cross Section Using Dimuons in $p\bar{p}$ Collisions at $\sqrt{s} = 1.8$ TeV”, *Phys. Rev. D* **59**, 052002 (1999).
- [98] DØ Collaboration (B. Abbott *et al.*), “Measurement of W and Z boson production cross sections (Run Ia)”, *Phys. Rev. D* **60**, 052003 (1999).
- [99] CDF Collaboration (D. Acosta *et al.*), “First Measurements of Inclusive W and Z Cross Sections from Run II of the Fermilab Tevatron Collider”, *Phys. Rev. Lett.* **94**, 091803 (2005).
- [100] CDF Collaboration (A. Abulencia *et al.*), “Measurement of $\sigma(p\bar{p} \rightarrow Z) \cdot \text{B}(Z \rightarrow \tau\tau)$ in $p\bar{p}$ Collisions at $\sqrt{s} = 1.96$ TeV”, *Phys. Rev. D* **75**, 092004 (2007).
- [101] A. Read, “Presentation of search results: the CL(s) technique”, *J. Phys.* G28, 2693 (2002).
- [102] T. Junk, “Confidence level computation for combining searches with small statistics” (1999).

- [103] W. Fisher, “Calculating limits for combined analyses”, DØ Note 5309 (2006).
- [104] T. Junk, *Nucl. Instr. Meth.* A434, 435 (1999);
- [105] A. Read, *Journ. of Phys.* G28: *Nucl. Part. Phys.*, 2693 (2002).
- [106] R. Brun, F. Rademakers, P. Canal, I. Antcheva and D. Buskulic, ROOT User’s Guide, July 2007, <http://root.cern.ch> (2007).
- [107] T. Junk, “Sensitivity, Exclusion and Discovery with Small Signals, Large Backgrounds and Large Systematic Uncertainties”, CDF Note 8128 (2007).
- [108] W. Fisher, “Systematics and Limit Calculations”, DØ Note 5309 (2006).
- [109] S. Catani, D. de Florian, M. Grazzini, P. Nason, ”Soft-gluon resummation for Higgs boson production at hadron colliders”, arXiv:hep-ph/0306211v1 (2003).
- [110] S. Heinemeyer, W. Hollik, G. Weiglein, *Comput. Phys. Commun* 135, 238 (2001).
- [111] The Tevatron Electroweak Working Group for the CDF and DØ Collaborations, “Combination of CDF and DØ Results on the Mass of the Top Quark”, FERMILAB-TM-2403-E (2008).
- [112] C.F. Galea, S. de Jong, “Measurement of $\sigma(p\bar{p} \rightarrow Z) \cdot \text{Br}(Z \rightarrow \tau^+\tau^-)$ with 1 fb^{-1} at $\sqrt{s} = 1.96 \text{ TeV}$ “, DØ Note 5484 (2007).
- [113] DØ Collaboration (V. Abazov *et al.*), “Search for Neutral Higgs Bosons Decaying to Tau Pairs in $p\bar{p}$ Collisions at $\sqrt{s}=1.96 \text{ TeV}$ “, *Phys. Rev. Lett.* 97, 121802 (2006).

Summary

The resonant production of tau-lepton pairs is as interesting for the study of Standard Model (SM) physics as the production of lighter leptons pairs. For new phenomena, such as Higgs boson production or in case new particles beyond the SM would arise, the detection of (resonant) pairs of tau leptons becomes much more interesting. This is due to the fact that tau leptons are much heavier than the other leptons, which increases the chance that these new phenomena would be observed first in this channel. Unfortunately their clean detection is far more difficult than that of muons or electrons.

The cross section times branching ratio $\sigma \cdot \text{Br}$ for the process $p\bar{p} \rightarrow Z \rightarrow \tau^+\tau^-$ was measured at $\sqrt{s} = 1.96$ GeV using 1.0 fb^{-1} of data collected by the DØ experiment. This measurement was performed in the channel in which one of the tau leptons decays to a muon and neutrinos, while the other decays either hadronically or to an electron and neutrinos. A set of 1511 events, of which about 20 % estimated background, passed all selection criteria. The trigger and muon reconstruction efficiencies, as well as the efficiency for track reconstruction were obtained from data using the “tag and probe” method on $Z \rightarrow \mu^+\mu^-$ events. The multijet background was estimated from the sample of events which passed all selection criteria but in which the muon and the tau candidate had the same charge. The $W \rightarrow \mu\nu + \text{jets}$ background was modeled by Monte Carlo simulations, but normalized to data. All the other backgrounds, as well as the efficiency for $Z \rightarrow \tau^+\tau^-$ events were estimated using simulated events normalized to the theoretical calculations of cross sections at next-to-leading order or next-to-next-to-leading order. The energy of the tau candidates was corrected for the estimated response of the charged pions in the calorimeter, which is of the order 50 – 80 %. Since the charged pion response in data was not well reproduced by the default simulation of hadronic interactions (Geisha), a different simulation (gCALOR) was used to obtain an estimated charged pion response consistent with the one measured in data. This tau energy correction method makes use of the superior resolution of the track momentum measurement compared to the resolution of the tau candidate energy as measured by the calorimeter, which leads to a better data - simulation agreement and a decrease of 10 % in the resolution of the visible mass peak.

The result of this measurement is $\sigma(p\bar{p} \rightarrow Z) \cdot \text{Br}(Z \rightarrow \tau^+\tau^-) = 240 \pm 8 \text{ (stat)} \pm 12 \text{ (syst)} \pm 15 \text{ (lumi) pb}$, in good agreement with the theoretical predictions of $241.6^{+3.6}_{-3.2} \text{ pb}$ [79] or $251.9^{+5.1}_{-12} \text{ pb}$ [93–95], as well as with other measurements performed by the DØ and CDF experiments in all channels in which the Z boson decays leptonically [96–100]. This is the most precise Z boson cross section measurement to date performed in the tau lepton channel at hadron colliders. The analysis demonstrates the ability of the DØ experiment to identify tau leptons decaying hadronically with good efficiency and high purity, a challenging task in $p\bar{p}$ collisions where the number of jets resembling tau leptons is very high. This achievement forms a solid basis for other analyses using hadronic tau lepton decays, such as the search for the Higgs boson decaying into tau-lepton pairs, which was performed for the last part of this thesis.

The Higgs mechanism to break electroweak symmetry is an essential ingredient of the SM. The mechanism predicts the existence of a Higgs boson, that so far has not been directly observed experimentally. As no evidence for sources of resonant $\tau^+\tau^-$ events was found in addition to the known SM processes, limits on the production of a neutral Higgs boson were set at 95 % confidence level (CL) using the semi-frequentist CL_s method. A variable which has a good separation between a potential Higgs boson signal and the SM backgrounds, called visible mass and representing a partially reconstructed mass from the energy of the tau candidate, the momentum of the muon and the missing transverse energy, was used for the limit setting procedure. Since the classical treatment of the systematic uncertainties smears the signal-plus-background and background-only probability density functions, making their separation less visible, an alternative approach was also used. In this new method, called profiling, the systematic uncertainties were varied within their constraints for each pseudo-experiment such that the best fit to the pseudo-experiment “data” is found, in both the signal-plus-background and background-only hypotheses.

The results obtained in this thesis set the tightest limits to date on the cross section times branching ratio $\sigma \cdot \text{Br}$ for the process $p\bar{p} \rightarrow H \rightarrow \tau^+\tau^-$ for a Higgs boson with a mass below 130 GeV, and comparable for the rest of the studied mass interval with the results obtained by the CDF experiment [40] using an analysis based on 1.8 fb^{-1} . However, this analysis is still far from probing the existence of a SM Higgs boson. The upper limits set here are higher than the theoretical SM Higgs boson cross section by factors of 80 – 160 for the relevant Higgs boson mass interval.

A search for a Higgs boson decaying to tau leptons is of particular interest in models with more than one Higgs doublet, where production rates for $p\bar{p} \rightarrow H \rightarrow \tau^+\tau^-$ can potentially be large enough for an observation at the Tevatron. Within the Minimal Supersymmetric Standard Model (MSSM), if the mass of the CP-odd neutral scalar Higgs boson m_A is low and the ratio of the vacuum expectation values of the two supersymmetric Higgs doublets, $\tan\beta$, is large, the Higgs boson production via b quarks can be greatly enhanced, by a factor of $\tan^2\beta$. Besides, one of the CP-even neutral Higgs bosons is degenerate with A, which effectively doubles the cross section.

Upper limits on $\tan\beta$ of the order 40 – 60 for the Higgs boson mass interval 90 – 170 GeV were set for certain MSSM benchmark scenarios [33,34] using the cross section limits on the $p\bar{p} \rightarrow H \rightarrow \tau^+\tau^-$ process obtained with the profiling method. These are comparable with the limits set by the CDF experiment [40] for the entire Higgs boson mass range studied in this thesis. Lower limits of typically 4 – 20 were set on $\tan\beta$ at LEP [35]. For a certain scenario within the MSSM (no-mixing, $\mu < 0$), the mass region 112 – 120 GeV is already excluded for the lightest neutral Higgs boson [113].

The data set collected by the DØ experiment at the time this analysis was completed had already reached 3.4 fb^{-1} and the Tevatron is expected to deliver 8 fb^{-1} by 2010. Higher luminosity, the inclusion of the decay mode $H \rightarrow \tau(\rightarrow e\nu_\tau\nu_e)\tau(\rightarrow \text{hadrons})$, allowing more trigger channels and the combination of the results from the two $p\bar{p}$ collision experiments at Fermilab, DØ and CDF, will lead to a significant increase in sensitivity for this search. If supersymmetry exists, the process $p\bar{p} \rightarrow H \rightarrow \tau^+\tau^-$ is one of the golden channels for a discovery at the Tevatron.

Samenvatting

De resonante productie van tau-lepton paren is net zo interessant voor de studie van Standaard Model (SM) fysica als de productie van lichtere lepton paren, electronen en muonen. Voor nieuwe verschijnselen, zoals Higgs boson productie of in het geval nieuwe deeltjes voorbij het Standaard Model zullen verschijnen, wordt de detectie van (resonante) paren van tau leptonen veel interessanter. Dit is een gevolg van het feit dat tau leptonen veel meer massa hebben dan de andere leptonen, hetgeen de kans vergroot dat deze nieuwe verschijnselen het eerst geobserveerd zullen worden in dit kanaal. Helaas is hun detectie veel moeilijker dan muonen of electronen.

De werkzame doorsnede vermenigvuldigd met de vertakkingsverhouding $\sigma \cdot \text{Br}$ voor het proces $p\bar{p} \rightarrow Z \rightarrow \tau^+\tau^-$ werd gemeten bij $\sqrt{s} = 1.96$ GeV, gebruik makend van 1.0 fb^{-1} data, verzameld met de DØ detector. Deze meting werd verricht in het kanaal waarin een van de tau leptonen vervalst naar een muon en neutrino's, terwijl het andere vervalst ofwel hadronisch ofwel naar een electron en neutrino's. Een verzameling van 1511 gebeurtenissen, waarvan ongeveer 20 % geschatte achtergrond, vervulde alle selectie criteria. De efficiëntie van de trigger en muon reconstructie, alsmede de efficiëntie van de spoor reconstructie werden vanuit de data verkregen, met gebruik van een methode waarin één muon van $Z \rightarrow \mu^+\mu^-$ gebeurtenissen wordt waargenomen en dan gekeken wordt of het andere muon waarneembaar is. De multi-jet achtergrond van de sterke interactie werd geschat vanuit de verzameling gebeurtenissen die aan alle selectie criteria voldeden, maar waarin het muon en de tau kandidaat dezelfde lading hadden. De $W \rightarrow \mu\nu + \text{jets}$ achtergrond werd gemodelleerd met Monte Carlo simulaties, maar genormeerd op het aantal in de data. Alle andere achtergronden, alsmede de efficiëntie voor $Z \rightarrow \tau^+\tau^-$ gebeurtenissen werden geschat met behulp van gesimuleerde gebeurtenissen, genormeerd naar de theoretische hogere orde berekeningen van werkzame doorsnedes. De energie van de tau kandidaten werd verbeterd voor de geschatte respons van geladen pionen in de calorimeter, die circa 50 – 80 % is. Aangezien de geladen pion respons in de data niet goed werd gereproduceerd door de standaard simulatie van hadronische interacties (Geisha), werd een andere simulatie (gCALOR) gebruikt om een geschatte geladen pion respons, consistent met die gemeten in data, te verkrijgen. De tau energie correctie methode maakt gebruik van de superieure resolutie van de impulsmeting van het geladen spoor, in vergelijking met de resolutie van de calorimeter voor tau kandidaat energie. Dit leidt tot een betere data - simulatie overeenkomst en een verbetering van 10 % in de resolutie van de zichtbare massa piek.

Het resultaat van deze meting is $\sigma(p\bar{p} \rightarrow Z) \cdot \text{Br}(Z \rightarrow \tau^+\tau^-) = 240 \pm 8 \text{ (stat)} \pm 12 \text{ (syst)} \pm 15 \text{ (lumi) pb}$, in goede overeenstemming met de theoretische voorspelling van $241.6^{+3.6}_{-3.2} \text{ pb}$ [79] of $251.9^{+5.1}_{-12} \text{ pb}$ [93–95], alsmede met andere metingen gedaan door de DØ en CDF experimenten in kanalen waarin het Z boson leptonisch vervalst [96–100]. Dit is tot op heden de meest precieze Z boson werkzame doorsnede meting, gedaan in het tau lepton kanaal bij hadronische botsers. De analyse toont het vermogen van

het DØ experiment aan om hadronisch vervallende tau leptonen te identificeren met goede efficiëntie en zuiverheid, een uitdagende taak in $p\bar{p}$ botsingen, waar het aantal jets dat op tau leptonen lijkt erg groot is. Deze prestatie vormt een solide grondslag voor andere analyses die hadronische tau lepton vervallen gebruiken, zoals de zoektocht naar het Higgs boson vervallend naar tau lepton paren, hetgeen werd gedaan voor het laatste deel van dit proefschrift.

Het Higgs mechanisme voor electrozwakke symmetriebreking is een essentieel onderdeel van het Standaard Model. Het Higgs boson wordt door dit mechanisme voorspeld, maar is tot nu toe experimenteel niet direct waargenomen. Aangezien er geen bewijs voor extra resonante $\tau^+\tau^-$ gebeurtenissen werd gevonden, werden bovenlimieten met een 95 % betrouwbaarheidsniveau gezet op neutrale Higgs boson productie, gebruik makend van de semi-frequentistische CL_s methode. Een variabele die een goed onderscheid van een mogelijk Higgs boson signaal en SM achtergronden geeft is de zichtbare massa. De zichtbare massa is een gedeeltelijk gereconstrueerde massa door gebruik te maken van de energie van de tau kandidaat, de impuls van het muon en de ontbrekende transversale energie (die door de niet waargenomen neutrino's wordt veroorzaakt). Aangezien de klassieke behandeling van systematische onzekerheden de signaal-plus-achtergrond en achtergrond waarschijnlijkheidsverdelingen vager maakt, werd ook een alternatieve aanpak gebruikt. In deze nieuw methode, "profiling" genoemd, worden de systematische onzekerheden voor elk pseudo-experiment zodanig gevarieerd binnen de grenzen van die onzekerheid dat de beste passing wordt gevonden aan de pseudo-experiment "data", voor zowel de signaal-plus-achtergrond als achtergrond hypotheses.

Het resultaat verkregen met de "profiling" methode zet de tot op heden scherpste bovenlimieten op de werkzame doorsnede vermenigvuldigd met de vertakkingsverhouding voor het proces $p\bar{p} \rightarrow H \rightarrow \tau^+\tau^-$, voor een Higgs boson massa van minder dan 130 GeV, en bovenlimieten voor de rest van het bestudeerde massa interval vergelijkbaar met de resultaten verkregen door het CDF experiment [40] gebaseerd op 1.8 fb^{-1} data. Echter, voor een Higgs boson massa van 100 – 150 GeV is deze analyse ver verwijderd van het onderzoeken van de aanwezigheid van een SM Higgs boson. De bovenlimieten die hier gezet worden zijn een factor 80 – 160 groter dan de SM Higgs boson werkzame doorsnede voor het relevante Higgs boson massa interval.

Eindtoestanden die tot tau lepton paren met een grote massa leiden, kunnen ook voortkomen uit fysische processen voorbij het SM, inclusief de productie van neutrale Higgs bosonen in het Minimale Supersymmetrische Standaard Model (MSSM). Een zoektocht naar een Higgs boson vervallend naar tau leptonen is bijzonder interessant in modellen met meer dan één Higgs doublet veld, waarin de productie voor $p\bar{p} \rightarrow H \rightarrow \tau^+\tau^-$ mogelijk groot genoeg is voor een waarneming bij het Tevatron. Als in het MSSM de massa van het CP-oneven neutrale scalaire Higgs boson m_A laag is en de verhouding van de vacuümverwachtingswaarden van de twee supersymmetrische Higgs paren, $\tan\beta$, groot is, dan kan de Higgs boson productie met een verval in b quarks en τ leptonen aanzienlijk vergroot zijn, met een factor $\tan^2\beta$. Bovendien is dan het CP-even neutrale Higgs boson gedegenerereerd met A hetgeen de werkzame doorsnede effectief verdubbelt.

Bovenlimieten op $\tan\beta$ van typisch $40 - 60$ voor het Higgs boson massa interval $90 - 170$ GeV werden gezet voor bepaalde MSSM scenario's [33,34], gebruik makend van de limieten op de werkzame doorsnede van het proces $p\bar{p} \rightarrow H \rightarrow \tau^+\tau^-$, verkregen met de “profiling” methode. Deze bovengrenzen op $\tan\beta$ zijn op dit moment het meest stringent. Ondergrenzen op $\tan\beta$ van typisch $4 - 20$ werden gezet door de LEP experimenten [35]. Voor het MSSM scenario zonder menging in de Higgs sector en met $\mu < 0$ wordt het massa domein $112 - 120$ GeV al uitgesloten voor het lichtste neutrale Higgs boson [113].

De hoeveelheid data verzameld door het DØ experiment op het moment dat deze analyse voltooid werd, heeft 3.4 fb^{-1} al bereikt, en de verwachting is dat het Tevatron tegen 2010 8 fb^{-1} levert. Een hogere luminositeit, het toevoegen van de analyse van het kanaal $p\bar{p} \rightarrow H \rightarrow \tau(\rightarrow e\nu_\tau\nu_e)\tau(\rightarrow \text{hadrons})$, het gebruiken van meer trigger mogelijkheden en de combinatie van de resultaten van de twee experimenten bij het Tevatron, DØ en CDF, zullen leiden tot een significante toename van de gevoeligheid voor deze zoektocht. Als supersymmetrie bestaat, dan is het proces $p\bar{p} \rightarrow H \rightarrow \tau^+\tau^-$ een van de gouden kanalen voor de ontdekking daarvan bij het Tevatron.

About the author

Cristina Florina Galea was born on March 26th, 1975 in Bucharest, Romania. She obtained a BSc. degree in Mathematics and Computer Science in 1998 and a BSc. in Physics in 2000, both from the University of Bucharest. After graduating, she spent a year at the Max Planck Institut für Radioastronomie in Bonn, where she studied the origin of the cosmic magnetic fields with Prof. Peter Biermann. She earned her MSc. degree in Physics from the University of Bucharest in 2002.

After her masters degree she started a PhD. in particle physics at the University of Nijmegen, participating in the DØ experiment under the supervision of Prof. Sijbrand de Jong. She spent a total of one and a half years in Nijmegen and almost 4 years at Fermilab, where she worked on radiation monitoring, data acquisition, tau triggers, the measurement of the Z boson cross section and a search for the Higgs boson in the tau lepton channel.

During her studies she went to several summer schools, four of them on astrophysics topics and four on particle physics topics. As customary, she presented her work and the work of her colleagues from the DØ and CDF experiments at several conferences and workshops, such as the Deep Inelastic Scattering (DIS 2008) Conference in London, England, the Physics at LHC 2006 Conference in Cracow, Poland or the Annual DØ Workshops in Fresno, California (2004) and Manchester, England (2006). She participated as scientific secretary in the XXXI International Conference on High Energy Physics (ICHEP 2002) in Amsterdam, the Netherlands, and the XXI International Symposium on Lepton and Photon Interactions (Lepton Photon 2003) in Batavia, IL, USA.

She is married to a fellow physicist from the DØ experiment, Michiel Sanders, and they have a three year old son, Pieter. When not doing physics, the author enjoys meeting with friends and family members, climbing mountains, reading, photography and playing with her son.

Acknowledgements

Writing a thesis in particle physics feels often like climbing the Everest. First of all, you can not do it alone. It takes the work of many hundreds of people for many years to build and run an accelerator like the Tevatron and an experiment like DØ, so many thanks go to all of them first.

Then, you need a good sherpa. I would like to thank my advisor, Sijbrand de Jong, for giving me the opportunity to work with him in what turned out to be a great challenge. He knew when to leave me alone to wander on my own for weeks (months?), and when to answer twenty e-mails per day if things got heated, often at odd hours of the night. Working with him was always easy and fun, so I feel very fortunate. He also pulled me out of several crevasses over the years, for which I am most grateful. Overall, I profited a lot from his insight in matters of physics and other related or unrelated issues. His patience and help through the many hundreds of versions of this thesis were also much appreciated.

Once in Nijmegen, Marjo, Hanneke, Annelies and Gemma were always very helpful with all the bureaucratic matters. Dank u wel! The company of Charles, Frank, Silke, Axel, Bram and occasionally Sijbrand or Nicolo made lunches much more entertaining. Peter, Yuan, Miran, Qin and Tamas were always nice to talk to as well.

The real climb began when I moved to Fermilab, five months after I started my PhD. Working in the Tau ID group was a good way to plunge into the DØ world. I learned a lot of physics over the years from Șerban Protopopescu, with whom it was always great to work on tau related issues. I would like to thank him also for reading my thesis and commenting on it. But in fact I've learned something from each member of the group, so I would like to thank them all. Same goes for the L3 and EW groups.

Ron Lipton was always helpful with the radiation monitor electronics, during the time when we were trying to calibrate the diodes. And Alan Stone might have saved me from getting an ulcer on that fifth night in a row of DAQ shifts, when he brought us shifters a nice turkey, just because it was Thanksgiving. For that, and for his call at 3 AM in the morning to remind me to put crate 10 in the physics run that we had started minutes earlier, I will always have a soft spot for him. From all the people roaming in the control room during those days, I distinctly remember the calm of Dmitri Denisov, who must be one of the most patient and positive persons I ever met.

Lukas introduced me to the ritual of having lunch with “the Dutch”, which at the time included Michiel, Martijn and himself. The ritual was very pleasant and survived long after he left. In fact, now that we are married, I still have lunch with Michiel occasionally. Life at Fermilab would have not been the same without all the after hours activities: the “movie & billiard” nights that Daniela and I were throwing for “the Germans” in Aurora, the salsa classes with Martijn, Janis and whoever else wanted to come along, the “girl movie” nights with Tulika, Emily, Meta and Amber. The parties with “the Brits” in the Chicago’s “corn cubs” at Tamsin’s and Emily’s place were a lot of fun, and the same goes for the ones hosted by Tim and Silke, Jon and Daniela, Martijn and Janis, Arnaud or Kyle.

Pieter, Miruna, the other Pieter, Jeroen and Bob were excellent company for the renewed “Dutch” lunches. Later they left, but Lucian and Mike took their place. Even though by then I had had it with the food at the High Rise, the bagel place and East China Inn, preferring to eat lunch in front of the computer, the conversations with them kept our cubicle a very lively place.

When I moved back to the Netherlands after two years at Fermilab, the climb started to get harder and harder. And then all of the sudden it got lighter again, by about 4.2 kg, and Pieter was here to fill our lives with smiles and sleepless nights. Thanks to Sijbrand, I didn’t have to choose between my thesis and my family, being allowed to move back to Fermilab. Many thanks go to the people at the Fermilab’s Daycare Center, who took care of Pieter when I went back to work after four months at home with him. While our party life was clearly over, we noticed that hanging out with the adults (and their kids) can be just as nice. Many thanks to Terry and Anne, who invited us often to their house full of toys, where Pieter always had a blast playing with Jem and later with Laurie. Same goes for Adam and Caryn, with whom we had a lot of fun watching Pauline and Pieter grow up together over the last three years.

Moving to Paris a year ago had both advantages and disadvantages. The food got a whole lot better, but there was no daycare option, which is not exactly ideal when one tries to write a thesis. Many thanks go to Paul, Liesbeth, Yolande, Jan Willem and Sophie for taking care of us in our visits to Loenen and for coming to look after Pieter when I had to go to a conference in London. Meeting with Mona, Alex and Sonia, Gențiana, Jose and their three girls, Viorica, Christophe and Gregoire, Mădălina and her family, Elena, Doru and Ioana made me feel very much at home here. To all my Base Camp friends, but in particular to Becca, Dee, Carly, Heather, Tori, Eve, Mel, Jen, Gretchen, Sue, Becky and Melissa - many thanks for just being there, and for all the laughs until we cried. Same goes for all my friends from Mathematics: Miki, Domnica, Bogdan, Ruxi, John, Danuț and Ionuț, as well as Adriana, Roxana and Florin.

The final bit is always the hardest: the air is thin and you are so tired that you can barely put a foot in front of the other. But the view is great and you can finally see the peak. My analysis profited a lot at this final stage from the careful review of the Editorial Boards 31 and 14, so many thanks go to Yann Coadou, Marie-Claude Cousinou, Peter Mättig, Marek Zielinski, Barbro Åsman, Marc Besançon, Leo Bellantoni, Fabrice Couderc, Slava Sharyy and Boris Tuchming for their helpful suggestions. The same goes for all the members of my thesis committee, in particular Marcel Demarteau. A big thank you to Peter Svoisky for his help with implementing the weights in my analysis and with the FeynHiggs plots, not to mention all the tea and Russian cookies.

Finally, I must thank my father for always supporting me in what I wanted to do and for buying me a book with all the mathematics formulas that I ever needed when I was 10. My mother never got to see me graduating from Physics, but I would like to thank her as well, for everything. I could always count on Ioana’s hospitality when we went to Romania and on Dana’s love and the support, as well as those of my entire family, which is too large to mention everyone here by name.

There is no proper way to thank Michiel and Pieter in a few lines for their love and all the ways they touched my life in the last years, so I’m not even going to try. Instead, I will just love them back and they will know that I am grateful.